Copyright
by
Nicholas Deak
2023

The Dissertation Committee for Nicholas Deak certifies that this is the approved version of the following dissertation:

Development and application of a high-performance framework for high-fidelity simulations of plasma-assisted ignition of hydrocarbon fuels using nanosecond pulsed discharges

Committee:
Fabrizio Bisetti, Supervisor
Laxminarayan Raja
Philip Varghese
Marcus Day

Development and application of a high-performance framework for high-fidelity simulations of plasma-assisted ignition of hydrocarbon fuels using nanosecond pulsed discharges

 $\mathbf{b}\mathbf{y}$

Nicholas Deak

DISSERTATION

Presented to the Faculty of the Graduate School of
The University of Texas at Austin
in Partial Fulfillment
of the Requirements
for the Degree of

DOCTOR OF PHILOSOPHY

THE UNIVERSITY OF TEXAS AT AUSTIN ${\rm August~2023}$

Dedicated to my grandmother, whose deep curiosity and love of learning inspired me to find my current path.
me to mid my current patii.
4

Acknowledgments

This dissertation would not have been possible without the support of several people who I wish to thank.

Firstly, I would like to thank my advisor Dr. Fabrizio Bisetti for the guidance he has provided over the past several years. His approach towards research, which combines an admirable scientific passion along with considerable academic rigor and great attention to detail, has been incredibly formative, and are qualities I aspire to carry with me throughout future projects. I also wish to thank my dissertation committee members, Prof. Laxminarayan Raja, Prof. Philip Varghese, and Dr. Marc Day for their valuable feedback, which helped me to improve my dissertation.

I had the opportunity to work with a number of exceptionally talented peers during my graduate studies. Prof. Aurélie Bellemans provided guidance and mentorship during her time as a post-doc in our research group. I also want to thank my fellow graduate students, including Dr. Tejas Kulkarni, Dr. Evrim Solmaz, Alfredo Duarte, Mitch Hollander, and Aditya Vinod, for their help and support throughout my studies. The considerable computational expertise provided by Dr. Marc Day and Dr. Lucas Esclapez, and their continued support throughout my research was an invaluable asset. I also wish to thank the ASE staff for their support during my graduate studies.

This research I conducted throughout my studies was supported by NSF grant

#1903775 and DOE contract DE-EE0008874. The simulations I conducted through the course of my program relied on computational resources generously provided by the Texas Advanced Computing Center (TACC), as well as the National Renewable Energy Laboratory (NREL). I am grateful to all of these institutions for the funding and computational resources that made my research possible.

I also want to thank my friends in Austin, including Dr. Suda Bharadwaj, Dr. Steve Carr, Mustafa Karabag, Yusuf Yagiz Savas, Maansi Desai, and many others. The time we spent together at Barbarella, Sida Bar, Violet Crown, and elsewhere made my time in Austin an amazing and unique experience.

Finally, I want to express my sincere gratitude for the love and support of my family, who provided encouragement and guidance through both easy and challenging times during my studies. Development and application of a high-performance framework for high-fidelity simulations of plasma-assisted ignition of hydrocarbon fuels using nanosecond pulsed discharges

Publication No.

Nicholas Deak, Ph.D. The University of Texas at Austin, 2023

Supervisor: Fabrizio Bisetti

The application of non-equilibrium plasma (NEP) pulses to ignite hydrocarbon/air mixtures has emerged as a promising technology for ensuring reliable ignition and combustion stability in difficult regimes. Despite its promise, major challenges and limitations still remain, particularly in the realm of conducting high-fidelity multidimensional numerical studies. The aim of this thesis is to develop, implement, and apply a robust and efficient computational framework that addresses some of these shortcomings.

As a preliminary step, the ignition of hydrocarbon/air mixtures by nanosecond pulsed discharges (NSPD) is investigated using a zero dimensional isochoric adiabatic reactor. A state-of-the-art two-temperature kinetics model, comprised of an experimentally-verified NEP plasma mechanism coupled with a hydrocarbon/air

7

oxidation mechanism, is used. Simulations are performed to assess the impact of changing initial pressure (which varies from 1 to 30 atm) and fuel type (methane and ethylene). It is found that at lower pressures, plasma-assisted ignition (PAI) imparts a benefit over thermal ignition for both fuel types, through the creation of combustion radicals O, H, and OH. At higher pressures, PAI of methane loses efficiency compared to ethylene, due to a lack of available H radicals (which are swept up by O_2), which limits the conversion of formaldehyde to formyl.

Next, a robust and efficient framework for simulating NSPD in multiple dimensions is developed. The reactive Navier-Stokes equations are extended to include a drift-diffusion plasma-fluid model with a local field approximation (LFA) in a finite-volume solver, which uses an adaptive mesh refinement (AMR) strategy to address the wide separation of length scales in the problem. A two-way coupling strategy is used whereby the plasma-fluid model and reactive Navier-Stokes equations are integrated simultaneously. An effective grid refinement approach is developed in order to ensure that the physical structures that arise during and after the NSD (including the propagating streamer heads, electrode sheaths, and expansion wave during the interpulse period) are resolved efficiently. Severe time step size restrictions that arise from the explicit temporal integration of the transport terms are mitigated through use of a semi-implicit approach for solving Poisson's equation for the electric potential, and an implicit strategy for evaluating electron diffusion terms.

A series of numerical studies are then conducted to investigate the ignition and propagation phases of atmospheric air streamers in axisymmetric discharge configurations. A range of conditions and configurations are explored to characterize the streamer, with an emphasis on the cathode sheath region, which supports steep gradients in charged species number densities as well as strong electric fields. The formation of the cathode sheath is shown to be a consequence of processes at the cathode surface, driven by electron losses at the boundary, and a strong dependence on the emission of secondary electrons.

Finally, the oxidation of ethylene/air mixtures mediated by NSPD is simulated in a pin-to-pin configuration. All phases of the plasma discharge are simulated explicitly (including streamer ignition, propagation, and connection, as well as the subsequent spark phase), along with the evolution of the plasma during the interpulse period. Temporally and spatially-resolved results are presented, with an emphasis on the analysis of heating and energy deposition, as well as of the evolution of the concentration of active particles generated during the NSPD and their influence on ignition. The impact of pin thickness is discussed, and it is shown that the use of thin pins limits the regions of energy deposition and temperature increase near the pin tips, hindering ignition. The application of multiple pulses is explored and it is shown that multiple voltage pulses of the same strength leads to substantial energy deposition and temperature increases $\mathcal{O}(1,000-10,000~\mathrm{K})$ near the pin tips. Discussion is rounded out by addressing how pulse frequency and initial mixture control the generation of active particles and combustion products. Finally, recommendations for future work are provided.

Table of Contents

Ackno	wledg	ments	5
Abstra	act		7
List of	Table	es	13
List of	Figui	res	14
Chapt	er 1.	Introduction	20
1.1	Litera	ature review	21
	1.1.1	Discharge regimes	21
	1.1.2	Simulations of discharges in air	22
	1.1.3	Electrode sheaths	23
	1.1.4	Plasma-assisted ignition	25
		1.1.4.1 Chemical and plasma kinetics and energy deposition .	25
		1.1.4.2 Development of kinetics mechanisms	26
		1.1.4.3 Numerical investigations	29
Chapter 2.		Impact of fuel type and pressure on plasma-assisted ignition	- 33
2.1	Two-1	temperature reactor governing equations	34
2.2	Kinet	ic mechanism	35
	2.2.1	Assumptions and limitations of the two-term approximation for the electron distribution function	37
2.3	Resul	ts	42
	2.3.1	Preliminaries and overview	42
	2.3.2	Pressure effects on τ	44
	2.3.3	Pressure effects on plasma and combustion kinetics	46
	2.3.4	Stoichiometry effects on ignition efficiency	49

	2.3.5	Impact of pulse frequency and duration on ignition
	2.3.6	Radical production
	2.3.7	Fuel effects
$\mathbf{Chapt}_{\mathbf{c}}$	er 3.	Ignition and propagation of streamers in air, and formation of the cathode sheath 62
3.1	Mode	ls and Methods
	3.1.1	Governing equations and computational domain 63
	3.1.2	Validity of the plasma fluid model 67
	3.1.3	Photoionization
	3.1.4	Initial and boundary conditions
	3.1.5	Kinetics
	3.1.6	Advancement Algorithm
	3.1.7	Numerical methods
3.2	Simul	ation results
	3.2.1	Simulation overview
		3.2.1.1 Streamer ignition and propagation 81
		3.2.1.2 Sheath formation
	3.2.2	Impact of electron emissions on formation of the cathode sheath 92
	3.2.3	Impact of initial conditions, photoionization, and problem geometry
Chapt	er 4.	Simulations of the plasma-assisted oxidation of ethylene/air mixtures 104
4.1	Mode	l and numerical methods
	4.1.1	Governing equations
	4.1.2	Reduced ethylene/air kinetics mechanism 109
	4.1.3	Numerical methods
		4.1.3.1 Plasma fluid model
		4.1.3.2 Grid resolution and time step size
4.2	Ethyl	ene/air results
	4.2.1	Voltage sensitivity
	4.2.2	Single pulse solution
		4.2.2.1 Solution overview

		4.2.2.2 Generation and consumption of combustion radicals	131
		4.2.2.3 Barriers to successful ignition	138
	4.2.3	Multiple pulse dynamics	140
	4.2.4	Streamers at elevated temperatures and pressures	145
\mathbf{Chapte}	er 5.	Summary and conclusions	151
5.1	Kineti	ic enhancement of plasma-assisted ignition	152
5.2	Imple	ementation of a multidimensional NSD solver	154
5.3	Stream	mers in air and the cathode sheath	154
5.4	Ignitio	on of ethylene/air mixtures using nanosecond pulsed discharges .	156
5.5	Recon	mmendations for future work	159
Appen	dices		161
Appen	dix A	. Rate coefficient fitting for electron reactions	162
Appen	dix B	. Detailed PAC mechanism	163
Appen	dix C	. Reduced ethylene/air mechanism	164
Bibliog	raphy	V	165

List of Tables

3.1	Summary of reactions and rates used in this study. Rate coefficients that depend on E/N and T_e use units of Td and K. The parameters for the ionization rate coefficients are modified from [118, 70] in order to provide a more accurate fit over a wider range of reduced electric field strengths	74
3.2	Parameters for pin-to-pin discharge simulations conducted in atmospheric quiescent air. Case R is the reference simulation. Problem sizes correspond to the maximum number of control volumes observed during each simulation, summed across all AMR levels	80
4.1	Plasma species included in the kinetics mechanism	109
4.2	Summary of reactions involving electrons and ions	110
4.3	Initial conditions used for increasing temperature and pressure PAC streamer cases assuming isentropic compression and stoichiometric ethylene/air	118

List of Figures

1.1	NSD in the corona, glow, and spark regimes in atmospheric air at $T_0 = 1000$ K. Adapted from [111]	21
1.2	Streamer in atmospheric air at $T_0 = 300 \text{ K}$ with stochastic photoionization. Adapted from [95]	24
1.3	Schlieren images following a NSD in atmospheric air at $T_0 = 1000 \text{ K}$ in a pin-to-pin configuration. Adapted from [177]	27
1.4	Contour surfaces for the electron number density, energy density, and power density deposition for streamers in a stoichiometric methane/air mixture at atmospheric conditions and $T_0 = 300$ K. Streamers are generated in a pin-to-plane configuration using different pulse voltage strengths. Adapted from [23]	30
1.5	Temperature field at different instants in time for different energy deposition strategies, including direct energy deposition, application of a single NSD, and application of multiple NSD. Adapted from [14]	31
2.1	Rate coefficients for elastic collisions between electrons and N_2 (E + $N_2 \rightarrow E + N_2$), inelastic collisions resulting in vibrational excitation of N_2 (E + $N_2 \rightarrow E + N_2(v3)$), and inelastic collisions resulting in dissociation of N_2 (E + $N_2 \rightarrow E + 2N$). Results are shown for atmospheric air at 300 K (solid lines), atmospheric air at 1000 K (dashed lines), and stoichiometric ethylene/air at atmospheric conditions and 300 K (dotted lines)	40
2.2	Electron collision rates as a function of the reduced electric field strength for the same mixtures at atmospheric pressure as in Fig. 2.1	41
2.3	Time evolution of the mean electron energy ε , number density of select species and gas temperature during ignition of a 0.5 atm stoichiometric methane/air mixture for (a) a single pulse and (b) multiple pulses ($E=31.9~\mathrm{mJ~cm^{-3}}$, FWHM = 15 ns, and $f=100~\mathrm{kHz}$)	43
2.4	Compensated time to ignition $\tau/(p_0/p^*)^b$ for (a) methane/air and (b) ethylene/air stoichiometric mixtures ($T_0 = 800 \text{ K}$, $15 \leq \text{FWHM} \leq 60 \text{ ns}$) as a function of the dimensionless mean energy deposition rate W/W^* alongside fits of the form $\tau = C(W/W^*)^a(p_0/p^*)^b$: $C = 59 \mu\text{s}$, $a = -0.84$, and $b = 0.87$ for methane and $C = 29.9 \mu\text{s}$, $a = -0.72$, and $b = 0.66$ for ethylene.	45

2.5	Ratio of time to ignition $\xi = \tau/\tau_T$ for methane/air and ethylene/air as a function of p , keeping the energy per unit mass constant. The effect of (a) energy and (b) equivalence ratio are shown	47
2.6	Effect of equivalence ratio on ignition of ethylene-air mixtures for both plasma heating and direct (thermal) heating models ($p_0=0.5$ atm, $T_0=800$ K, FWHM = 10 ns, $f=200$ kHz, and $P=500$ kW/cm ³).	50
2.7	Ratio of time to ignition $\xi = \text{TTI}/\tau_T$ as a function of p_0 , keeping the energy per unit mass constant for (a) methane/air and (b) ethylene/air.	50
2.8	TTI as a function of energy deposition rate for 15 and 60 ns FWHM pulses at various f and P for methane/air mixtures (a) and ethylene/air mixtures (b)	53
2.9	TTI as a function of (a) pulse FWHM for constant W , f , and E and (b) pulse frequency for a constant W and FWHM	54
2.10	(a) Peak value of the mean electron energy ε_{max} during the first discharge pulse for two sets of power deposition rates, and ratio of vibrational excitation losses (Ω_v) , to electronic excitation losses (Ω_{el}) averaged over the first pulse, as a function of pressure. (b) Average radical production (kmol/m³-s) for the dataset described in Section 2.3.3, normalized by initial number density n_0 for CH ₄	56
2.11	Pathway analysis for O, H and OH during CH_4 ignition, averaged over the first two pulses for (a) 0.5 atm and (b) 30 atm, with the same pulsing conditions in Section 2.3.3. Percentages of production (blue) and consumption (red) are shown, along with average rates normalized by the initial number density n_0 . Arrow thickness is proportional to the average rate.	57
2.12	Pathway analysis for C_2H_4 ignition, averaged over the first two pulses for (a) 0.5 atm and (b) 30 atm, with the same pulsing conditions in Section 2.3.3	60
3.1	Normalized electron transport coefficients in a mixture of N_2 (79% by volume) and O_2 (21%) as a function of the reduced electric field E/N . Data calculated using BOLSIG+ and cross sections from the Morgan database [112]	65
3.2	Electrode configuration and applied voltage profile. Electrode boundaries are represented with solid lines, while far-field boundaries are shown with dotted lines	67
3.3	Electron mean free path for five gas mixtures as a function of the reduced electric field strength	68

3.4	Reduced electric field for the reference streamer case (case R). The cells of the finest grid level used to resolve the head of the positive streamer are clustered in regions of high reduced electric field gradient, and near the electrode surface, consistent with the tagging strategy discussed in section 3.1.7	79
3.5	(a) Electron number density n_e , (b) reduced electric field E/N , (c) sum of positive ion number densities n_+ , and (d) space charge density ρ_c for case R at 5 ns. A positive streamer emanates from the anode, forming a plasma channel with electrons and positive ions in its wake. A negative streamer with a lower degree of ionization propagates from the cathode. The cathode sheath is apparent as a region void of electrons surrounding the tip of the cathode	82
3.6	Evolution of the two streamers (case R). In each figure, the left panel shows the electron number density n_e and the right panel shows the reduced electric field strength E/N	83
3.7	(a) Charged species number densities and space charge density components (positive and negative), (b) reduced electric field, and potential along the axis for case R at 5 ns. The axial location with $y=0$ corresponds to the cathode tip, while $y=2.5$ corresponds to the anode tip	84
3.8	Charged species number densities and space charge density at the positive streamer head, taken along the axis for case R at 5 ns	86
3.9	Key quantities detailing the evolution of the positive streamer using centerline data from case R. The streamer ignition time t_{ig} corresponds to the maximum value observed in the time evolution of E/N_{peak} . The streamer position is indicated by h_l , defined as the distance of the streamer heat from the anode tip. The connection time t_{conn} is calculated as the time at which the streamer's head moves at its peak	07
3 10	Speed	87 88
	Drift and dielectric relaxation time step size restrictions for case R. (a) Electron number density n_e , (b) reduced electric field E/N , (c) sum of positive ion number densities n_+ , and (d) space charge density ρ_c near the cathode tip for case R at 5 ns	89
3.12	(a) Electron number density n_e with electric field lines and (b) potential ϕ for case R at 5 ns	90
3.13	Charged particle number densities and electron production rate near the cathode for case R at 5 ns, taken along the axis	91
3.14	Reduced electric field in the cathode region with control volumes for case R at 5 ns	92

3.15	Comparison of n_e (left panels) and E/N (right panels) near the cathode region at time $t=5$ ns, corresponding to cases R, B1, B2, and B3 respectively	93
3.16	Electron number density n_e (left panels) and reduced electric field strength E/N (right panels) at $t=4.5$ ns for cases (a) R, (b) B3, and (c)B4	94
3.17	Temporal evolution of (a) h_l , (b) E/N_{peak} , (c) δ_{sh} , and (d) ϕ_{cf} , along the axis, for different values of γ and electrode surface models	97
3.18	Evolution of the time step size constraint based on the electron drift velocity for streamers with γ ranging from 0.05 to 0 and including the "zero-gradient" boundary conditions (case B4)	98
3.19	Temporal evolution of (a) h_l , (b) E/N_{peak} , (c) δ_{sh} , and (d) ϕ_{cf} , taken along the axis of symmetry, for initial seed charge values of 10^{15} and 10^9 m ⁻³ , with and without photoionization	101
3.20	Temporal evolution of (a) h_l , (b) $E/N_{\rm peak}$, (c) δ_{sh} , and (d) ϕ_{cf} , taken along the axis of symmetry. Comparisons are made across cases using $r_c = 50$ and 300 μ m, $\ell = 2.5$ and 5 mm, and peak voltages ranging from 10 to 20 kV.	102
4.1	Electrode configuration; electrode surfaces are represented with solid lines, while far-field boundaries are shown with dotted lines	108
4.2	Temporal evolution of (a) electron number density and (b) gas temperature for various pulse strengths at atmospheric conditions	117
4.3	Temporal evolution of (a) electron number density and (b) gas temperature for various pulse strengths at $T_0 = 600$ K and $p_0 = 11.3$ atm	119
4.4	Deposited energy per particle as a function of the peak reduced electric field strength for the cases outlined in table 4.3	120
4.5	Streamer solution $(n_e, n_+, n_{N_2(v)}, n_{N_2^*}, n_{rad}, n_{prod}, T, \text{ and } p)$ at 6 ns. The plasma channel is comprised of a narrow region formed by the propagation of the positive streamer, and a broader region from by propagation of the negative streamer.	123
4.6	Reduced electric field and gas temperature along the axis of symmetry at 2.8 ns (solid lines), 3.7 ns (dashed lines), and 4.5 ns (dotted lines). Ignition of the positive streamer occurs at 2.6 ns, while streamer connection occurs at 3.7 ns	124
4.7	(a) Temporal evolution of the electron number density and reduced electric field strength at point 1, (b) temporal evolution of the temperature at point 1 and total energy deposited	126

4.8	(a) Number densities of excited state species, (b) number densities of radical and product species along the axis of symmetry at 6 ns	128
4.9	Temporal evolution of the total amount of cations, anions, vibrationally and electronically excited N ₂ , radicals, and products integrated across the entire domain, normalized using a reference gas mass $m_{\rm ref} = 2.29619 \times 10^{-6} \ {\rm g.}$	129
4.10	Radial profiles of the (a) charged particle number density, (b) excited species number density, (c) combustion radical number density, and (d) product number density and gas temperature, taken across the upper and lower portions of the plasma channel at 10 ns (solid), 100 ns (dashed), and 1 μ s (dotted)	132
4.11	Temporal evolution of (a) production and (b) consumption of O at point 2 driven by key reactions	135
4.12	Temporal evolution of (a) production and (b) consumption of H at point 2 driven by key reactions	136
4.13	Temporal evolution of (a) production and (b) consumption of OH at point 2 driven by key reactions	137
4.14	Heating and hydrodynamic expansion $(T, p, \rho, \text{ and } \boldsymbol{v})$ at 10 ns, 100 ns, and 1 μ m following the first pulse	139
4.15	Radial profiles of the gas pressure and velocity magnitude, taken across the plasma channel 0.05 mm from the anode tip at 10 ns (solid), 100 ns (dashed), and 1 μ s (dotted)	139
4.16	Temporal evolution during the first pulse (solid lines) and second pulse (dashed lines) of (a) electron number density and reduced electric field strength at point 3 and (b) temporal evolution of the temperature at point 3 and total energy deposited	142
4.17	Temporal evolution during the second pulse at 500 kHz (solid lines) and 200 kHz (dashed lines) of (a) electron and excited species number number densities and reduced electric field strength and (b) number densities of select combustion radicals and temperature at point 3	144
4.18	Temporal evolution of the total deposited energy scaled using the initial gas number density N_0 and a reference gas number density $(N_{ref}=2.446\times 10^{25}~{\rm m}^{-3})$ for the 300 K and 400 K cases	146
4.19	Comparison of the solution (number density of electrons, cations, combustion radicals, vibrationally and electronically excited N_2 , and combustion products, normalized by N_0) for the 300 K (left panels) and 400 K (right panels) cases at 6 ns	148

4.20	Temporal evolution during the first pulse for cases conducted at 300	
	K and 1 atm (solid lines) and 400 K and 2.7 atm (dashed lines) of (a)	
	the charged species number number densities and reduced electric field	
	strength, (b) excited species number densities, (c) combustion radicals	
	number densities, and (d) combustion product number densities and	
	temperature at point 3	150

Chapter 1

Introduction

Plasma-assisted ignition (PAI) has emerged in recent years as a promising alternative to traditional ignition [61], relying on the use of low-temperature plasmas (LTP) in place of spark discharges. In particular, nanosecond discharges (NSD) have been shown to enhance ignition and combustion under severe conditions (i.e. ignition of lean and diluted mixtures in internal combustion engines and ultra-lean gas turbines [138, 134, 100, 139, 143, 64], and supersonic combustion [80, 78]), actuate flow in supersonic environments [153], reduce pollutants and treat liquids [27, 44, 71], and promote fuel reforming [66]. The benefits include thermal heating, kinetic enhancements (for instance generation of combustion radicals such as O, H, and OH), and modification of transport properties [60].

Nanosecond discharges are characterized by an electron temperature that far exceeds the gas temperature $T_e \gg T_g$, along with high applied voltages $\mathcal{O}(1\text{-}100 \text{ kV})$ and reduced electric fields $\mathcal{O}(100\text{-}1000 \text{ Td})$, low to moderate currents $\mathcal{O}(1\text{-}10 \text{ A})$, and short durations $\mathcal{O}(1\text{-}10 \text{ ns})$ [152]. Such pulses are generated by applying a large voltage bias across two electrodes, resulting in the formation of a self-propagating ionization wave called a streamer, which leaves behind an initial channel of charged species with particle densities $\mathcal{O}(10^{18}\text{-}10^{22} \text{ m}^{-3})$ at atmospheric pressures. In most

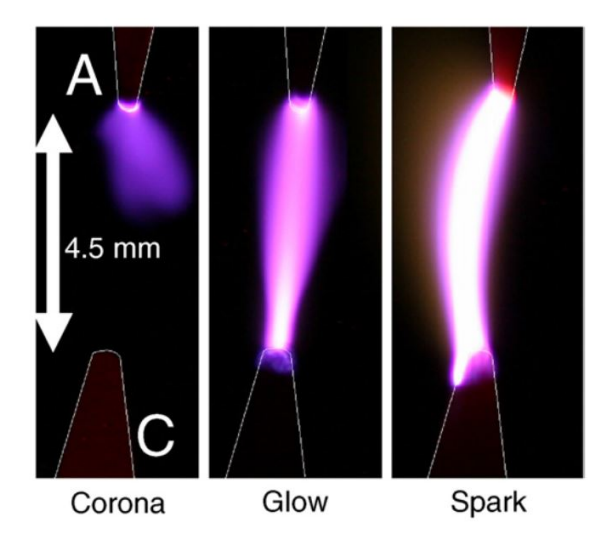


Figure 1.1: NSD in the corona, glow, and spark regimes in atmospheric air at $T_0 = 1000$ K. Adapted from [111].

applications of interest, the electrode gap has size $\mathcal{O}(1 - 10 \text{ mm})$, resulting in streamer radii $\mathcal{O}(0.1 - 1 \text{ mm})$. In order to prevent excessive heating of the gas, currents are generally held below $\mathcal{O}(10 \text{ A})$ [111].

1.1 Literature review

1.1.1 Discharge regimes

Understanding streamer dynamics remains a rich and complex problem, with a wide range of behaviors that can be elicited under different conditions. Experimental studies of pin-to-pin discharges have been conducted in order to define and understand different streamer regimes (corona, glow, and spark, as shown in figure 1.1) [110, 111, 109], which are characterized by differences in streamer structure, current, and gas heating.

Corona discharges are formed when the applied voltage is not sufficient to form a streamer that closes the electrode gap, instead forming a cloud of charged particles in the vicinity of the electrodes, with a small number of active particles and gas heating. Corona discharges enter the glow regime if the voltage is sufficiently high to allow the streamer to propagate across the gap, resulting in a channel of active particles, with modest currents and gas heating $\mathcal{O}(10\text{-}100\text{ K})$.

If the voltage source remains active past the glow phase, transition to the spark regime may occur, marked by large currents and significant localized heating (> 1000 K). Controlling the discharge regime is important when excessive heating is undesirable, for instance when NO_x emissions reduction or electrode erosion are concerns. Additional complexities have been observed experimentally in air at pressures $p \ge 1$ atm [115, 10], as streamer branching driven by stochastic photoionization processes results in the formation of a fractal-like structure, which is inherently three-dimensional.

1.1.2 Simulations of discharges in air

The numerical study of streamers presents an imposing set of obstacles, as large electric fields and tight coupling between the electric field and charged particles introduce sub-picosecond timescales, which are much smaller than the time scales of practical interest (≥ 1 ms for ignition and combustion applications). Issues of scale separation are further exacerbated by resolution requirements near the streamer head and at electrode boundaries, where $|\nabla \ln(n_e)|^{-1} \sim 10 \ \mu \text{m}$ or less. Such requirements imply micron-scale grid spacing, which is much smaller than the largest spatial scales

of the problem, such as the gap length.

Over the past decades, a large number of studies focused on simulating plasma discharges in air via pin-to-plane and pin-to-pin configurations [118, 159, 181, 182, 36, 136], taking advantage of the axisymmetric nature of the problem. Such simulations allowed for the exploration of many aspects of streamer propagation, including the dependence of the streamer's characteristics on the electrode geometry, voltage source, preionization and thermodynamic gap properties, gas heating effects, and photoionization. Still, axisymmetric approaches are inherently limited, as they are unable to describe streamer branching and streamer propagation in an inhomogeneous fluid where the inhomogeneities are three-dimensional as in configurations with mixture stratification due to turbulent mixing.

In more recent years, a number of three dimensional simulations have been conducted [94, 124, 157, 142], allowing for the investigation of stochastic streamer branching (as shown in figure 1.2), and streamer interactions. Still, limitations remain, as most three-dimensional studies relied on simplified kinetics models, electrode surface geometries, and transport equations. To date, the simulation of streamer propagation in a three-dimensional, inhomogeneous gas and simulations of discharges for plasma-assisted ignition using complex hydrocarbon/air mechanisms in three dimensions, are absent in the literature.

1.1.3 Electrode sheaths

Modeling choices at the electrode boundaries are particularly important. Under the influence of an applied voltage, the interaction of a charge-neutral plasma

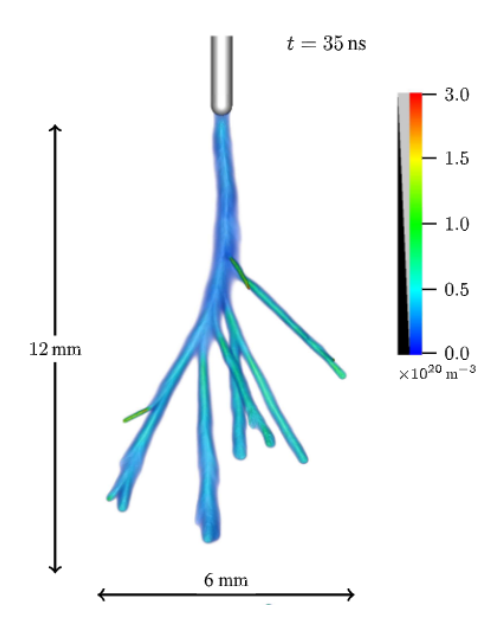


Figure 1.2: Streamer in atmospheric air at $T_0 = 300 \text{ K}$ with stochastic photoionization. Adapted from [95].

with a cathode surface results in a positively charged layer with a high space charge and electric field known as a cathode sheath [45], which forms as electrons are lost at the surface, and driven away by the electric field. The emission of secondary electrons from the cathode surface (whether due to photon and ion bombardment, thermionic emission, or other sources [186]) leads to charge multiplication as electrons are accelerated by the electric field, leading to further increases in the electric field strength, current, and charged particle gradients near the cathode. The simulation of plasma sheaths presents a significant challenge, driven by stringent requirements for spatial resolution and time step size as well as the formation of cathode "hot-spot" instabilities [92, 31, 32]. Early attempts at modeling the sheath region involved the use of "patching" methods [122, 83], which model the sheath and plasma regions of a

discharge separately, and rely on the application of appropriate boundary conditions between the different regions. More recent techniques have focused on reducing the stiffness associated with the sheath by calculating the electric field using Ohm's law rather than Gauss's law [120]. While such approaches have been successful in one-dimensional simulations, their applicability to multi-dimensional sheaths is untested.

1.1.4 Plasma-assisted ignition

1.1.4.1 Chemical and plasma kinetics and energy deposition

The problem is complicated considerably when multiple NSD are used to ignite a hydrocarbon/air mixture, due to disparate problem time scales and complex chemical kinetics. During each streamer propagation phase, electrons may attain a mean energy O(1-10) eV in the region in front of the streamer head, where space charge separation creates a strong electric field. Subsequent collisions with neutral air and hydrocarbon fuel particles may result in the generation of excited species and ions. Also important are electron impact dissociation processes, which directly generate combustion radicals and break down hydrocarbon fuel species, along with electron impact ionization, which is responsible for the creation of additional electrons and ions. The propagation of the plasma streamer, and generation of active particles through electron impact reactions typically occurs on time scales O(1-10) ns). Over longer periods of time O(100 ns) and under weaker electric field strengths, electron attachment and recombination processes play an important role in modifying space charge in the plasma channel.

Of particular importance are the electron collision processes that result in

the formation of electronically excited species, which can efficiently generate combustion radicals and promote "fast-heating" [128] of a gas mixture, occurring over O(10-100 ns), upon relaxation. The generation of and subsequent relaxation of vibrationally excited species is primarily responsible for "slow-heating" occurring over $O(1\text{-}10) \mu s$ [99, 74], and may also be of importance when multiple plasma pulses are considered.

As previously discussed, when a sufficiently strong applied voltage is maintained after streamer connection, Joule heating drives considerable increases in the gas temperature and pressure, the order of several hundred to a few thousand K and a few atm [177]. Since the heating occurs over \mathcal{O} (1-10) ns time scales, the heating is effectively isochoric. The subsequent hydrodynamic expansion phase [177, 160] occurs over $\mathcal{O}(1\text{-}10~\mu\text{s})$, and can support shock waves of moderate strength (as shown in figure 1.3) that necessitate a compressible treatment of the fluid. Accurate representation of the hydrodynamic expansion phase is crucial, as a sufficiently strong pulse can result in a considerable decrease in the gas number density, which in turn impacts subsequent pulses through changes in E/N.

1.1.4.2 Development of kinetics mechanisms

Major efforts have been made over to past few decades to better understand and model the broad problem of plasma-assisted combustion. Several experimental studies have focused on developing more accurate kinetic mechanisms describing the interactions of LTP with common hydrocarbon fuels [163, 174, 175, 41, 178, 77, 132, 166]. Such mechanisms can reach considerable levels of size and complexity,

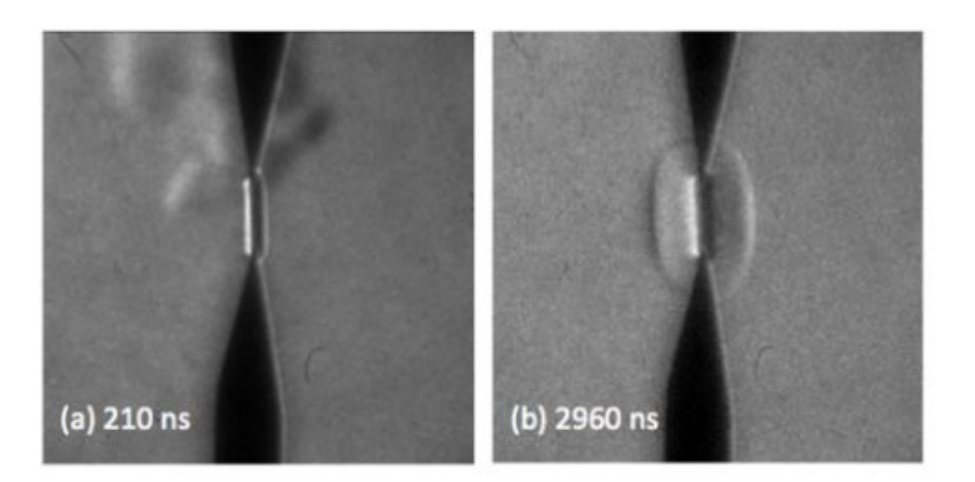


Figure 1.3: Schlieren images following a NSD in atmospheric air at $T_0 = 1000$ K in a pin-to-pin configuration. Adapted from [177].

especially when large hydrocarbons are included. A comprehensive mechanism would include, in addition to traditional combustion reactions, reactions describing electron interactions with ground state, excited, and ionized species. Such reactions result in the formation of a wide array of excited species, radicals, and ions, and may also include processes such as electron attachment and detachment, electron-ion and ion-ion recombination, and the quenching of excited species. While detailed kinetic mechanisms containing hundreds of species and thousands of reactions have been used to successfully investigate LTP behavior in zero-dimensional numerical reactors [5, 6, 163, 183, 39, 156, 166], such mechanisms are intractable for use in large-scale three-dimensional simulations due to excessive computational costs.

This has necessitated the development of new strategies for developing skeletal mechanisms that accurately describe the plasma-assisted ignition process. One common mechanism reduction strategy relies on representing the mechanism as a directed relation graph (DRG) [88, 155, 150, 82], where species in the mechanism are represented as nodes in the graph. Weighted edges are placed between species that interact directly through reactions, where the weights are correlated with the interaction strength. Targets (generally species or other quantities that need to be described accurately) are chosen, and the graph weights are used to quantify which species interact least with the targets. These species (and corresponding reactions) are discarded from the mechanism. This reduction procedure can be performed in an iterative manner, resulting in a hierarchy of smaller and smaller skeletal mechanisms, until some user-specified error tolerance is violated.

This approach has been effectively used to reduce various combustion mechanisms, and was extended in [17] to produce a reduced mechanism describing the oxidation of various hydrocarbon fuels using LTP. In this study a novel directed relation graph with error propagation (DRGEP) approach was used to reduce the detailed PAI mechanism from [41]. In this study, emphasis was placed on accurately representing the electron energy branching (which describes the pathways through which excited electrons deposit their energy through collisions with heavy species) by making it a reduction target. It was found that the detailed mechanism, which contained 163 species and 1167 reactions, could be reduced to 55 species and 222 reactions while still accurately describing the electron energy branching, as well as other important metrics such as the ignition time and adiabatic flame temperature.

1.1.4.3 Numerical investigations

The use of such a mechanism in multidimensional numerical studies represents an important step towards conducting predictive simulations of PAI. Advances in multidimensional PAI simulations have occurred primarily over the last decade, and have generally relied on a range of simplifying assumptions and empirical models. In [104], an uncoupled approach was used, whereby a two-dimensional methane/air streamer simulation consisting of three species was conducted, and used to initialize a one-dimensional simulation that described the gas dynamics in the channel. Special attention was paid to changes in the streamer properties due to the presence of methane, which was found to considerably reduce the impact of photoionization due to its large photon absorption cross section.

More recently, simulations of dielectric barrier discharges (DBD) in methane/air and NSD in hydrogen/air have been conducted in axisymmetric configurations using more detailed PAI kinetic mechanisms [68, 140, 93]. While these studies provided comprehensive overviews of the composition of the streamers during and after the pulse, evolution of the thermodynamic quantities was either modeled empirically, or neglected entirely. A recent methane/air study [23] extended previous work by using a three-dimensional PIC-MCC model to study the effect of methane addition on streamer properties and pulse energy deposition as shown in figure 1.4, but analysis was limited to the streamer propagation phase.

Efforts have been made to accurately simulate the full PAI ignition process as well. A semi-empirical model was developed in [29] to approximate the energy deposition from a NSD without explicitly solving equations for the charged particles

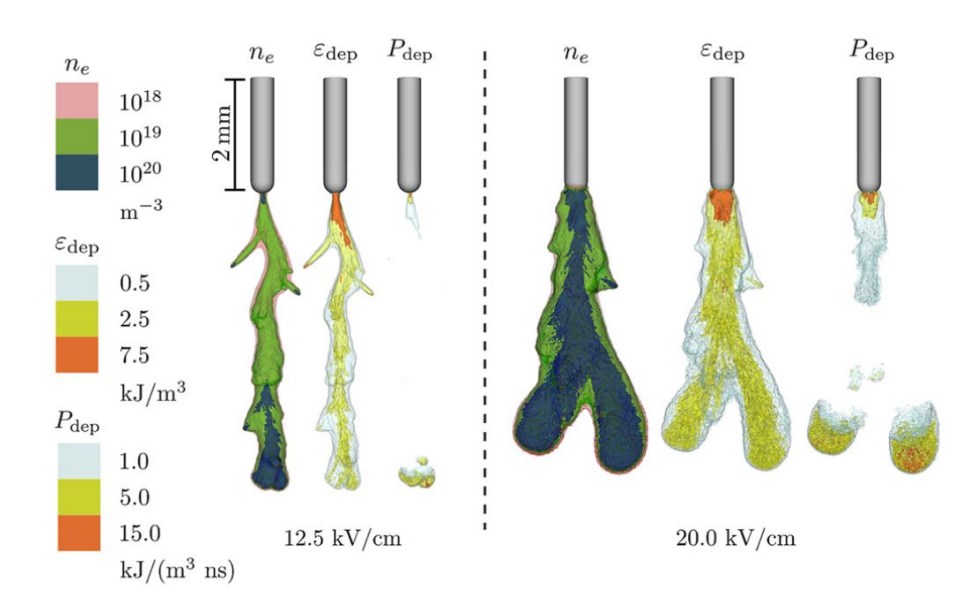


Figure 1.4: Contour surfaces for the electron number density, energy density, and power density deposition for streamers in a stoichiometric methane/air mixture at atmospheric conditions and $T_0 = 300$ K. Streamers are generated in a pin-to-plane configuration using different pulse voltage strengths. Adapted from [23].

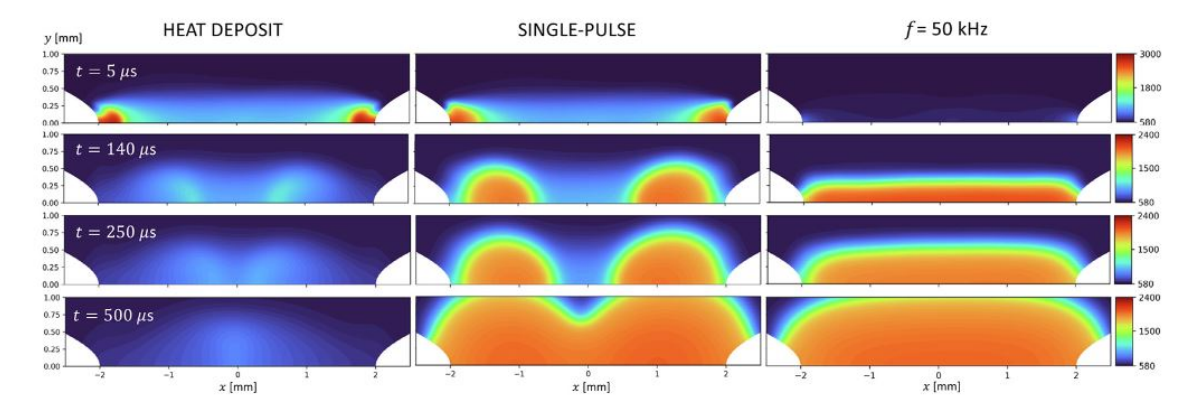


Figure 1.5: Temperature field at different instants in time for different energy deposition strategies, including direct energy deposition, application of a single NSD, and application of multiple NSD. Adapted from [14]

and electric field. This strategy was used in both three-dimensional [30] and axisymmetric configurations [15] to efficiently simulate the heating and ignition of various air/fuel mixtures across multiple pulses. Similar approaches were explored in [65]. Higher fidelity models have coupled the plasma fluid equations with a reactive flow solver [62, 140, 93, 147, 14] using both one-way and two-way coupling to study the PAI of hydrogen/air and methane/air mixtures (as shown in figure 1.5). The studies relied on axisymmetric configurations to minimize computational costs, and allow for more detailed chemical kinetic mechanisms. Such comprehensive approaches have not yet been used to conduct PAI simulations in three-dimensions.

This thesis seeks to resolve these gaps and limitations by conducting temporally and spatially-resolved simulations of the plasma-assisted oxidation of application-relevant hydrocarbon/air mixtures via multiple NSPD. Such a task is an inherently multi-faceted problem that necessitates a comprehensive understanding of a wide range of topics, ranging from chemical kinetics, to mechanism reduction, to large-

scale simulations of LTP. In Chap. 2, a high-fidelity plasma ignition kinetic mechanism is studied in 0D under a range of pressures and fuel-types. Next, the ignition and propagation of streamers in air is studied in Chap. 3 using a plasma fluid model which has been integrated into a reactive Navier-Stokes solver with adaptive mesh capabilities. The plasma sheath is characterized, and computational costs are assessed. Finally, a skeletal plasma ignition mechanism is used to simulate multiple pulses in an ethylene/air mixture in Chap. 4. A summary of the most impactful findings from this dissertation are provided in Chap. 5, along with recommendations for future areas of work aimed at further improving the predictive capabilities of the solver that has been developed.

Chapter 2

Impact of fuel type and pressure on plasma-assisted ignition

Investigation of plasma-assisted ignition begins with a zero-dimensional study aiming to quantify how important parameters such as the initial temperature, pressure, stoichiometry, and fuel type affect ignition of hydrocarbon air/mixtures. The ignition of methane/air and ethylene/air mixtures via NSPD is simulated in a zero-dimensional isochoric adiabatic reactor with a detailed mechanism featuring non-thermal plasma and combustion kinetics. A two-temperature model describes the non-thermal plasma generated during each pulse, as the strong electric field allows electrons to attain temperatures that are much higher than those of all other particles.

On the short time scale of a single nanosecond discharge, the transport of ions and other neutral particles is assumed negligible and spatial inhomogeneities in the concentrations of particles other than electrons are due to plasma kinetics rather than particle transport. Thus, while a zero-dimensional reactor model does not include transport effects, it describes energy exchanges due to plasma processes at the head of streamers and in the quasi-neutral region occupied by the streamer's body. Zero-dimensional plasma kinetic models are a well established approach in the

study of chemical plasmas [163].

2.1 Two-temperature reactor governing equations

The mathematical model consists of a set of ordinary differential equations (ODEs) that describe the evolution of the thermodynamic state of an ensemble of M species. The number density of each particle class is n_i , the internal energy density of the electrons is u_e , and u is the internal energy density of the ensemble of all other particles. The system of M + 2 ODEs reads

$$\frac{dn_i}{dt} = \omega_i \quad i = 1, \dots, M, \tag{2.1}$$

$$\frac{du_e}{dt} = Q_e \qquad \frac{du}{dt} = Q. \tag{2.2}$$

In the equations above, ω_i is the net rate of formation of particle i and Q_e and Q are the rate of energy gain for the electrons and all other particles. The electron energy source term reads

$$Q_e = 3k_B \left(\sum_{i=1, i \neq e}^M \nu_i^{el} \frac{m_e}{m_i} \right) n_e (T_e - T)$$
$$- \sum_{j=1}^R \delta \varepsilon_j \omega_e^j + Q_E(t). \tag{2.3}$$

The first and second terms in Eq. (2.3) represent energy transfers from electrons to other particles via elastic and inelastic collisions, respectively. m_i and m_e are the masses of species i and electron mass, ν_i^{el} is the elastic collision frequency between species i and the electron, T_e and T are the temperature of the electron and that of all other particles. $\delta \varepsilon_j$ is the energy lost by the electron in inelastic collision j occurring

at a rate ω_e^j . The third term in Eq. (2.3), $Q_E(t)$, represents the energy acquired by electrons from the electric field during each pulse. The internal energy source term for the ensemble of particles other than the electrons is $Q = -Q_e + Q_E(t)$.

The discharge consists of a sequence of pulses at frequency f. The energy density deposited by each pulse is E. The pulse power has a Gaussian profile with full-width-half-max FWHM, which describes the time between the two points on the Gaussian curve that are equal to half of the peak value. Pulses are centered at discrete times $t_k = t_1 + (k-1)/f$ with k = 2, ..., K. Thus, t_1 indicates the timing of peak power during the first pulse.

Thermodynamic properties and rate coefficients for all plasma processes and conventional combustion chemistry reactions are stored in CHEMKIN format and evaluated using the two-temperature extension of the CHEMKIN library [63]. More details about the kinetic model are provided below in Section 2.2. Time integration of the system of ODEs is performed efficiently with a variable time step and variable order Backward Differentiation Formula (BDF) implicit method as implemented in the CVODE solver [53].

2.2 Kinetic mechanism

The kinetic mechanism of Eckert et al. [41] for PAC applications is used in this study. The mechanism includes the electron, 2 ions $(O_2^+ \text{ and } N_2^+)$, 160 neutral species, and 1167 reactions and features various classes of electron/particle processes as well as conventional combustion chemistry. The combustion model describes the oxidation of H_2 , CH_4 , C_2H_4 , and C_3H_8 and has been validated for fuel lean and fuel

rich conditions at low and high temperatures and pressures up to 40 atm [69].

The set of plasma kinetics includes electron impact processes, whereby energetic electrons collide with ground state species (O_2 , N_2 , O, H_2 , CH_4 , C_2H_2 , C_2H_4 , C_3H_8), resulting in particle excitation, dissociation, and ionization. Vibrational excitation is included for N_2 , for which the first 8 vibrational levels are considered, along with electronically excited levels for O_2 , N_2 , and O, and corresponding de-excitation reactions. Reactions describing electron interactions with radicals and combustion products have been omitted in order to reduce the mechanism complexity at this stage.

The rate coefficients of collisions involving electrons and heavy species depend on the electron temperature and are not well-described by the Arrhenius form, necessitating special functional fits. The rate coefficients for all processes involving high-energy electrons in the mechanism from Ref. [41] were recomputed using the most recent cross section data from the LxCat database [112] and the Boltzmann kinetic solver BOLSIG+ [50], and parametrized as a function of T_e , using the JANEV functional forms available in CHEMKIN. The mechanism along with updated reactions is available in the appendix.

As described in [3], data from a series of low pressure (≤ 1 atm) experiments have been used to validate the mechanism extensively. The cross sections used by BOLSIG+ to model electron/neutral collisions are not measured or obtained theoretically at elevated pressures ($\gg 1$ atm), however it is generally understood that pressure effects are less important for two-body electron/molecule interactions. Quenching of vibrationally and electronically excited nitrogen and oxygen may be

impacted by elevated pressure, but the data in the literature are scarce.

2.2.1 Assumptions and limitations of the two-term approximation for the electron distribution function

BOLSIG+ solves an approximate form of the Boltzman equation (BE), which for electrons in an ionized gas is given as

$$\frac{\partial f_e}{\partial t} + \boldsymbol{u} \cdot \nabla f_e - \frac{e}{m_e} \boldsymbol{E} \cdot \nabla_{\boldsymbol{u}} f_e = C[f_e], \tag{2.4}$$

where f_e is the electron velocity distribution function, $\nabla_{\mathbf{u}}$ is the velocity-gradient operator, and $C[f_e]$ represents the rate of change of f_e due to collisions. To solve the BE, it is assumed that the electric field and collision probabilities are spatially uniform on scales comparable with the electron mean free path (MFP) λ_e . Under these assumptions f_e becomes symmetric in velocity space around the direction of \mathbf{E} , and can be rewritten in spherical coordinates as

$$\frac{\partial f_e}{\partial t} + v \cos \theta \frac{\partial f_e}{\partial z} - \frac{e}{m_e} E \left(\cos \theta \frac{\partial f_e}{\partial v} + \frac{\sin^2 \theta}{v} \frac{\partial f_e}{\partial \cos \theta} \right) = C[f_e], \tag{2.5}$$

where v, z, and θ are the velocity magnitude, direction of the electric field, and angle between the velocity and electric field direction, respectively. It is further assumed that the electric field and electron distribution are stationary on time scales comparable to the electron collision frequency ν .

The distribution function f_e is expanded using spherical harmonics, and the first two terms from the expansion are retained

$$f_e(v, \theta, z, t) = f_{e,0}(v, z, t) + f_{e,1}(v, z, t)\cos\theta,$$
 (2.6)

where $f_{e,0}$ and $f_{e,1}$ describe the isotropic component of f_e , and an anisotropic perturbation, respectively. It is known that more terms (6 or more) should be retained for high accuracy results, but the two-term approximation is widely used for the simulation of fluid discharges. The two-term approximation does however fail when the reduced electric field strength E/N is sufficiently large that f_e becomes highly anisotropic and collisions are mostly inelastic. Equation 2.6 is substituted into equation 2.5 and a system of two equations in the two unknowns $f_{e,0}$ and $f_{e,1}$ is solved (with further details available in [50]). Once the two functions are solved for, important parameters that depend on f_e are calculated, including electron transport and rate coefficients, collisional frequencies, and mean electron energies.

Thus, electron parameters account for departures of the electron energy distribution from a Maxwellian as well as for anisotropy brought by the directionality of the electric field, albeit only as described by the two-term approximation. More details about the consistency of the electron transport properties and the plasma fluid model are provided in [50].

For the work presented in this dissertation, relevant coefficients and parameters are evaluated via BOLSIG+ as functions of E/N for a fixed gas mixture (i.e. it is assumed that the gas composition, temperature, and pressure are constant). Gas mixture conditions for the simulations conducted and discussed in this dissertation, however, vary in both space and time, and changes in the gas composition and conditions can impact collision frequencies, and other parameters obtained from BOLSIG+. These effects are neglected entirely, although it is shown that their impact is modest in most cases.

The validity of the model and underlying assumptions can be evaluated by first examining the rate coefficients for selected elastic and inelastic collisions. To examine the effect of changes in the mixture conditions, three cases are considered: atmospheric air at 300 K, atmospheric air at 1000 K, and a stoichiometric ethylene/air mixture at atmospheric conditions and 300 K. Results are shown in figure 2.1 and show that the rate coefficient for selected elastic collision reaction is greater than rate coefficients for the selected inelastic collisions across the full range of reduced electric field strengths shown (which reflect the largest electric fields encountered throughout the work presented in this dissertation), indicating validity of the two-term approximation for the electron distribution function. It is also observed that changes in the mixture conditions have a modest impact on rate coefficients at lower field strengths, while there is almost no impact at stronger electric field strengths.

It is also important to consider the total electron/neutral collision frequency ν , which is provided in figure 2.2 for the same set of mixtures. It is observed that the collision frequencies ranges from $10^{11} < \nu < 10^{13}$ 1/s across the relevant set of reduced electric field strengths, implying collisional timescales $t_c = 1/\nu$ between 10^{-13} and 10^{-11} s. The assumption of a stationary electric field is thus judged to be reasonable, as $t_c \ll t_p \ll t_f$, where t_p is the timescale associated with the pulse duration, taken to be the range of pulse FWHM values considered $(1.5 \times 10^{-8} < t_p < 6 \times 10^{-8} \text{ s})$, and $t_f = 1/f$ is the timescale associated with the pulse frequency $(2 \times 10^{-6} < t_f < 2 \times 10^{-4} \text{ s})$.

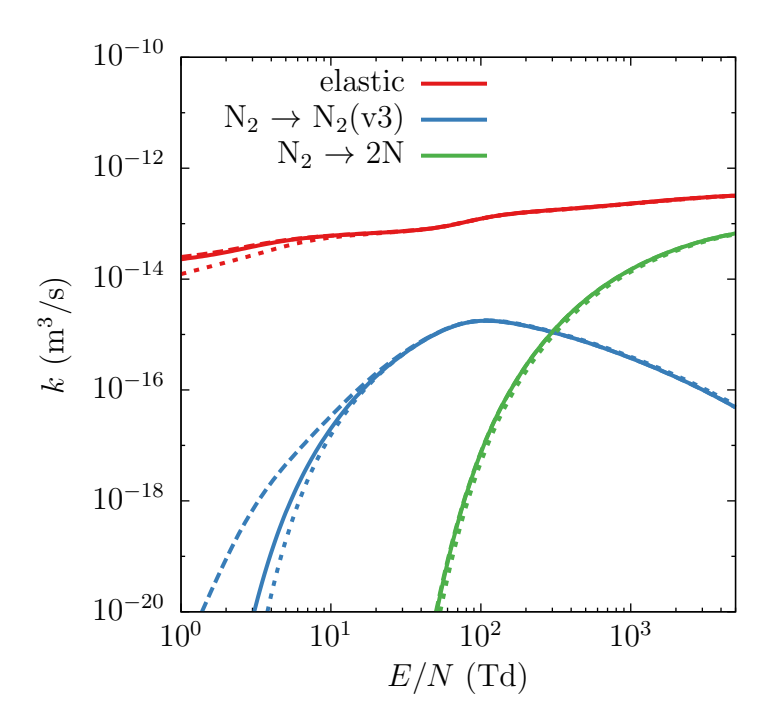


Figure 2.1: Rate coefficients for elastic collisions between electrons and N_2 (E + N_2 \rightarrow E + N_2), inelastic collisions resulting in vibrational excitation of N_2 (E + N_2 \rightarrow E + N_2 (v3)), and inelastic collisions resulting in dissociation of N_2 (E + N_2 \rightarrow E + 2N). Results are shown for atmospheric air at 300 K (solid lines), atmospheric air at 1000 K (dashed lines), and stoichiometric ethylene/air at atmospheric conditions and 300 K (dotted lines).

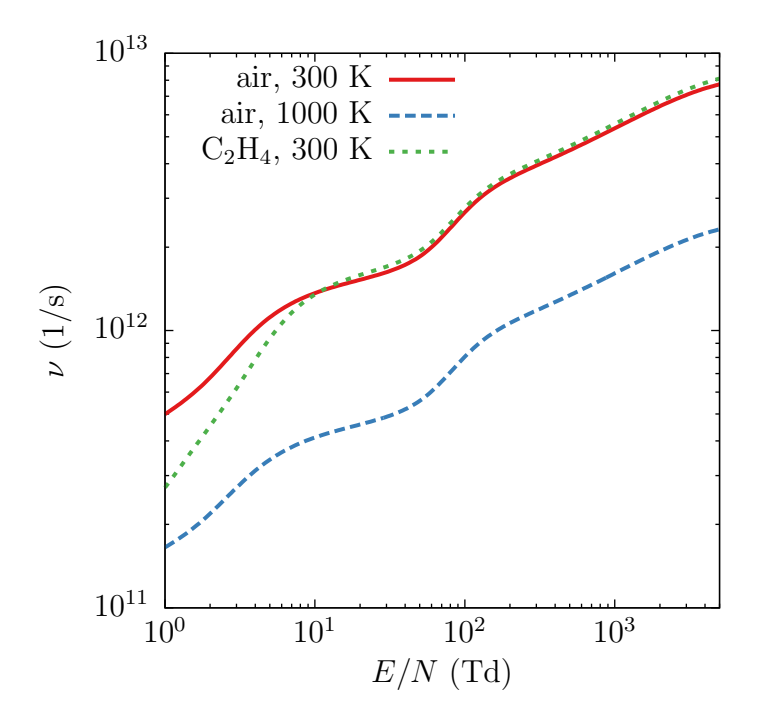


Figure 2.2: Electron collision rates as a function of the reduced electric field strength for the same mixtures at atmospheric pressure as in Fig. 2.1.

2.3 Results

2.3.1 Preliminaries and overview

PAI of fuel/air mixtures via NSPD is simulated with a two-temperature isochoric and adiabatic reactor. For all cases, the initial temperature T_0 is 800 K, which is representative of applications in power generation and hypersonics alike. The study considers methane and ethylene fuels, various stoichiometries, and initial pressures p_0 from 0.5 to 30 atm. While it is known that at elevated pressures, plasma streamers exhibit modified behavior, as they become filamentary in nature and the deposition of energy becomes less homogenous [141], these effects are are ignored in the present 0D study.

The discharge parameters are varied across a range of values that guarantee ignition within 100 μ s. Discharge frequencies between 5 and 500 kHz, FWHM between 15 and 60 ns, and single pulse energy densities between 15 and 15,000 mJ / cm³ are explored. A wide range of energy densities is explored due to the wide range of pressures. The reactor is initialized with pressure $p = p_0$, temperature $T = T_e = T_0$, and a mixture of fuel and air with equivalence ratio Φ .

Figure 2.3 presents an overview of the temporal evolution of the reactive mixture during a NSPD and is characteristic of all ignition events considered in this study. The values of energy density per pulse employed in the study are comparable to those in experimental studies on PAI. [76] report using 0.8-3.2 mJ per pulse in a discharge channel volume of \sim 17 mm³to ignite a mixture of methane and air at 1 atm and 850 K.

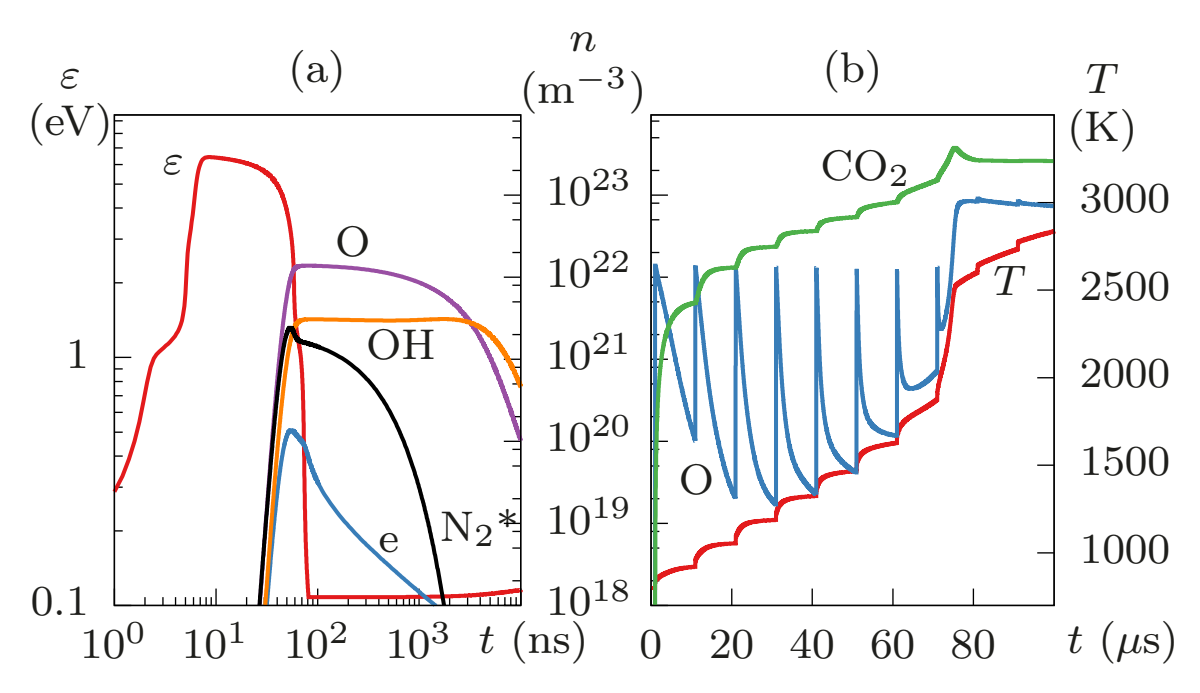


Figure 2.3: Time evolution of the mean electron energy ε , number density of select species and gas temperature during ignition of a 0.5 atm stoichiometric methane/air mixture for (a) a single pulse and (b) multiple pulses ($E=31.9~\mathrm{mJ~cm^{-3}}$, FWHM = 15 ns, and $f=100~\mathrm{kHz}$)

During each discharge, the electrons reach peak mean energies $\varepsilon \approx 6.5$ eV (before which an inflection corresponding to rapid vibrational excitation of N_2 is observed), followed by rapid cooling. Energetic electrons form excited state particles, mostly of O_2 and N_2 and the quenching reactions that follow excitation (e.g. $N_2^* + O_2 \rightarrow N_2 + 2O$) result in the formation of radicals as the excited particles thermalize. This process is known as *ultra-fast heating* [144], marked by a modest increase in T.

Across multiple pulses, radicals and transient species exhibit sawtooth profiles shown by the O radical. As reactants are consumed, the peak concentrations of combustion radicals during each pulse decrease, though this trend is not visible in the log scale in Fig. 1. After a number of pulses, the concentration of carbon dioxide increases abruptly, signaling that conventional exothermic reactions undergo a rapid acceleration consistent with an *ignition event*. Thus, the instant in time when the rate of change of the number density of CO_2 peaks is taken to represent the time of ignition t^* . Then, the *time to ignition* (TTI) is defined as $\tau = t^* - t_1$, where t_1 is the timing of the peak discharge power during the first pulse. Thus, τ represents the interval between the first pulse and ignition. Following ignition, the gas temperature continues increasing due to the relaxation of the remaining excited species, eventually reaching a thermochemical equilibrium.

2.3.2 Pressure effects on τ

Achieving fast and reliable ignition requires understanding the factors that impact τ most. We found that fuel type, mean energy deposition rate W = Ef, and initial pressure p_0 account for most of the variation in the time to ignition across

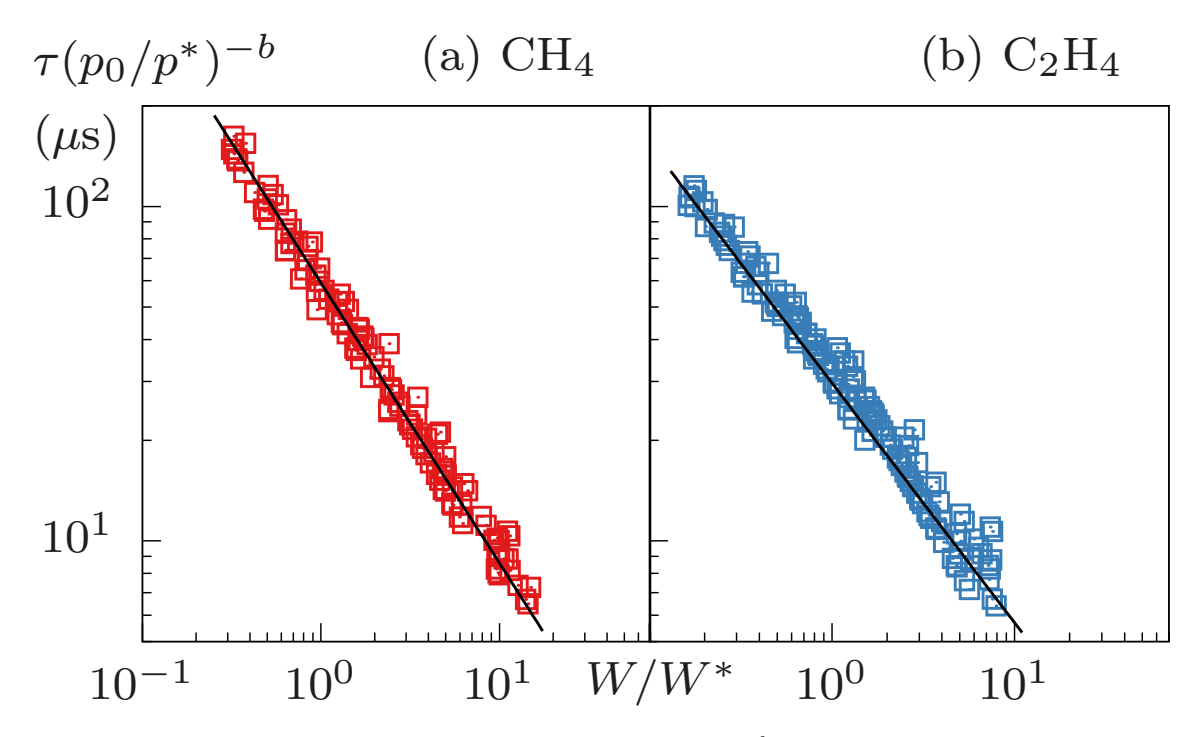


Figure 2.4: Compensated time to ignition $\tau/(p_0/p^*)^b$ for (a) methane/air and (b) ethylene/air stoichiometric mixtures ($T_0 = 800 \text{ K}$, $15 \leq \text{FWHM} \leq 60 \text{ ns}$)as a function of the dimensionless mean energy deposition rate W/W^* alongside fits of the form $\tau = C(W/W^*)^a(p_0/p^*)^b$: $C = 59 \mu\text{s}$, a = -0.84, and b = 0.87 for methane and $C = 29.9 \mu\text{s}$, a = -0.72, and b = 0.66 for ethylene.

cases.

Figure 2.4 shows τ for stoichiometric mixtures of methane/air and ethylene/air at 800 K and several combinations of $15 \le E \le 15,000$ mJ cm⁻³, $5 \le f \le 500$ kHz, $15 \le \text{FWHM} \le 60$ ns, and $0.5 \le p_0 \le 30$ atm. The data are reported in compensated form $\tau/(p_0/p^*)^b$ versus W/W^* , where $p^* = 1$ atm and $W^* = 10$ kW cm⁻³ are reference quantities. Fits of the form $\tau = C(W/W^*)^a(p_0/p^*)^b$ are shown alongside the data from simulations and the parameters are provided in the caption for methane and ethylene.

Several important conclusions can be drawn from Fig. 2.4. First, τ depends on the energy deposition rate W = Ef and not on the energy density per pulse E and pulse frequency f, separately. In other words, less energetic and more frequent pulses are equivalent to more energetic and less frequent pulses. Second, τ decreases as the mean energy deposition rate W increases, so that faster ignition is achieved by either increasing energy density E or frequency f. Third, the power law model is broadly consistent with the ignition behavior of the two reactive mixtures, so that $\tau \sim p_0^b$ at constant mean energy deposition rate and $\tau \sim W^a$ at constant pressure. The agreement is rather convincing, especially because the ranges of values spanned by τ , W and p_0 are broad, encompassing values relevant to applications.

Finally, the response of τ to changes in p_0 and W, pressure and power, are distinctly different for methane and ethylene. According to the model, $W \sim p_0^{-b/a}$ for constant τ , so that -b/a = 1.04 for methane and -b/a = 0.92 for ethylene, pointing to the fact that the energy per unit mass of the mixture required to keep τ constant increases as pressure increases for methane/air, while it decreases for ethylene/air mixtures. This highlights an important sensitivity of the kinetics of PAI to pressure and fuel type.

2.3.3 Pressure effects on plasma and combustion kinetics

In order to separate the contributions of plasma kinetics and combustion chemistry to the dependence of τ on pressure, we conducted additional simulations with direct heating of the gas. In these auxiliary simulations, the power Q_E is delivered directly to the gas, defined here as the collection of all particles other than

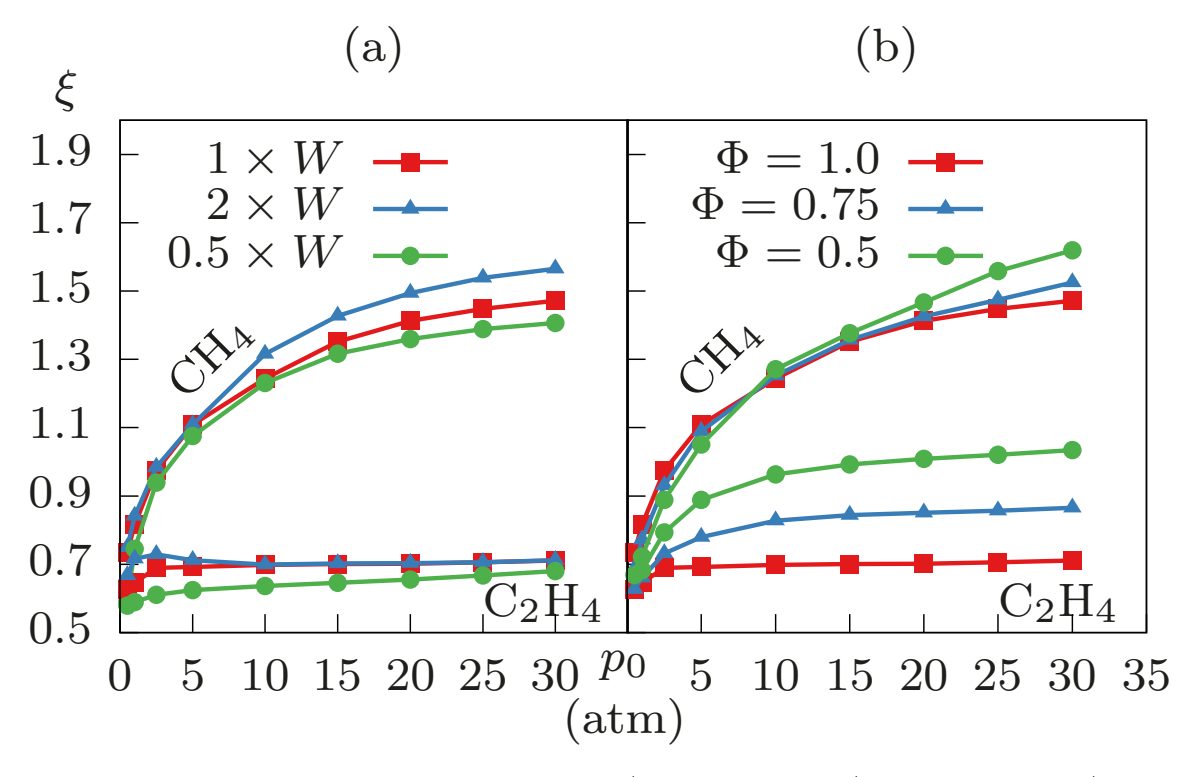


Figure 2.5: Ratio of time to ignition $\xi = \tau/\tau_T$ for methane/air and ethylene/air as a function of p, keeping the energy per unit mass constant. The effect of (a) energy and (b) equivalence ratio are shown.

electrons. This approach results in thermal heating of the mixture on the same time scales of the discharge pulses without the generation of high-energy electrons responsible for the production of radicals.

The time to ignition with direct gas heating is indicated with τ_T and the ratio $\xi = \tau/\tau_T$ is defined and shown in Fig. 2.5 as a function of pressure for the two fuels, mixtures of varying stoichiometry, and several mean energy deposition rates. The data are obtained as follows. Starting from $p_0 = 0.5$ atm and W = 34 kJ cm⁻³ s⁻¹, the pressure is varied and W is adjusted in order to keep the mean energy deposition

rate per unit mass constant. In practice, this means that as p_0 increases, W increases by the same factor. The FWHM is held constant and equal to 15 ns and the frequency is f = 100 kHz for all cases. The same simulations are repeated for $\Phi = 1.0, 0.75, 0.5$, and for higher and lower values of W in order to explore the dependence of ξ on Φ and W.

The following trends are apparent in Fig. 2.5. First, $\xi \leq 1.0$ for nearly all ethylene/air mixtures and all cases considered, indicating that PAI of ethylene is energetically more efficient than ignition via direct gas heating (meaning the same power deposition leads to a faster ignition). Interestingly, the same remains true even as pressure increases, which suppresses radical production as discussed later. Nonetheless, ξ does display a minor increase with increasing pressure. Second, $\xi < 1$ at low pressures ($p_0 < 3$ atm) for methane/air mixtures, while ξ becomes greater than unity and continues to grow as pressure rises. This trend points to a loss of efficiency of PAI of methane for higher pressures. Third, the two conclusions hold true qualitatively even as the equivalence ratio and the mean energy deposition rate change. Fourth, a dependence of ξ on Φ for C_2H_4 ignition is observed, as decreasing Φ leads to less C_2H_4 oxidation, lower amounts of heat release, and thus less efficient ignition.

To conclude, PAI loses its advantages in terms of shorter τ as pressure increases, but the value and rate of increase of the ratio τ/τ_T differ significantly for methane/air and ethylene/air mixtures.

2.3.4 Stoichiometry effects on ignition efficiency

Ignition efficiency and flame stability are of great importance when it comes to the combustion of both methane/air and ethylene/air mixtures. Ethylene is a proxy for fuels used in supersonic combustion; conditions in supersonic combustors are often highly turbulent and chaotic, and mixture properties such as local equivalence ratio can vary greatly from location to location. Methane is used as a fuel in gas turbines for power generation, where lean conditions and high pressures can create problems for flame stability.

In order to explore the effect of non-equilibrium plasma on mixtures of varying equivalence ratio Φ , a series of ethylene/air simulations have been run for $p_0 = 0.5$ atm and $T_0 = 800$ K. Pulse settings have been kept the same for each simulation, with pulse FWHM = 10 ns, f = 200 kHz, P = 500 kW/cm³. Enough pulses have been used to ensure that for each simulation, ignition occurs prior to the final pulse. Results for both plasma heating and direct heating strategies are presented in Fig. 2.6:

As seen in section 2.3.3, for ethylene/air mixtures, the plasma heating is a more efficient strategy than direct heating across pressures. This trend holds true across equivalence ratios as well. It is also interesting to note that peak ignition efficiency occurs at different points for each strategy, with ignition occurring earliest at stoichiometric and slightly fuel rich conditions for the plasma heating strategy, and at lean conditions in the case of direct heating. As expected, as conditions become very lean or very rich, ignition efficiency drops.

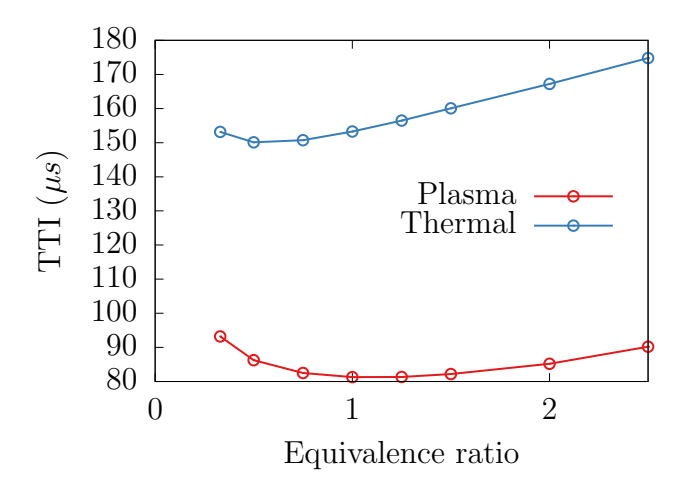


Figure 2.6: Effect of equivalence ratio on ignition of ethylene-air mixtures for both plasma heating and direct (thermal) heating models ($p_0 = 0.5$ atm, $T_0 = 800$ K, FWHM = 10 ns, f = 200 kHz, and P = 500 kW/cm³).

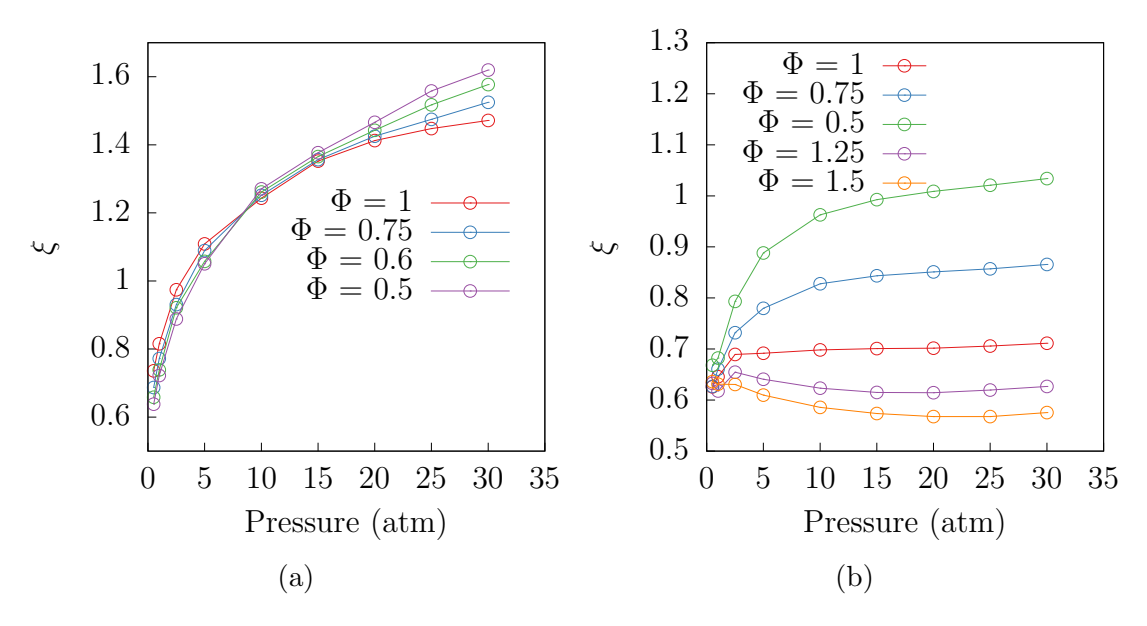


Figure 2.7: Ratio of time to ignition $\xi = \text{TTI}/\tau_T$ as a function of p_0 , keeping the energy per unit mass constant for (a) methane/air and (b) ethylene/air.

The analysis presented in section 2.3.3 is expanded to include equivalence ratio effects. As before, a series of methane/air and ethylene/air simulations are run for $0.5 < p_0 < 30$ atm, with $0.5 < \Phi < 1,.0$ for methane, and $0.5 < \Phi < 1.5$ for ethylene. The pulse settings used were FWHM = 15 ns and f = 100 kHz. Starting from $p_0 = 0.5$ atm and W = 3.4 kJ cm⁻³ s⁻¹, the pressure is varied and W is adjusted in order to keep the mean energy deposition rate per unit mass constant. Results are presented for methane/air and ethylene air in Fig. 2.7.

Several conclusions can be drawn from the results. First, it is apparent that in comparison with ethylene, methane ignition is fairly insensitive to equivalence ratio, as the trends in pressure observed at stoichiometric conditions persist for leaner mixtures. At higher pressures ($p_0 > 20$ atm), there is a minor equivalence ratio effect, with leaner mixtures taking a relatively longer amount of time to ignite (compared with the thermal ignition time τ_T).

Ethylene ignition, in contrast shows a greater dependence on equivalence ratio. It is apparent that the trends shown in Fig. 2.6 for $\Phi=0.5$ persist at higher pressures as well. For a given pressure, plasma ignition performs best under slightly fuel-rich conditions, while thermal ignition performs well under slightly lean conditions. The equivalence ratio and pressure trends interact, leading to an appreciable decrease in ignition efficiency for lean fuels under high pressure conditions. In fact, for the leanest mixtures tested in this study ($\Phi=0.5$), thermal ignition outperforms plasma ignition ($\xi>1$) for pressures exceeding 20 atm.

An interesting departure in these trends is observed for fuel-rich ethylene/air mixtures. In contrast to all other cases discussed, plasma ignition efficiency actually

improves relative to thermal ignition with increasing pressure. This would indicate that the trends observed in Fig. 2.6 become exaggerated as pressure increases.

2.3.5 Impact of pulse frequency and duration on ignition

The impact of pulsing parameters on TTI was investigated using stoichiometric methane/air and ethylene/air mixtures at 0.5 atm, and 800 K, characteristic of the conditions seen in supersonic combustion applications. Pulse frequency f has been varied from 5-500 kHz, peak power density P is varied from 500 - 480,000 kW/cm³, and pulse FWHM is varied from 15-120 ns. Given the Gaussian pulse profile used in the study, P and FWHM can be used to calculate the energy density per pulse as $E = P\sqrt{2\pi}\sigma$, with $\sigma = \text{FWHM}/(2\sqrt{2\ln 2})$. TTI for each case can then be plotted against the energy deposition rate W, calculated as Ef. Results are presented in Fig. 2.8 for methane (a) and ethylene (b).

Several conclusions can be drawn immediately from the data. First both fuels display a power law dependence of TTI on W, with faster ignition obtained for larger energy deposition rates. Since the energy deposition rate is the product of the pulse frequency and the energy density per pulse, one can conclude that these two factors alone do not play a primary role in determining TTI, and that weaker, more frequent pulses are roughly equivalent to stronger, infrequent pulses. Second, for a given W, ethylene ignites more readily than does methane.

For a given W, a larger FWHM corresponds with a lower peak pulse power P, while the opposite is true for shorter FWHM values. Finally, it appears that there is a secondary effect of pulse FWHM on TTI. This is seen more clearly in Fig. 2.9a, which

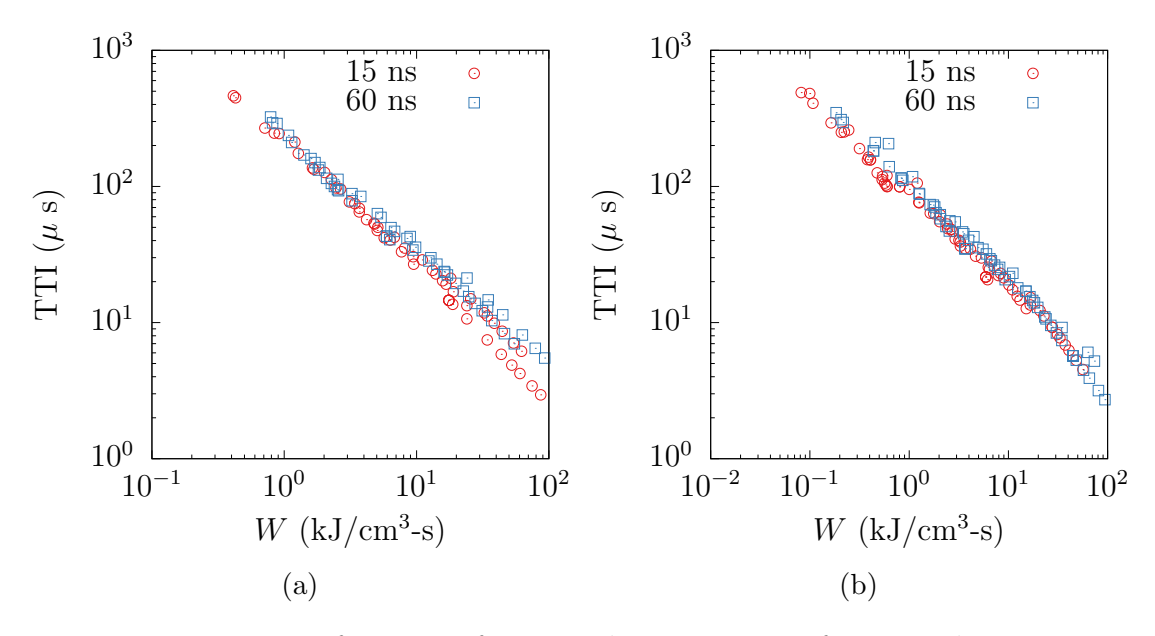


Figure 2.8: TTI as a function of energy deposition rate for 15 and 60 ns FWHM pulses at various f and P for methane/air mixtures (a) and ethylene/air mixtures (b).

illustrates the impact of pulse FWHM on TTI for both fuels, for an energy deposition rate of 3.2 kW/cm^3 , a pulse frequency of 100 kHz, and a single-pulse energy density of 32 mJ/cm^3 . In order to keep E constant, the peak pulse power P is increased in proportion with decreases in FWHM. As FWHM decreases and P increases, the mixture ignites more efficiently, as a shorter TTI is achieved with the same power deposition. In addition, the dependence of TTI on f is shown in Fig. 2.9b, with a fixed energy deposition rate of 3.2 kW/cm^3 , and a pulse FWHM of 15 ns. In order to hold W constant, the single-pulse energy density E is increased proportionally with decreases in f. It is apparent that all else held constant, lower pulse frequencies, and thus higher single-pulse energy densities, lead to a more efficient ignition.

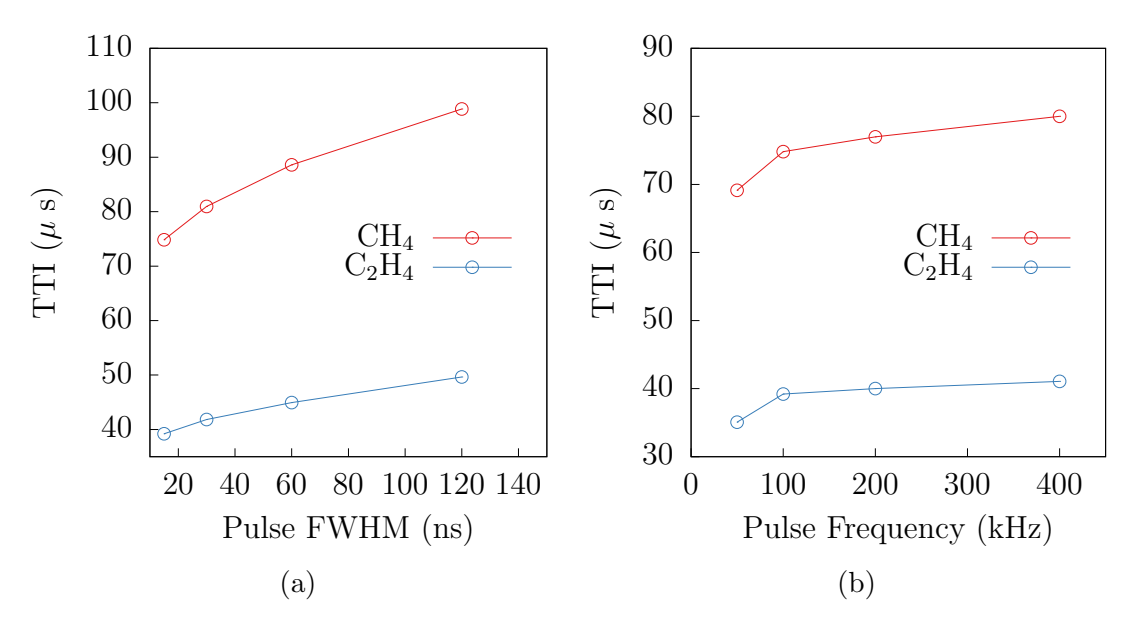


Figure 2.9: TTI as a function of (a) pulse FWHM for constant W, f, and E and (b) pulse frequency for a constant W and FWHM.

To summarize, TTI is primarily governed by the energy deposition rate, as previously observed. Secondary dependencies of TTI on pulse FWHM (holding W, f, and E constant), and pulse frequency (holding W and FWHM constant) are also observed. It is found that for a given energy deposition rate, higher peak pulse powers and single-pulse energy densities are preferable for obtaining a faster ignition.

2.3.6 Radical production

One primary mechanism leading to loss of efficiency for PAI as pressure increases is related to the dependence of the peak mean electron energy ε_{max} on pressure p_0 . As shown in Fig. 2.10a, the peak mean electron energy drops rapidly as pressure increases. It is also apparent that increasing the mean energy deposition rate W by

increasing the energy density deposited with each pulse E does not impact the effect of pressure on ε_{max} . These trends are general and independent of the fuel/air mixture composition on the account that ε_{max} is controlled by the collisions of electrons with air molecules.

The decrease in ε_{max} with pressure has important implications for the generation of excited species and radical production. The electron energy distribution function and the associated mean electron energy control electron/particle interactions. This is due to the fact that inelastic collisions have specific energy thresholds. Vibrational excitation of N_2 requires an electron energy in the range of 0.1 to 3 eV, while electronic excitation of N_2 , dissociation, and ionization require higher energies, in the range of 6 to 16 eV.

Thus, the lower the pressure, the higher the mean electron energy and the greater the rates of production of electronically excited N_2 , which is efficient at creating O radicals through collision with O_2 . Conversely, as pressure increases, the discharge energy contributes mostly to the vibrational excitation of N_2 , which does not lead to the production of radicals. This also explains the energy budgets in less efficient ignition cases (for a given input energy).

The dependence of the so-called *energy branching* of the plasma discharge on pressure is well known and shown in Fig. 2.10a, which depicts the ratio of electronic and vibrational electron energy losses (Ω_{el}/Ω_v) , averaged over 10 μ s (one pulse).

The impact this has on the generation of radicals is demonstrated in Fig. 2.10b, which shows the pulse-averaged rate of production of combustion radicals as a func-

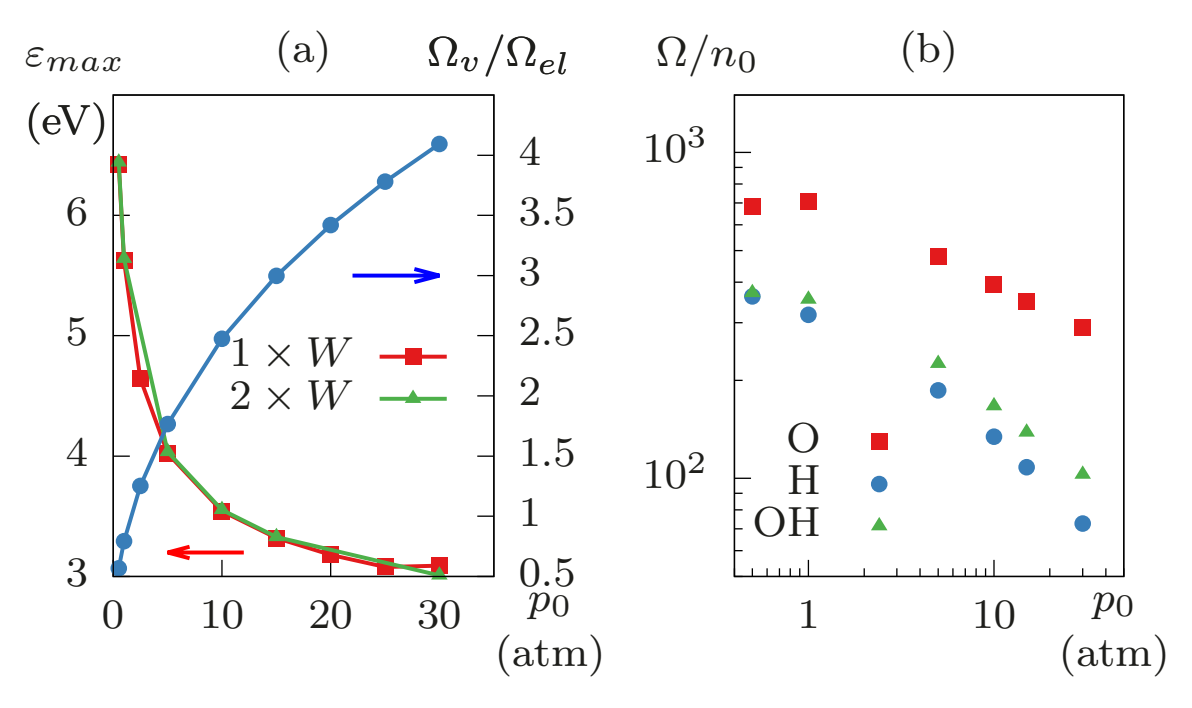


Figure 2.10: (a) Peak value of the mean electron energy ε_{max} during the first discharge pulse for two sets of power deposition rates, and ratio of vibrational excitation losses (Ω_v) , to electronic excitation losses (Ω_{el}) averaged over the first pulse, as a function of pressure. (b) Average radical production (kmol/m³-s) for the dataset described in Section 2.3.3, normalized by initial number density n_0 for CH₄.

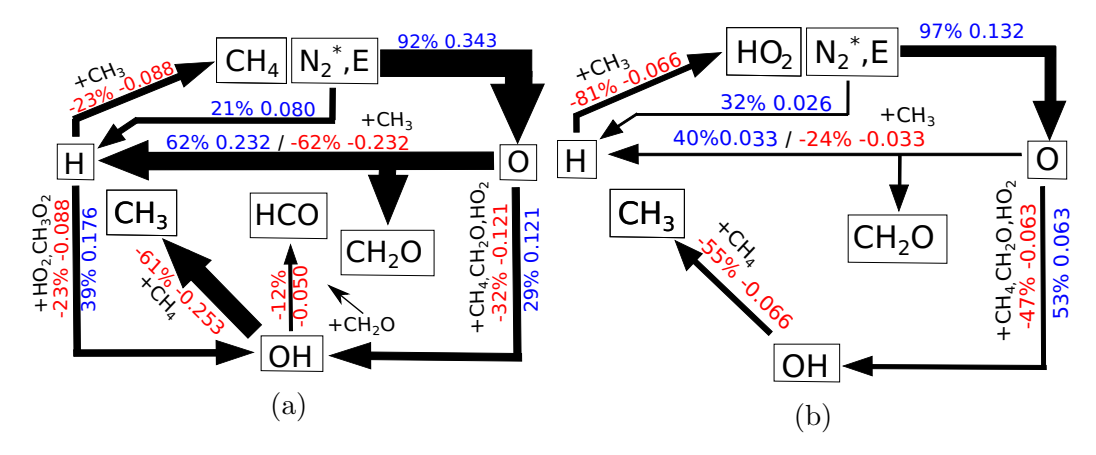


Figure 2.11: Pathway analysis for O, H and OH during CH_4 ignition, averaged over the first two pulses for (a) 0.5 atm and (b) 30 atm, with the same pulsing conditions in Section 2.3.3. Percentages of production (blue) and consumption (red) are shown, along with average rates normalized by the initial number density n_0 . Arrow thickness is proportional to the average rate.

tion of pressure. The rate of production is normalized by the initial number density n_0 in order to compensate for the increase in mixture density brought by pressure. It is apparent that the normalized rate of formation of all three radicals decreases as pressure increases. A similar decrease in the rates of formation of radicals in ethylene/air mixtures is found (not shown).

2.3.7 Fuel effects

A comprehensive analysis of the kinetics processes responsible for the loss of efficiency of PAI in methane/air mixtures with pressure and the resilience of the same PAI in ethylene/air is presented next by considering detailed pathways for low and high pressure ignition cases. The low pressure case features $p_0 = 0.5$ atm and W = 34 kW cm⁻³, while the high pressure case features $p_0 = 30$ atm and

 $W = 2.04 \text{ MW cm}^{-3}$, so that the mean energy deposition rate is scaled in order to keep the energy per unit mass constant.

In Fig. 2.11, nodes indicate species and arrows indicate reactions. For the sake of clarity, only the major pathways are shown. For each plot, the thickness of the arrows is proportional to the normalized rate of progress of the specific reaction averaged over 20 μ s (two pulses). The rates are normalized by n_0 to account for variations brought by density and pressure and facilitate comparisons between the low and high pressure cases. Percentages next to the rates are computed for each reaction relative to the total rate of formation (positive numbers) or total rate of destruction (negative numbers) for the radicals involved in each reaction.

We begin by considering the pathways involving O, H, and OH in Fig. 2.11a and Fig. 2.11b, respectively. While the data are shown for methane/air ignition similar results are obtained for ethylene/air because the plasma reactions involved pertain to air mostly.

Plasma reactions are responsible for 92% to 96% of the rate of formation of O and for a more modest contribution to H (20 to 32% at low and high pressure), mainly through collisions of CH_4 with electrons and electronically excited N_2 . We find that O radicals are crucial in the breakdown of methyl radicals through $CH_3 + O \longrightarrow CH_2O + H$, which is also an important source of H. O promotes ignition via attacks on methane to form methyl ($CH_4 + O \longrightarrow CH_3 + OH$) and on formaldehyde to produce formyl ($CH_2O + O \longrightarrow HCO + OH$). At low pressure, H contributes to the formation of OH via the breakdown of hydroperoxyl ($HO_2 + H \longrightarrow 2OH$). These sources of OH account for 2/3 of the overall production of OH, which is the

radical most involved in the abstraction of hydrogen from CH₄.

At this point, it is important to recall that methane oxidation to carbon monoxide proceeds through a sequence of intermediates, $CH_4 \longrightarrow CH_3 \longrightarrow CH_2O \longrightarrow HCO \longrightarrow CO$, whereby the first three steps require radicals. First hydrogen abstraction from CH_4 to form the methyl radical CH_3 requires any one of O, H, or OH. Next, the formation of CH_2O is mostly due to $CH_3 + O \longrightarrow CH_2O + H$. Most importantly, the key step $CH_2O + H \longrightarrow HCO + H_2$ requires the H radical. The formyl radical then reacts with O_2 to form CO.

In the high-pressure case, H is consumed by the reaction $H + O_2 \longrightarrow HO_2$ instead, which is a well known chain-termination step given that HO_2 is a rather stable species. Thus, regardless of the rates of formation of O and, subsequently, of all other radicals, the destruction of H to form HO_2 conspires to slow down the conversion of formaldehyde to formyl. At low pressure, this is the largest source of HCO, accounting for 41% of production. Instead, it becomes insignificant as pressure increases. Since this is the primary pathway for HCO production, this bottleneck also limits the production of CO and ultimately CO_2 , severely mitigating the benefits of radicals produced via discharges. For every mole of methane converted to methyl, less than 0.09 moles of CO are created at high pressure. In contrast, around 0.29 moles of CO are created for each mole of CH_3 at low pressure.

Although not shown, the pathways of radical formation and consumption are very similar for ethylene/air mixtures. In particular, the same pathways leading to the consumption of H to form HO₂ are active in ethylene/air mixtures at high pressure also, but they appear to be inconsequential to the efficiency of PAI. As shown

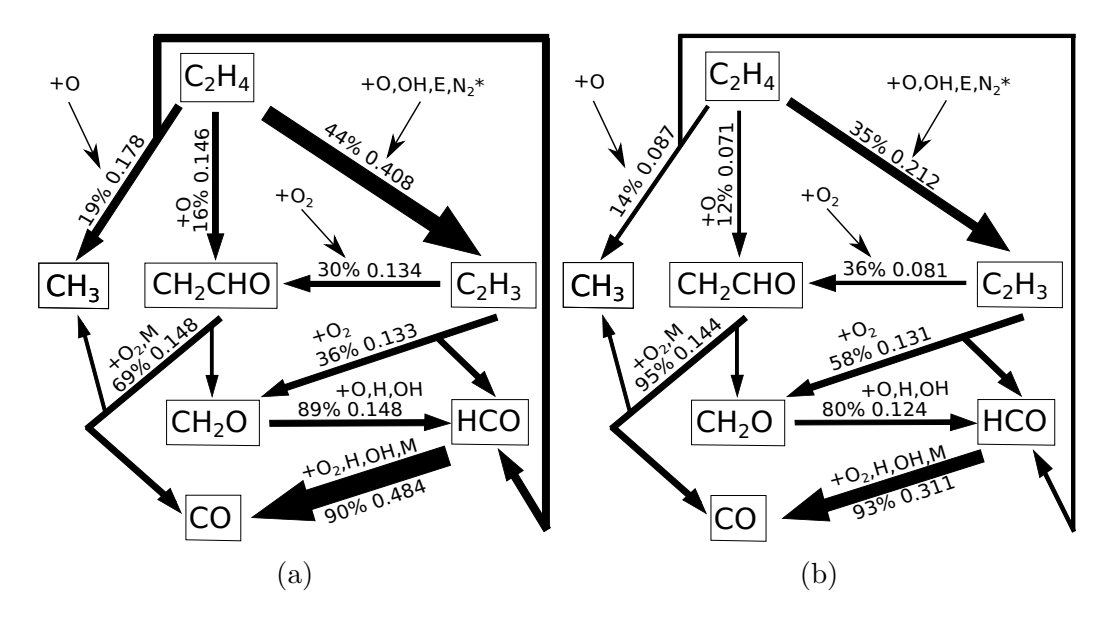


Figure 2.12: Pathway analysis for C_2H_4 ignition, averaged over the first two pulses for (a) 0.5 atm and (b) 30 atm, with the same pulsing conditions in Section 2.3.3.

in Fig. 2.5, the ignition of stoichiometric ethylene/air mixtures via plasma discharges and radical production is not hindered significantly at high pressure compared to direct gas heating. The source for this peculiar behavior lies in the more complex network of reactions that lead to the formation of HCO in ethylene/air mixtures compared to methane/air.

Figure 2.12 shows the pathways of ethylene oxidation at low pressure. Compared to methane, ethylene oxidation occurs through a more complex network of reactions, starting with the initial H-abstraction from ethylene, primarily through attacks by O and OH. This results in the formation of ethylenyl C_2H_3 ($C_2H_4 + O \longrightarrow C_2H_3 + OH$ and $C_2H_4 + OH \longrightarrow C_2H_3 + H_2O$), vinoxy CH_2CHO ($C_2H_4 + O \longrightarrow CH_2CHO + H$), and methyl radicals ($C_2H_4 + O \longrightarrow CH_3 + HCO$). In

particular, the last of these reactions is significant, as it bypasses the bottleneck $CH_2O \longrightarrow HCO$ and allows for the direct formation of HCO, which is then converted to CO.

Ethylenyl is attacked primarily by O_2 to form vinoxy CH_2CHO ($C_2H_3 + O_2 \longrightarrow CH_2CHO + O$) and formaldehyde and HCO ($C_2H_3 + O_2 \longrightarrow CH_2O + HCO$). The former reaction is an important source of additional O radicals, while the latter reaction is a second bypass pathway leading to the formation of HCO. Two additional bypass reaction pathways leading to HCO involve the breakdown of CH_2CHO by O_2 , ultimately forming CO and CH_2O through a complex set of reactions, and directly via $CH_2CHO + (M) \longrightarrow CH_2O + CO$.

Because the three bypass pathways described above remain active at high pressure, ethylene ignition is largely unaffected by the loss of H radical to form HO_2 . In particular, at 30 atm, for every mole of ethylene that undergoes hydrogen abstraction, about 0.99 moles of CO are created compared to 0.86 moles at 0.5 atm. This finding is consistent with faster ethylene/air ignitions for ethylene at high pressure (when keeping the energy density per unit mass of the mixture constant) and in contrast with methane. The bypass of the step $CH_2O + H \longrightarrow HCO + H_2$ is key to explaining both the shorter time to ignition for ethylene/air compared to methane/air, as well as the persistent efficiency of PAI of ethylene at elevated pressures.

Chapter 3

Ignition and propagation of streamers in air, and formation of the cathode sheath

Although treated with a zero-dimensional approach in section 2 in order to focus on the kinetic enhancement effects of LTP, plasma-assisted ignition is inherently multi-dimensional. Such plasmas are often generated between two pin electrodes by a voltage pulse. This results in the formation of an ionization wave called a streamer, characterized by a strong electric field at its head, which promotes ionization and allows for continued propagation. During each NSD, the curvature of the electrode tips results in strong local electric fields, leading to the ignition of streamers at both the anode and cathode. These streamers propagate towards the center of the gap, eventually connecting and forming a channel of charged and active particles.

Even in the absence of ignition and combustion, the simulation of streamers represents a significant challenge due to restrictive time step size constraints, and stringent resolution requirements associated with resolving structures that arise during the streamer's evolution. One such structure is the cathode sheath, which forms near the cathode surface as electrons are driven away from the region, and space charge effects generate elevated electric fields $\mathcal{O}(1000 \text{ Td})$ and steep gradients in the fields. The remainder of this chapter is dedicated to examining the multi-dimensional

nature of plasma streamers through its evolution, and understanding the associated numerical challenges.

3.1 Models and Methods

3.1.1Governing equations and computational domain

Streamer propagation across a pin-to-pin gap in atmospheric air is simulated using a plasma fluid model, consisting of transport equations for density, momentum, energy density, and species mass fractions,

$$\frac{\partial \rho}{\partial t} = -\nabla \cdot (\rho \mathbf{u}) \tag{3.1}$$

$$\frac{\partial \rho}{\partial t} = -\nabla \cdot (\rho \boldsymbol{u}) \tag{3.1}$$

$$\frac{\partial \rho \boldsymbol{u}}{\partial t} = -\nabla \cdot (\rho \boldsymbol{u} \boldsymbol{u} - p \boldsymbol{I} + \boldsymbol{\Pi}) \tag{3.2}$$

$$\frac{\partial \rho E}{\partial t} = -\nabla \cdot (\rho \boldsymbol{u} E - p \boldsymbol{u}) - \nabla p + \nabla \cdot \boldsymbol{\Omega}$$

$$\frac{\partial \rho E}{\partial t} = -\nabla \cdot (\rho \mathbf{u} E - p \mathbf{u}) - \nabla p + \nabla \cdot \mathbf{Q}$$

$$\frac{\partial \rho Y_k}{\partial t} = -\nabla \cdot (\rho \mathbf{v}_{\text{eff}} Y_k) - \nabla \cdot \mathbf{\mathcal{F}}_k + \rho \dot{\omega}_k, \tag{3.3}$$

which are solved throughout the entirety of each simulation. In the equations above, Π , Ω , and \mathcal{F}_k represent the viscous and diffusive fluxes for momentum, energy density, and mass fraction of species k, with mixture-averaged transport coefficients (viscosity, diffusivity, and thermal conductivity) based on Ern and Giovangigli approximations [42]. In the species transport equation, the effective species velocity $\mathbf{v}_{\text{eff}} = \mathbf{u} + z_k \mathbf{E} \mu_k$ is used in place of the bulk fluid velocity, where z_k is the species charge number, E is the electric field, and μ_k is the mobility of species k. The electric field is obtained by solving the Poisson equation for the electric potential

$$\Delta \phi = -\frac{1}{\varepsilon_0} \rho_c, \tag{3.4}$$

where ϕ is the potential, Δ is the Laplacian operator, ε_0 is the vacuum permittivity, $\rho_c = e \sum_k z_k n_k$ is the charge density, and e is the unit charge.

The electron mobility and diffusivity are determined from BOLSIG+ [50] using cross section data from the Morgan database [112]. Air is modeled as a binary mixture of nitrogen (79% by volume) and oxygen (21%). As shown in figure 3.1, both quantities (normalized by the gas number density N) are functions of the reduced electric field E/N, consistent with a local-field approximation (LFA) [173]. Ion mobilities are held constant at 2.74×10^{-4} m²/V-s [51].

It is known that the LFA suffers from inaccuracies in regions with large gradients in the electric field (for instance within the cathode sheath) [28, 40]. It was shown in [48] that at 100 Pa, large inaccuracies in the electron diffusivity and ionization rate in the cathode sheath region were incurred when using a LFA, while errors in the mobility were more modest. As will be shown in section 2.3, the cathode sheath supports large electric field strengths, which ensure drift effects dominate over diffusive ones, and low electron number densities throughout most of the sheath limit errors related to ionization, other than very close to the sheath boundary. Additionally, agreement between the LFA and higher order models is known to improve at higher pressures due to shorter electron mean free paths and energy dissipation lengths, and LFA has been used in previous studies of discharges at or above atmospheric pressures [16, 145]. It is thus expected that results and trends presented in

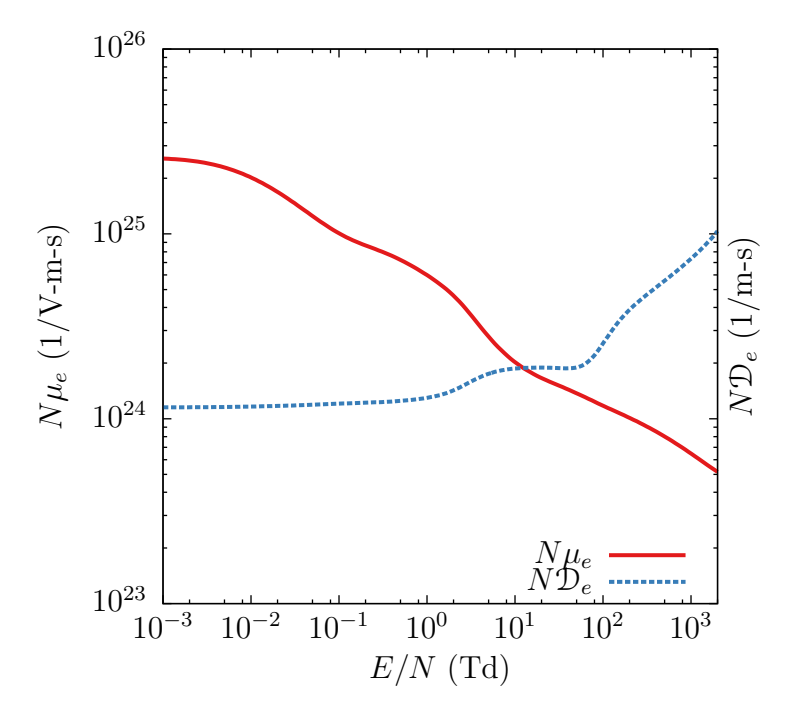


Figure 3.1: Normalized electron transport coefficients in a mixture of N_2 (79% by volume) and O_2 (21%) as a function of the reduced electric field E/N. Data calculated using BOLSIG+ and cross sections from the Morgan database [112].

this study are valid.

Streamer simulations are conducted using the finite-volume compressible reactive flow Navier-Stokes solver PeleC, based on the AMReX library [148]. The computational domain is shown in figure 3.2. All simulations are performed in three dimensions using a quarter of the full domain, exploiting symmetry in the electrode in the x and z directions. The axis of the electrodes is oriented in the y direction, and both the anode (top) and cathode (bottom) protrude from top and bottom planar surfaces by 7.5 mm. The top and bottom surfaces are part of the electrodes while the far-field domain boundaries extend 1 cm in the x and z directions from the axis of symmetry. The choice of domain size has an effect on the solution primarily through the electric potential and electric field, with larger domains generally resulting in slightly steeper gradients in the potential near the pin tips. These effects have been found to be minor for the cases considered, and are thus neglected for the remainder of this dissertation.

As in [159], electrodes are paraboloids in shape and their geometry is determined uniquely by the radius of curvature at the pin tip r_c , and by the gap length ℓ . Following [68], an applied voltage with a sigmoid profile

$$\phi(t) = \phi_{\text{max}} \left[\sigma(t - \delta, \lambda) + \sigma(t - \delta - T_p - T_r, -\lambda) - 1 \right], \tag{3.5}$$

$$\sigma(t,\lambda) = \frac{1}{1 + e^{-\lambda t}},\tag{3.6}$$

drives the anode while the cathode is grounded. For all simulations, the pulse delay time is $\delta = 3$ ns, pulse rise time is $T_r = 5$ ns, the pulse plateau time is $T_p = 12$ ns,

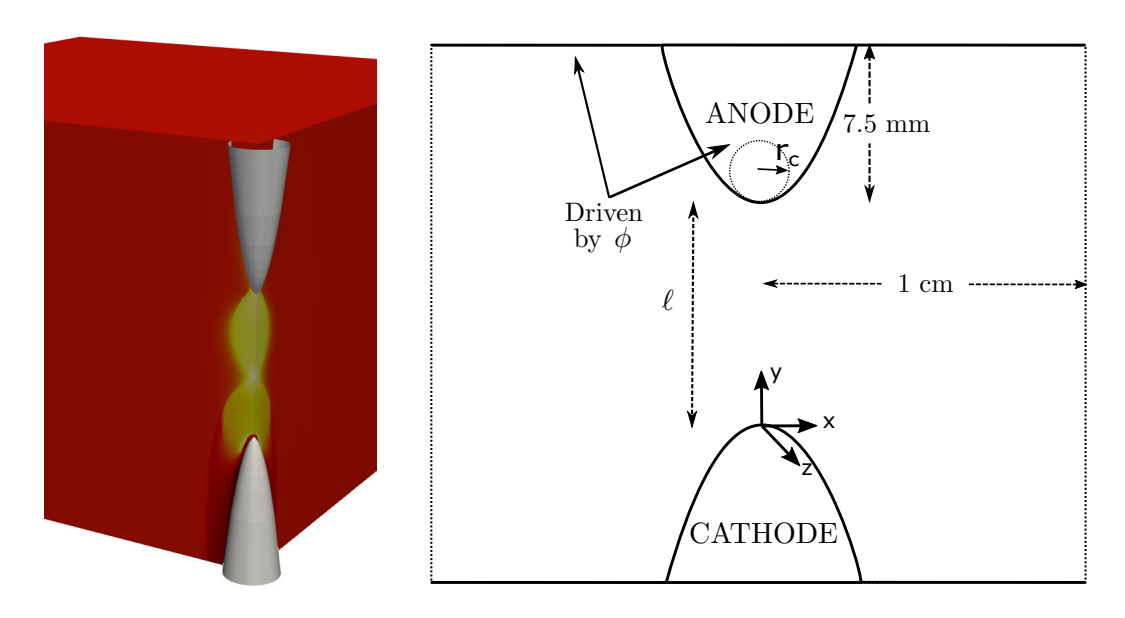


Figure 3.2: Electrode configuration and applied voltage profile. Electrode boundaries are represented with solid lines, while far-field boundaries are shown with dotted lines.

and the scaling factor is $\lambda = 8/T_r$. A range of peak voltages ϕ_{max} and geometries are explored as discussed later in section 3.2.1.

3.1.2 Validity of the plasma fluid model

In section 2.2.1, the assumptions and limitations of the two-term approximation for the electron distribution function were highlighted and discussed, and it was shown that the assumption of a stationary electric field used by BOLSIG+ was valid across the range conditions observed in the simulations in this dissertation. Attention is now given to evaluating other major assumptions that underlie the two-term approximation and plasma fluid model.

As previously stated, BOLSIG+ assumes a spatially homogeneous electric

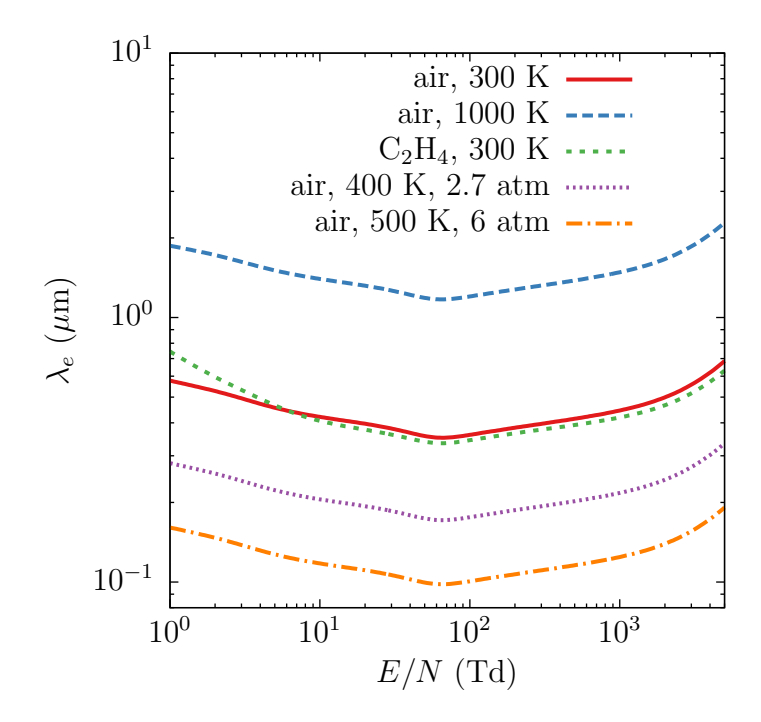


Figure 3.3: Electron mean free path for five gas mixtures as a function of the reduced electric field strength.

field and collision probabilities over length scales comparable with the electron mean free path λ_e , which can be calculated [19] as

$$\lambda_e = \frac{1}{\nu} \sqrt{\frac{2U_e}{m_e}},\tag{3.7}$$

where ν is the electron collision frequency, and U_e is the mean electron energy. BOLSIG+ is used to calculate λ_e for several different mixtures - atmospheric air at 300 K and 1000 K, as well as a stoichiometric ethylene/air mixture at atmospheric conditions and 300 K. Cases in air at elevated temperature and pressure are also considered, with mixtures at 400 K and 2.7 atm, and 500 K and 6 atm. Results are shown in figure 3.3.

For the range of reduced electric field strengths considered, λ_e is $\mathcal{O}(0.1 - 1 \mu \text{m})$. As will be shown later, λ is much smaller than other length scales of interest, for instance the streamer head thickness δ_h $\mathcal{O}(100 \mu \text{m})$, the sheath thickness δ_{sh} $\mathcal{O}(10 - 100 \mu \text{m})$, and the gap length ℓ $\mathcal{O}(1\text{-}10 \text{ mm})$. This separation between λ_e and other relevant length scales provides further justification for use of the two-term approximation for the electron distribution function, and the plasma fluid model.

3.1.3 Photoionization

It is well known that the relaxation of excited neutral species produced during a discharge emit photons that ionize other gas particles. The effects of photoionization processes and seed electrons formed in front of the streamer are of critical importance for a range of physical conditions [72, 117, 55, 56], and modify key properties such as the streamer radius and propagation speed if the background electron number density is sufficiently low. It is common practice in the simulation of streamers in air to assume that the primary contribution to the production of photoions is due to the ionization of O_2 by absorption of photons in the spectral range 98-102.5 nm (typically generated by relaxation of electronically excited N_2). In this case, 102.5 nm is the photoionization threshold of O_2 , and below 98 nm, photons are readily absorbed by N_2 which has a higher ionization energy, and thus provides a negligible contribution to the production of photoions [84].

Photoionization is modeled based on the Zheleznyak approximation [185] for photoionization in atmospheric air:

$$S_{ph}(\mathbf{r}) = \frac{1}{4\pi} \frac{p_q}{p + p_q} \iiint \frac{S_{ion}(\mathbf{r}')}{|\mathbf{R}|^2} \Psi(p|\mathbf{R}|) d^3 \mathbf{r}', \tag{3.8}$$

where it is assumed that photon production is proportional to the rate of ionization S_{ion} . Ψ is the photoionization rate function, a function of the product of p and $|\mathbf{R}|$ (the distance between positions \mathbf{r} and \mathbf{r}'), p_q is the quenching pressure, and position vector \mathbf{r} extends across the entire domain.

While this model describes photoionization accurately, it can be very expensive computationally in large-scale unsteady three-dimensional simulations because its evaluation requires an integral over the entire domain for each grid point, at every time step. Several approaches [137, 11] have been developed in the literature to approximate (3.8). In [90, 21], the Zheleznyak model is approximated as a linear combination of functions,

$$S_{ph} = \sum_{j=1}^{nh} S_{ph}^{j}, \tag{3.9}$$

where each component is the solution to a Helmholtz problem

$$\nabla^2 S_{ph}^j - (\lambda_j p_{O_2})^2 S_{ph}^j = -A_j p_{O_2}^2 S_{ion}^j.$$
 (3.10)

A three-term approximation is used in this work (nh = 3) with three terms providing an accurate approximation over a wide range of conditions. The parameters A_j and λ_j are taken from [21]. The photoionization source term S_{ph} is added to the species production term $\dot{\omega}_k$ for electrons and O_2^+ ions when photoionization is included.

As in [90], homogeneous Dirichlet boundary conditions are used for the solution of the Helmholtz problem, implying that photoionization effects vanish near electrode surfaces, and in the far-field. It was shown in [21] that while such an approach guarantees accuracy in the domain's interior, it leads to an appreciable underestimation of the photoionization source term when there is a source of significant ionization (i.e. at the streamer head) near the boundary. In such cases, more accurate Dirichlet boundary conditions can be formulated by evaluating the full Zheleznyak integral for all boundary cells. For all simulations conducted in the present work, streamers form near the pin tips but quickly propagate towards the center of the gap. It is thus assumed that approximation errors at the domain boundaries are negligible.

3.1.4 Initial and boundary conditions

Boundary conditions for electrons and ions are taken from [47] and follow a "two-stream approximation" [123, 34], which considers both a particle flux directed from the plasma to the wall, and a flux directed from the wall to the plasma. From there, an expression for the electron flux normal to the electrode boundary ($\Gamma_{e,n}$) is given as

$$\Gamma_{e,n} = \frac{n_e}{2}\bar{v} - 2\gamma\Gamma_{i,n}, \quad \bar{v} = \sqrt{\frac{8k_B T_e}{\pi m_e}},\tag{3.11}$$

where \bar{v} is the electron thermal velocity, calculated using the electron temperature and mass $(T_e \text{ and } m_e)$, along with the Boltzmann constant k_B . Thus, electrons are lost to the electrode boundary through the electron thermal velocity term, and are emitted from the electrode through secondary electron emission, dependent on the ion flux to the electrode $\Gamma_{i,n}$, and the secondary electron emission coefficient γ (SEEC). These modeling choices represent a departure from the boundary fluxes traditionally used in similar numerical studies, as an extra factor of two is applied to both terms in equation 3.11. The modeling of boundary conditions for plasma fluid models remains an open question, due in large part to the inherent complexity of trying to describe boundary processes, which require a particle description and the electron distribution function for a high degree of accuracy. Additionally, it will be shown later that in the plasma sheath, which is the region most impacted by modeling choices at the electrode surface, there is only a small degree of sensitivity to the secondary emission coefficient γ , indicating only a modest impact of the additional factor of 2.

Next, the case of a positive ion is considered, assuming the presence of a strong electric field. Under this assumption, electric drift processes are assumed to dominate over thermal motion, and in the presence of a positive electric field component normal to the electrode surface ($E_n > 0$, oriented from the plasma into the electrode), the ion flux becomes

$$\Gamma_{i,n} = n_i V_{d,i},\tag{3.12}$$

where the ion drift velocity normal to the electrode surface is $V_{d,i} = \mu_i E_n$. Conversely, if $E_n < 0$ (the component of the electric field normal to the electrode surface points from the electrode into the plasma), the flux is simply

$$\Gamma_{i,n} = 0. (3.13)$$

An analogous set of conditions can be derived for negative ions, using the same approach described above. As with the electrons, a homogeneous Neumann condition is applied at the far-field domain boundaries. The paraboloid pins are represented using an embedded boundary method with a state redistribution approach [18], which addresses time step restrictions due to small cut cells.

At the onset of the simulations, the gap itself is occupied by quiescent atmospheric air at $T_0 = 300$ K. Following [159], an initial spatially uniform seed charge

density $n_{e,0} = n_{O_4^+,0} = 10^{15} \text{ m}^{-3}$ is prescribed in order to approximate the conditions in the gap after previous pulses [161]. The effect of initial conditions is explored in section 3.2.3. The concentration of all other ions is set to zero. For the electric potential ϕ , the applied voltage ϕ_{app} acts as a Dirichlet condition for the driven electrode (anode), while a homogeneous Dirichlet condition is imposed at the grounded electrode (cathode). Homogeneous Neumann conditions are imposed at the far-field boundary for all quantities.

3.1.5 Kinetics

The air plasma kinetics mechanism from [118] (itself simplified from [70]) is extended to include electron detachment and volumetric ionization of air due to cosmic rays and radiation. The mechanism contains 10 species, and consists of 6 ions $(N_2^+, O_2^+, N_4^+, O_4^+, O_2^+N_2, \text{ and } O_2^-)$, 3 neutral particles $(N_2, O_2, \text{ and } O)$, and electrons. Reactions are summarized in Table 3.1. Following the LFA, the electron temperature T_e is assumed to be a function of the reduced electric field, and parameterized using data from BOLSIG+ [50].

Also considered is the impact of the radioactive decay of gaseous nuclides, specifically radon-222 (222 Rd), which is present in air in trace amounts. Upon decay, 222 Rd emits alpha particles with high energies (4.99 or 5.49 MeV), which ionize neutral species [75]. The emission of these particles is considered isotropic, and is thus treated as a volumetric source of ionization, occurring at the same rate everywhere in the domain. This source term is taken to be $S = 10 \text{ cm}^{-3} \text{ s}^{-1}$ under atmospheric conditions [113], and contributes to the production of electrons, N_2^+ , and O_2^+ .

No.	Reaction equation	k_f (units of cm, s, K, Td)	Ref.						
Electron impact ionization									
1	$e + N_2 \rightarrow e + e + N_2^+$	$10^{(-8.0-400/(E/N))}$	[118, 70]						
2	$e + O_2 \rightarrow e + e + O_2^+$	$10^{(-7.6-600/(E/N))}$	[118, 70]						
Charge transfer									
3	$N_2^+ + N_2 + M \to N_4^+ + M$	5×10^{-29}	[118, 70]						
4	$N_4^+ + O_2 \to O_2^+ + N_2 + N_2$	2.5×10^{-10}	[118, 70]						
5	$N_2^+ + O_2 \to O_2^+ + N_2$	6.0×10^{-11}	[118, 70]						
6	$O_2^+ + N_2 + N_2 \to O_2^+ N_2 + N_2$	9.0×10^{-31}	[118, 70]						
7	$O_2^+ N_2 + N_2 \to O_2^+ + N_2 + N_2$	4.3×10^{-10}	[118, 70]						
8	$O_2^+ N_2 + O_2 \to O_4^+ + N_2$	10^{-9}	[118, 70]						
9	$O_2^+ + O_2 + M \to O_4^+ + M$	2.4×10^{-30}	[118, 70]						
	Electron-ion and ion-ion recombination								
10	$e + O_4^+ \rightarrow O_2 + O_2$	$1.4 \times 10^{-6} \left(300/T_e \right)^{0.5}$	[118, 70]						
11	$e + O_2^+ \rightarrow O + O$	$2.0 \times 10^{-7} \left(300/T_e \right)$	[118, 70]						
12	$O_2^- + O_4^+ \to O_2 + O_2 + O_2$	10^{-7}	[118, 70]						
13	$O_2^- + O_4^+ + M \to O_2 + O_2 + O_2 + M$	2.0×10^{-25}	[118, 70]						
14	$O_2^- + O_2^+ + M \to O_2 + O_2 + M$	2.0×10^{-25}	[118, 70]						
Electron attachment and detachment									
15	$e + O_2 + O_2 \rightarrow O_2^- + O_2$	f(T, E/N)	[70]						
16	$e + O_2 + N_2 \rightarrow O_2^- + N_2$	f(T, E/N)	[70]						
17	$\mathrm{O_2}^- + \mathrm{O_2} \to e + 2\mathrm{O_2}$	f(T, E/N)	[4, 126]						
18	$O_2^- + N_2 \to e + O_2 + N_2$	f(T, E/N)	[4, 126]						

Table 3.1: Summary of reactions and rates used in this study. Rate coefficients that depend on E/N and T_e use units of Td and K. The parameters for the ionization rate coefficients are modified from [118, 70] in order to provide a more accurate fit over a wider range of reduced electric field strengths.

3.1.6 Advancement Algorithm

Algorithm 1 PeleC advancement framework

```
1: procedure Advance
           while t < t_{\text{out}} \text{ do}
 2:
                 \mathbf{E}^n = -\nabla \phi^n
                                                                                     \triangleright Applied voltage \phi_{app} at anode
 3:
                 S_{ph} = S_{ph}(\boldsymbol{U}^n)
                                                               ▷ Calculated using 3-term Helmholtz approx.
 4:
                 S^* = AD(\mathbf{U}^n, \mathbf{E}^n)
                                                                  ▶ Electron and ion boundary fluxes applied
 5:
                 \boldsymbol{U}^* = \boldsymbol{U}^n + \Delta t(S^* + \omega_r)
 6:
                 S^{n+1} = AD(\boldsymbol{U}^*, \mathbf{E}^n)
 7:
                                                                  ▶ Electron and ion boundary fluxes applied
                 U^{**} = \frac{1}{2}(U^n + U^*) + \frac{\Delta t}{2}(S^{n+1} + \omega_r)
 8:
                 F_{AD} = \frac{1}{\Delta t} (\boldsymbol{U}^{**} - \boldsymbol{U}^{n}) - \omega_{r}^{2}
 9:
                 \omega_r = \omega_r(\mathbf{\tilde{U}}^n, F_{AD}, S_{ph})
                                                                                     ▶ Integrated using CVODE [53]
10:
                 \boldsymbol{U}^{n+1} = \boldsymbol{U}^n + \Delta t (F_{AD} + \omega_r)
11:
12:
           end while
13: end procedure
```

A brief summary of the time advancement framework implemented in the PeleC finite volume solver is presented in algorithm 1, which is a modification of the original PeleC time stepping algorithm [1]. Each time step begins with an explicit calculation of the electric field \mathbf{E}^n along with the photoionization source term S_{ph} , as shown in steps 3 and 4. The Poisson equation for the potential and Helmholtz equations S_{ph}^j are solved using the geometric multigrid solver implemented in AMReX, using a second-order centered spatial discretization. Next, a second-order predictor-corrector approach is used to construct a forcing term \mathbf{F}_{AD} (representing the effects of advective, drift, and diffusive processes for all conserved variables \mathbf{U}), through construction of two intermediate "star" states using explicitly-evaluated second-order advective/diffusive source terms \mathbf{S} , and time-lagged reactive sources $\boldsymbol{\omega}_r$. Finally, all conserved variables are integrated cell-by-cell in an implicit manner from time t^n

to t^{n+1} , incorporating reactive processes along with the advective/diffusive forcing, shown in steps 10-12.

The advective fluxes are evaluated by first using characteristic extrapolation to compute the left and right states at the cell face \mathbf{u}^l and \mathbf{u}^r , after which a Riemann solver constructs the fluxes for the conserved variables. Fluxes for the charges species are modified by selecting from \mathbf{u}^l and \mathbf{u}^r based on the effective velocity \mathbf{v}_{eff} . Note that the boundary fluxes discussed in section 3.1.4 are incorporated whenever the advective/diffusive source terms are evaluated, as in steps 5 and 7.

The adaptive mesh refinement (AMR) library AMReX [184] (which is used in PeleC) is used to refine the grid dynamically at locations where large gradients occur using a hierarchy of grid levels. Time advancement across AMR levels proceeds without subcycling, meaning that each AMR level is advanced using the same time step size $\Delta t = t^{n+1} - t^n$, in order to minimize overhead costs. Time advancement with subcycling, in contrast, would advance finer levels with smaller time step sizes, with synchronization between levels performed multiple times throughout the time advancement in a recursive manner. Note that the numerical time step size is discussed in the next section. For each time step, AMR levels are advanced sequentially in order of ascending refinement, to ensure that the solution from coarser levels is available to supply boundary condition data for finer levels at coarse/fine grid boundaries. As successively finer levels are advanced, synchronization between coarser and finer levels is performed, whereby data from a finer level l+1 is projected back onto the coarser level l using a volume-weighted averaging approach, in order to ensure solution consistency in regions where both coarse and fine data exist. At

the interface between coarse and fine meshes, data from the coarse level l provides a boundary condition for the fine level l + 1. Upon successful integration of a fine level l + 1, a refluxing procedure modifies the solution at the coarse/fine interface at level l in order to ensure discrete conservation.

3.1.7 Numerical methods

One of the most crucial considerations for the simulation of streamers is the choice of grid. It is known that discharges display sharp gradients near electrode tips, as well as near the propagating streamer head. In order to resolve such gradients, minimum grid spacings $\Delta_{\min} \sim \mathcal{O}(1 \ \mu\text{m})$ are usually required for atmospheric streamers. While some previous 2D studies [159, 140] were successfully conducted using static grids, this approach is impractical for three-dimensional configurations. In this framework, multiple adaptive mesh levels are utilized, with higher AMR levels corresponding to finer grids. An efficient meshing strategy ensures that the highest AMR levels (which typically account for the majority of the overall number of control volumes) are restricted to regions that require high resolution and that those regions are a small fraction of the entire computational domain.

A base mesh consisting of cells with a grid spacing $\Delta = 156 \ \mu \text{m}$ in each direction is defined on the domain. Additional levels of refinement are added to regions characterized by steep gradients in the reduced electric field by considering the absolute value of the finite difference between adjacent cells,

$$\max(|E/N_{i,j,k} - E/N_{i\pm 1,j\pm 1,k\pm 1}|) \ge 100 \text{ Td.}$$
 (3.14)

In other words, if the absolute difference in reduced electric field between any two

adjacent cells at a given level exceeds 100 Td, those cells are tagged for refinement. Additional levels of refinement are added until either the difference drops below the tagging threshold, or the maximum number of levels specified by the user is reached. In order to resolve the embedded boundary geometry adequately, cells that intersect with the surfaces of the electrodes are also tagged for refinement, up to the highest level. Up to six additional levels of refinement are used ($\ell_{\rm max}=6$), with successive levels using twice the resolution of the previous level, implying a minimum grid spacing $\Delta=2.5~\mu{\rm m}$. The maximum AMR level $\ell_{\rm max}$ is specified to ensure that there is not an unnecessarily high degree of grid refinement, which would increase computational costs significantly. Verification and grid convergence studies have been carried out extensively on AMReX and PeleC [148, 59, 1], and have demonstrated the second-order convergence of the solver across a variety of problems.

The performance of the adaptive mesh is demonstrated in figure 3.4, which shows the reduced electric field near the anode for a typical streamer simulation shortly after ignition. The finest mesh levels are clustered around the head of the streamer, which supports the sharpest gradients, while outer regions with gentler gradients are resolved on coarser meshes. The importance of using an adaptive mesh strategy is highlighted by the fact that a grid resolution of 2.5 μ m across the entire domain would require 120 B cells, roughly three orders of magnitude more than the highest number of control volumes considered in our work.

Due to the explicit handling of transport, time step size constraints driven by the electron drift Courant-Friedrichs-Lewy (CFL) condition and dielectric relaxation time scale (which is associated with the tight coupling between changes in the electron

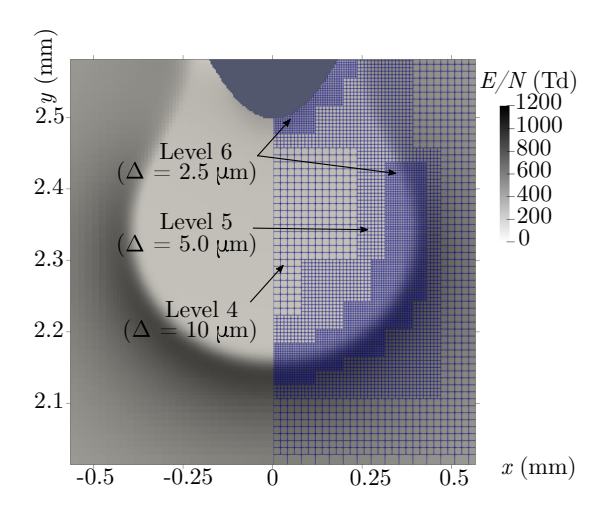


Figure 3.4: Reduced electric field for the reference streamer case (case R). The cells of the finest grid level used to resolve the head of the positive streamer are clustered in regions of high reduced electric field gradient, and near the electrode surface, consistent with the tagging strategy discussed in section 3.1.7.

number density and electric field) must be considered in order to maintain stability of the numerical solution. Following [170], the time step size is calculated as

$$\delta t = \min(0.3 \,\delta t_A, 0.5 \,\delta t_E),\tag{3.15}$$

$$\delta t_A = \min\left(\frac{\Delta}{|\boldsymbol{v}|_{\text{eff.e}}}\right),\tag{3.16}$$

$$\delta t_E = \min\left(\frac{\varepsilon_0}{e\mu_e n_e}\right),\tag{3.17}$$

where δt_A and δt_E represent the electron drift and dielectric relaxation time scale constraints, and minimization occurs across the entire domain and all AMR levels. The factor of 0.3 used for the electron drift constraint differs from values used in previous studies [170, 21], and is a consequence of the method of lines used by PeleC. A maximum time step size of 1 ps is also imposed to ensure solution accuracy.

No.	$r_c \ [\mu \mathrm{m}]$	$\ell \; [\mathrm{mm}]$	$\phi_{\rm max} \ [{\rm kV}]$	γ	$n_{e,0} \ [\mathrm{m}^{-3}]$	S_{ph}	Size [M]
R	50	2.5	15	0.05	10^{15}	No	77.4
C1	50	5.0	15	0.05	10^{15}	No	77.0
C2	300	5.0	15	0.05	10^{15}	No	202.3
V1	50	2.5	10	0.05	10^{15}	No	76.4
V2	50	2.5	20	0.05	10^{15}	No	78.2
I1P	50	2.5	15	0.05	10^{15}	Yes	77.3
I2P	50	2.5	15	0.05	10^{9}	Yes	78.0
B1	50	2.5	15	0.01	10^{15}	No	77.5
B2	50	2.5	15	0.001	10^{15}	No	80.5
В3	50	2.5	15	0	10^{15}	No	83.1
B4	50	2.5	15	$\Gamma_i = n_i V_{d,i}$	10^{15}	No	80.0

Table 3.2: Parameters for pin-to-pin discharge simulations conducted in atmospheric quiescent air. Case R is the reference simulation. Problem sizes correspond to the maximum number of control volumes observed during each simulation, summed across all AMR levels.

3.2 Simulation results

3.2.1 Simulation overview

As in [159], electrodes are modeled as paraboloids with a radius of curvature r_c at the tip equal to 50 or 300 μ m and gap sizes of 2.5 mm for the smaller pin $(r_c = 50 \ \mu\text{m})$, and 5 mm for $r_c = 300 \ \mu\text{m}$. The peak voltage ϕ_{max} varies from 10 to 20 kV. The effect of varying boundary conditions, photoionization, and seed charge are also explored. All simulations are summarized in Table 3.2, and case R is the reference case.

3.2.1.1 Streamer ignition and propagation

The curvature of the pins and the application of voltage at the anode result in elevated electric field strengths near the electrode tips. As the bias voltage increases during the pulse rise, electron avalanches near the electrode tips lead to rapid ionization, and to the formation of a positive streamer (directed towards the cathode, with positive space charge at the head) and negative streamer (directed towards the anode, with negative space charge at the head), as shown in figure 3.5. The two streamers propagate towards the center of the channel and connect in a matter of nanoseconds, forming a channel of increased degree of ionization, as shown in figure 3.6.

Additional insight can be gained from examining one-dimensional profiles of the solution, taken along the axis of symmetry, as depicted in figure 3.7 for t=5 ns. The location of the positive and negative streamer heads (located at approximately y=1.6 mm and y=0.6 mm in 3.7(a), respectively) are identified by the presence of large gradients in number density, and local maxima in the reduced electric field. The plasma in the channels left behind the propagating streamer heads is approximately neutral (the space charge density is one to three orders of magnitude lower than the space charge densities observed at the streamer heads and near the electrode tips), with a plasma density in the positive streamer about an order of magnitude greater than the plasma density in the negative one.

The composition of the plasma behind and ahead of the positive streamer head is shown in greater detail in figure 3.8. There is a peak of positive space charge corresponding to the streamer head, behind which the space charge drops, and then

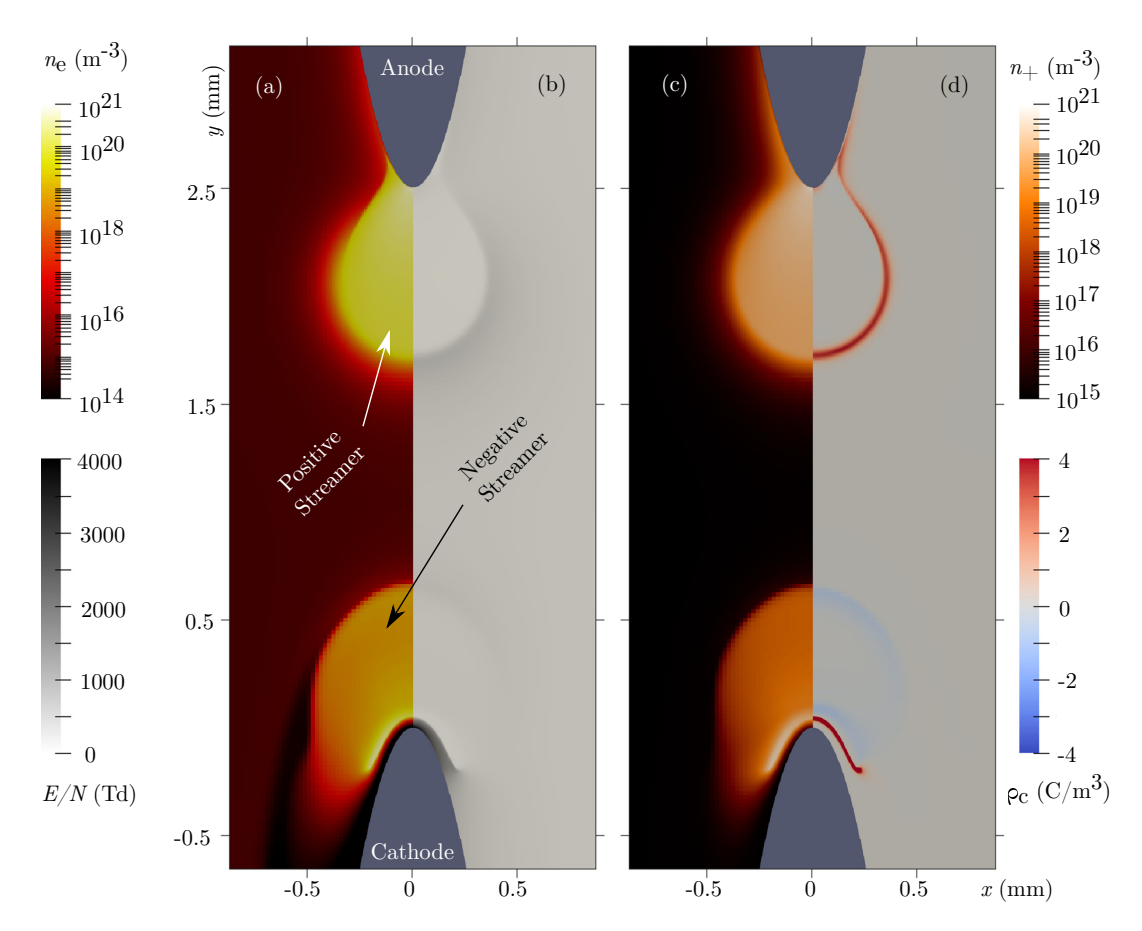


Figure 3.5: (a) Electron number density n_e , (b) reduced electric field E/N, (c) sum of positive ion number densities n_+ , and (d) space charge density ρ_c for case R at 5 ns. A positive streamer emanates from the anode, forming a plasma channel with electrons and positive ions in its wake. A negative streamer with a lower degree of ionization propagates from the cathode. The cathode sheath is apparent as a region void of electrons surrounding the tip of the cathode.

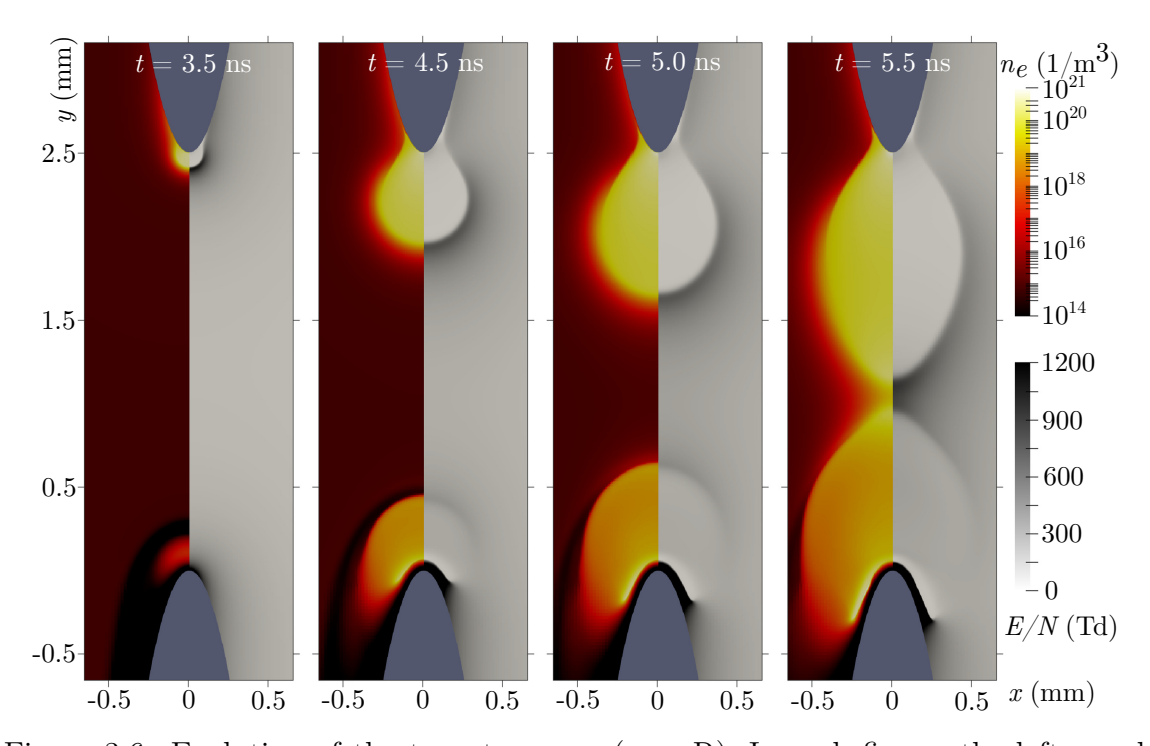


Figure 3.6: Evolution of the two streamers (case R). In each figure, the left panel shows the electron number density n_e and the right panel shows the reduced electric field strength E/N.

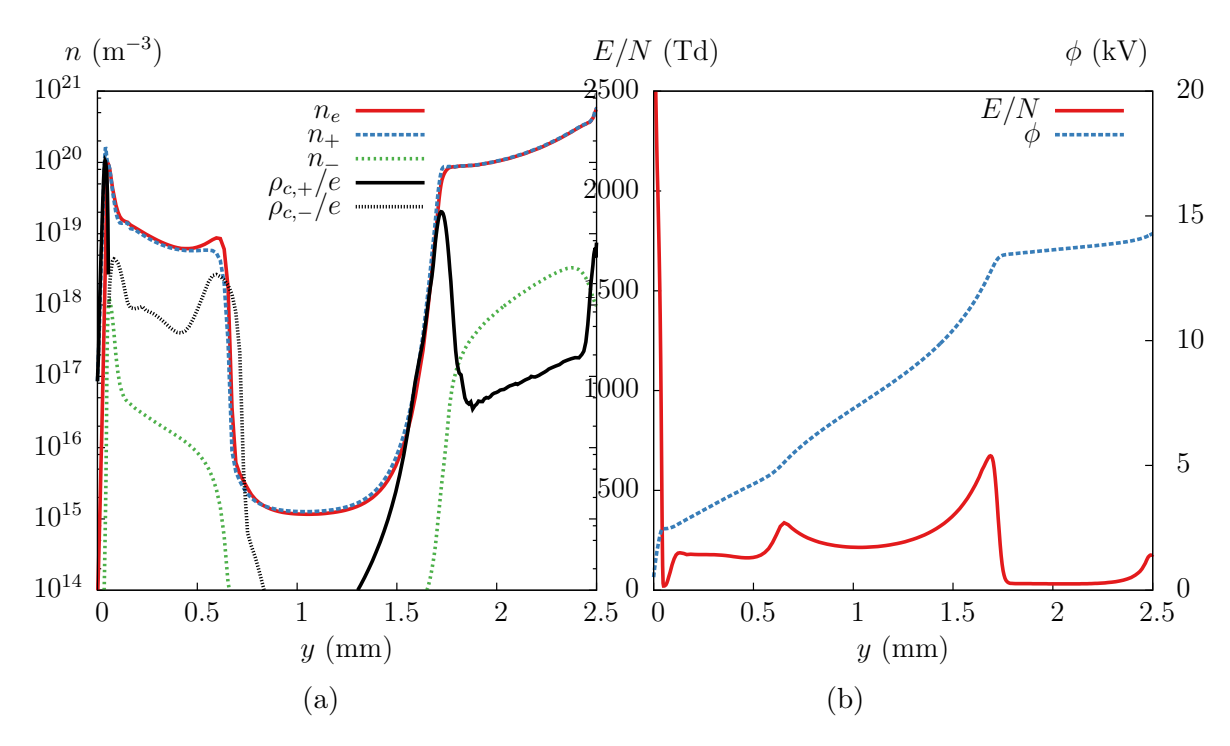


Figure 3.7: (a) Charged species number densities and space charge density components (positive and negative), (b) reduced electric field, and potential along the axis for case R at 5 ns. The axial location with y=0 corresponds to the cathode tip, while y=2.5 corresponds to the anode tip.

steadily rises in the plasma channel towards the anode (right side of figure 3.8), due to the fact that electrons are rapidly lost at the electrode boundary. The number densities of N_2^+ and N_4^+ ions peak near the streamer head, and then decrease in the interior of the channel, as they are converted to O_2^+ and O_4^+ ions (which see number density increases in the same region) through charge transfer reactions. The negative space charge is dominated by electrons, with number densities about 2 order of magnitude greater than that of the negative ions. This is due to the fact that the rate of electron attachment is negligible under the elevated electric fields, and the short time scales associated with streamer ignition and propagation do not leave time for attachment to occur. Ahead of the streamer (left side of figure 3.8), the space charge is dominated by electrons and O_4^+ ions, which is a consequence of the initial conditions. The thickness of the streamer head δ_h can also be estimated as the distance between the two points equal to the peak space charge value $\rho_{c,\text{max}}/10$, and it is found that $\delta_h = 100~\mu\text{m}$ at t = 5~ns.

To characterize the timing of the streamer, the value of the reduced electric field observed at the head of the positive streamer is shown in figure 3.9, alongside its location in the gap, defined as the distance from the anode h_l . The streamer ignition time t_{ig} can then be defined as the time when the maximum value of E/N_{peak} is reached, as the ignition of the streamer coincides with a decrease in the peak reduced electric field due to space charge shielding of the region near the electrode tip. Upon ignition, the positive streamer head propagates rapidly towards the cathode, allowing for the definition of the connection time t_{conn} as the time at which the streamer head reaches its peak propagation speed. These are shown in figure 3.9, indicated with

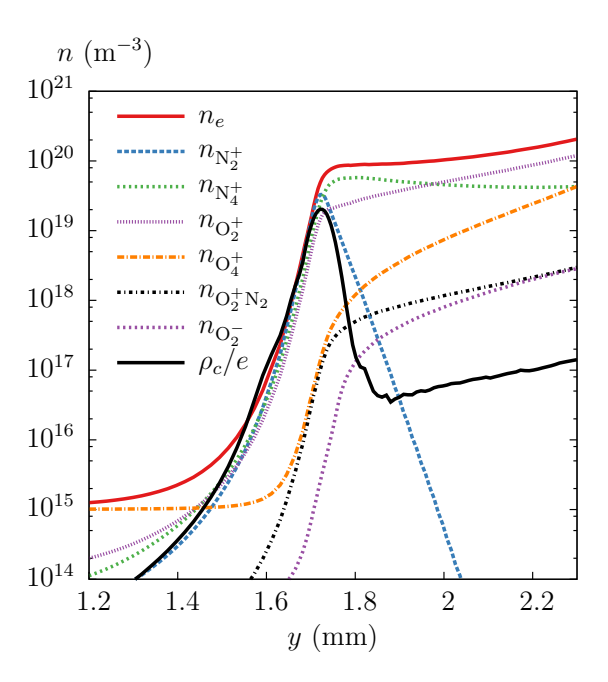


Figure 3.8: Charged species number densities and space charge density at the positive streamer head, taken along the axis for case R at 5 ns.

solid lines.

It is also instructive to consider the evolution of the time step size for case R. As shown in figure 3.10, the electron drift CFL condition is more constraining than the dielectric relaxation one early on, as the peak electron number density in the domain is several orders of magnitude smaller than values during ignition and propagation. As the simulation approaches t_{ig} , electron avalanche processes near the electrode tips lead to a rapid increase in n_e , leading to a sudden drop in the dielectric time scale. For most cases considered in this study, the drift CFL condition is most constraining during most of the propagation phase, driven by the large electric field values in the cathode sheath, as described later in 3.2.1.2. This is due to the fully-explicit time integration approach as discussed in section 3.1.6. For configurations

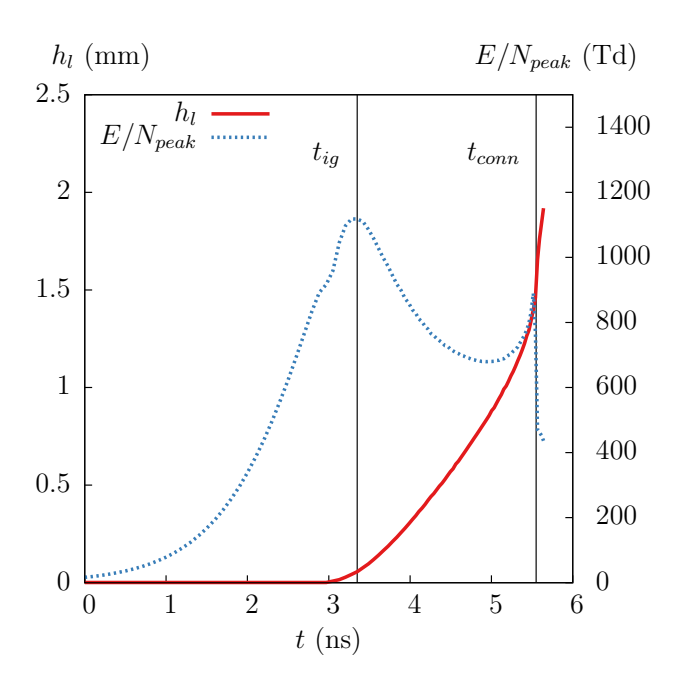


Figure 3.9: Key quantities detailing the evolution of the positive streamer using centerline data from case R. The streamer ignition time t_{ig} corresponds to the maximum value observed in the time evolution of E/N_{peak} . The streamer position is indicated by h_l , defined as the distance of the streamer heat from the anode tip. The connection time t_{conn} is calculated as the time at which the streamer's head moves at its peak speed.

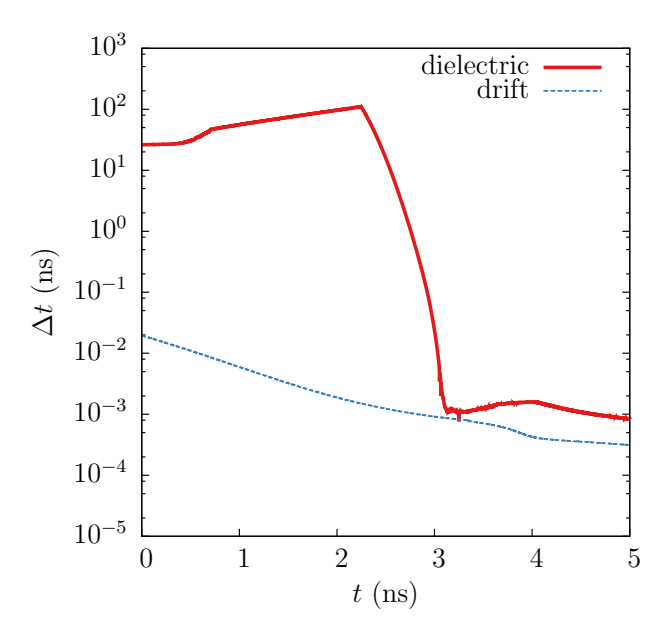


Figure 3.10: Drift and dielectric relaxation time step size restrictions for case R.

when the dielectric relaxation imposes the greatest time step size restriction, the use of a semi-implicit approach to calculating the electric field, as described in [169], may be more appropriate.

3.2.1.2 Sheath formation

Of particular importance is the thin region that develops around the surface of the cathode during the streamer propagation phase. This region has implications for the evolution of the streamer, as the sheath modifies the potential and resulting applied electric field, impacting both local properties, such as currents and energy densities around the cathode, as well as the streamer's propagation speed.

During the pulse rise, a thin region around the cathode surface acts as a capacitor, as electrons drift away from the cathode surface while positive ions drift

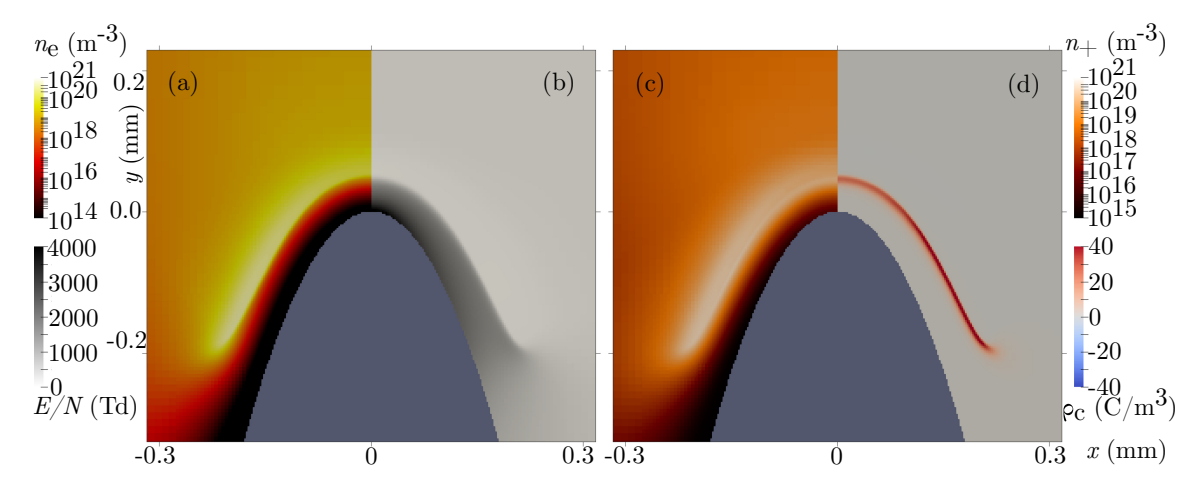


Figure 3.11: (a) Electron number density n_e , (b) reduced electric field E/N, (c) sum of positive ion number densities n_+ , and (d) space charge density ρ_c near the cathode tip for case R at 5 ns.

towards it. The resulting space charge separation leads to a layer of positive ions around the cathode surface with a high electric field as shown in figure 3.11. As positive ions bombard the cathode surface, secondary electrons are emitted, which attain high energies in the high electric field region, leading to further ionization. It is observed that electrons emitted at the electrode surface travel directly to the edge of the sheath region, at which point the electric field curves around the surface of the sheath, as shown in figure 3.12(a).

The vast majority of electrons are generated near the edge of the sheath (away from the cathode surface), where the rate of electron production is the highest, as shown in figure 3.13. As electrons are generated in this region, their number density becomes comparable to that of the positive ions, and space charge shielding effects create a low electric field region where electrons and ions accumulate (corresponding to the sharp drop in the electron production rate), marking the edge of the cathode

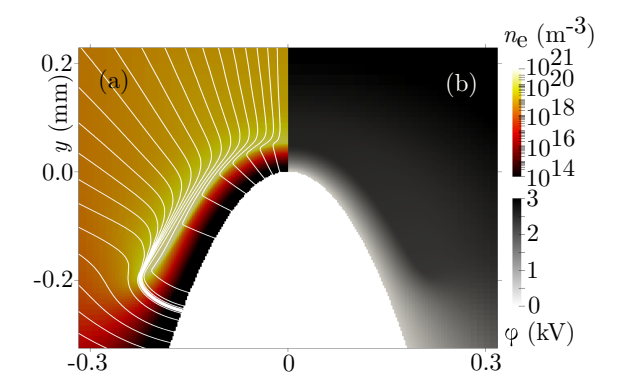


Figure 3.12: (a) Electron number density n_e with electric field lines and (b) potential ϕ for case R at 5 ns.

sheath.

For the streamer simulations conducted, reduced electric field strengths of up to 5000 Td were observed in the cathode sheath region, introducing considerable numerical complexity, as discussed later in section 3.2.2. While the validity of continuum models at such high values of the electric field is questionable, it was observed in [125] that discrepancies of ionization coefficient calculations between a Boltzmann solver and experimental results from [52] remained under 10% until E/N > 3000 Td. Since fields above 3000 Td were only observed in small regions close to the cathode tip, within the sheath where charged particle densities are extremely small, the implications of such errors are judged to be small. Additionally, comparisons between streamer simulations with fluid models and Particle-in-Cell Monte Carlo collision (PIC-MCC) approaches in [33] found that while the overall agreement was rather good (with errors in key metrics such as the propagation speed and peak electric field strengths under 10%), at higher reduced electric field strengths (\geq 1000 Td), relativistic electron runaway [131] can also occur. Such processes cannot be captured

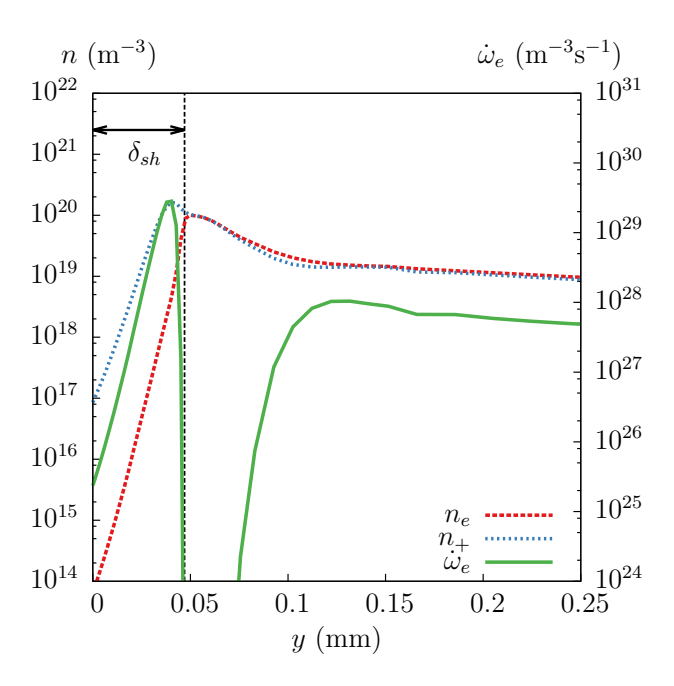


Figure 3.13: Charged particle number densities and electron production rate near the cathode for case R at 5 ns, taken along the axis.

by continuum models, and are neglected in this study as well.

Following [16], a sheath thickness δ_{sh} is defined as the distance between the tip of the cathode and the location along the axis of symmetry where the electron number density reaches half of that of the positive ions. Assuming a grounded cathode, a cathode fall voltage ϕ_{cf} is defined as the voltage at the edge of the cathode sheath, taking on values of about 1-4 kV for the cases considered, as shown in figure 3.12(b). The adaptive mesh in the cathode region is shown in figure 3.14, where it is observed that the finest level of resolution is required across the entire cathode sheath region, due to large gradients in the electric field.

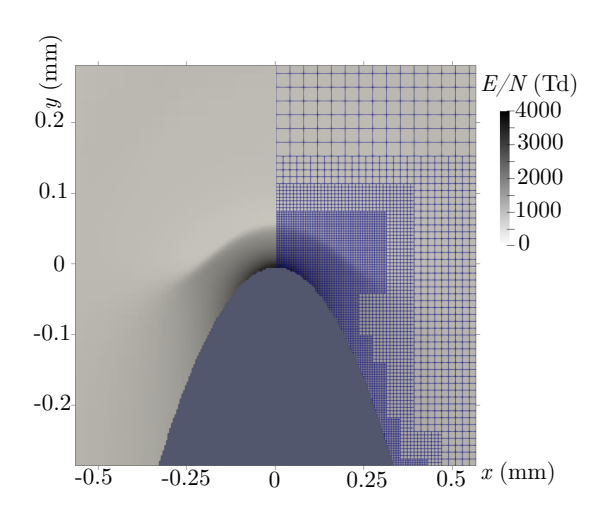


Figure 3.14: Reduced electric field in the cathode region with control volumes for case R at 5 ns.

3.2.2 Impact of electron emissions on formation of the cathode sheath

It is known that the modeling of secondary electron emission impacts the formation and characteristics of the streamer and cathode sheath. The secondary electron emission coefficient γ has been shown to influence the sheath length, with larger values of γ corresponding to thinner sheaths and smaller voltages drops. Comparisons of cathode sheath behavior using different values of γ are shown in figure 3.15. There is considerable departure from typical sheath formation behavior when secondary electron emissions are neglected entirely, as a large area devoid of electrons forms around the cathode, and the cathode streamer does not form.

It is informative to investigate the behavior in the cathode region when different modeling choices are made at the cathode surface. Returning to ideas presented in [47], the number density flux (driven by drift and diffusion) normal to an electrode

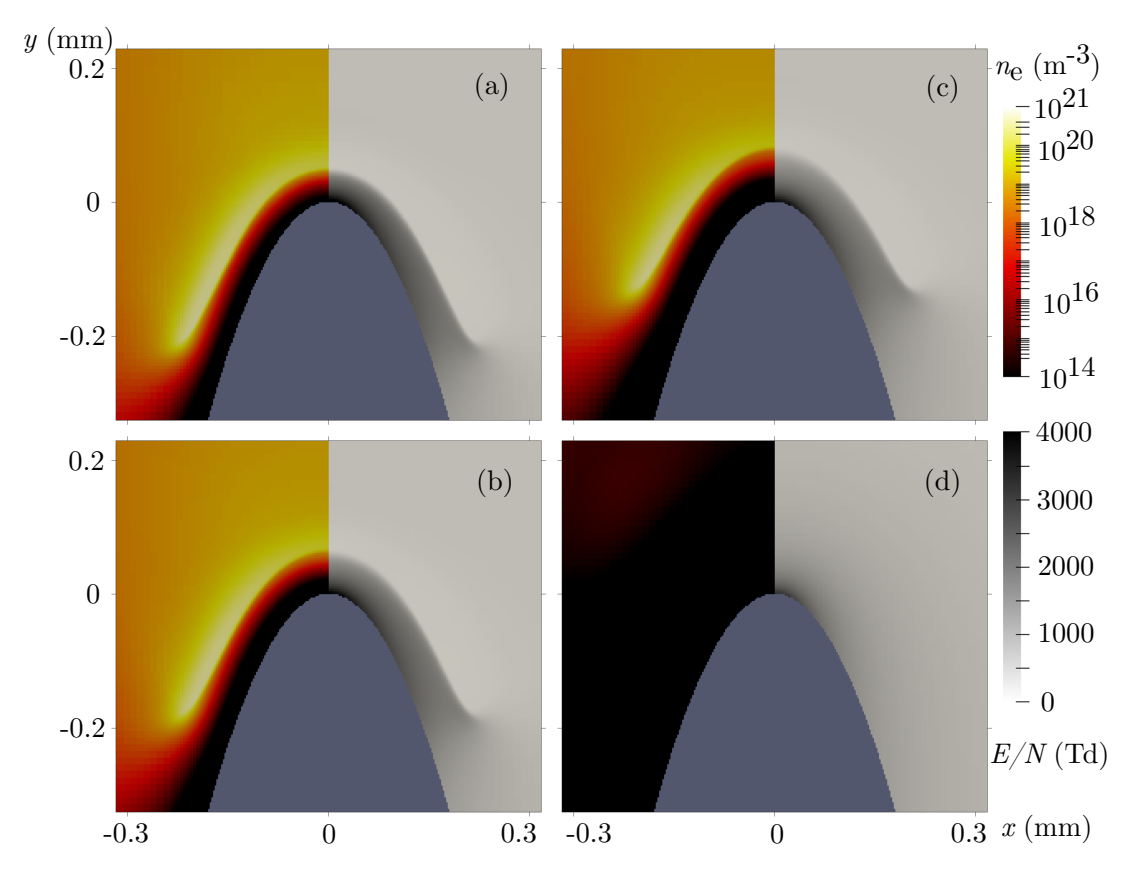


Figure 3.15: Comparison of n_e (left panels) and E/N (right panels) near the cathode region at time t=5 ns, corresponding to cases R, B1, B2, and B3 respectively.

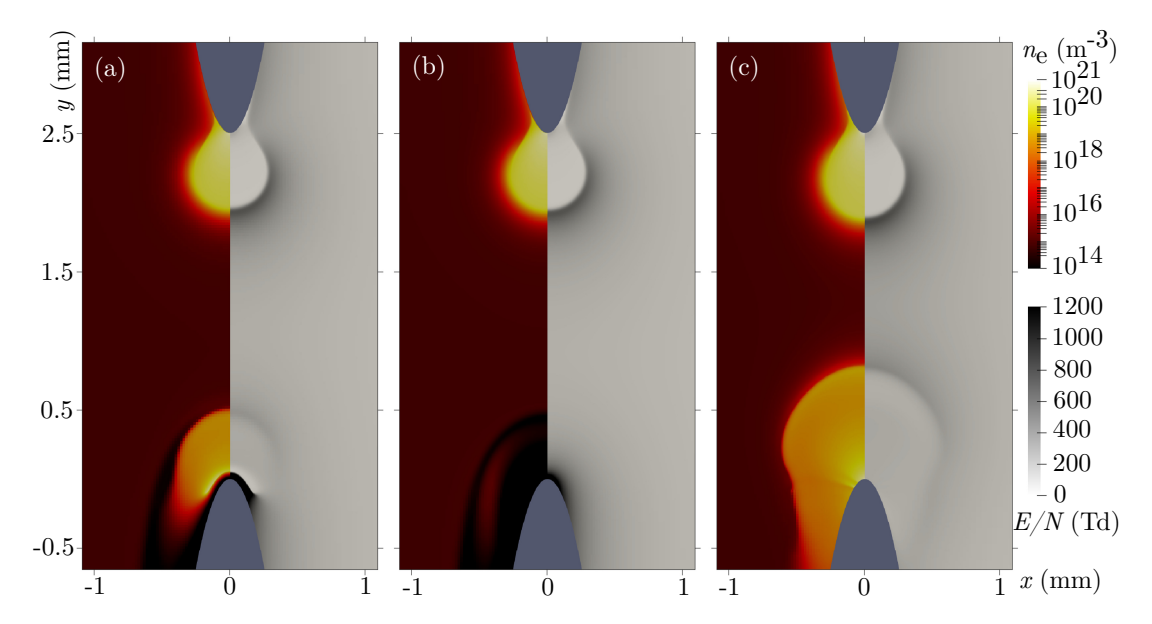


Figure 3.16: Electron number density n_e (left panels) and reduced electric field strength E/N (right panels) at t=4.5 ns for cases (a) R, (b) B3, and (c)B4.

boundary for charged species i can be expressed generally as

$$\Gamma_{i,\eta} = -\mathcal{D}_i \frac{\partial n_i}{\partial \eta} + n_i V_{d,i}, \tag{3.18}$$

where η is the coordinate normal to the boundary. It is apparent then that if the gradient of any charged particle density normal to the electrode surface vanishes, the flux obtained is

$$\Gamma_{i,\eta} = n_i V_{d,i},\tag{3.19}$$

where i now acts as an index over ions and electrons.

Under these conditions, the cathode acts as a source of electrons during the build-up to streamer ignition, with electron emission driven by the electron drift velocity at the electrode surface. It is found that the emission of electrons from the cathode is sufficiently high that a negative streamer forms without the cathode sheath forming. The full range of streamer behavior elicited is depicted in figure 3.16, which compares results using the electrode surface model described in this section (case B4) with results using the boundary conditions from section 3.1.4, using $\gamma = 0.05$ (case R) and $\gamma = 0$ (case B3). The striations around the cathode surface for case B4 are driven by a discrete representation of the paraboloid electrode with the embedded boundary method and its effect on boundary conditions. While modeling choices at the cathode tip have a significant impact on the solution near the cathode, the positive streamer is almost entirely unaffected.

Quantitative differences between cases are shown in figure 3.17(a) and (b). It is apparent that when electron losses at the electrode surface are modeled along with secondary emission of electrons, the behavior of the streamers are similar, with higher values of γ leading to faster streamer propagation, thinner sheath regions, and smaller cathode voltage falls. Elimination of secondary emissions (case B3) leads to a positive streamer that propagates at a similar speed, but the connection time t_{conn} is longer, due to the fact that a negative streamer does not form under such conditions, and the positive streamer must traverse the entire gap. When the cathode sheath is eliminated (case B4), the negative streamer ignites sooner, leading to a faster t_{conn} . While it is clear that the boundary conditions at the electrode can impact the timing of the streamer, it is also observed that until the positive and negative streamers approach each other, the evolution of E/N_{peak} is identical across cases. This has important implications, as the electric field strength at the streamer head determines the rate of ionization and that of production of ions and excited

state neutrals.

Given the clear differences in the evolution of positive and negative streamers, consideration is given to how these differences impact the numerical challenges associated with time integration. The electron drift time step size constraints are presented in figure 3.18. It is observed that the time step size constraints are most severe when the cathode sheath is properly modeled, due to the elevated electric field strengths in this region, which result in large electron drift velocities. When the cathode sheath is eliminated, the drift CFL condition becomes significantly less restrictive, allowing for time step sizes larger than 1 ps during streamer ignition and propagation and leading to greater computational efficiency. Computational efficiency is primarily driven by large stable time step sizes, with a secondary effect due to the fact that large electric fields in the cathode sheath region result in more stringent spatial resolution requirements. A sharp increase in the stable time step size is observed around 4.5 ns for the case where the sheath is eliminated, corresponding to the elimination of the high electric field regions ahead of the positive and negative streamer heads when the two fronts meet. Such an increase is not seen when the sheath region forms because high electric fields values are present.

3.2.3 Impact of initial conditions, photoionization, and problem geometry

In this section the effect of initial conditions, photoionization, and geometry are considered, with a focus on how those impact streamer propagation and the cathode sheath region. One particularly important variable is the initial seed number

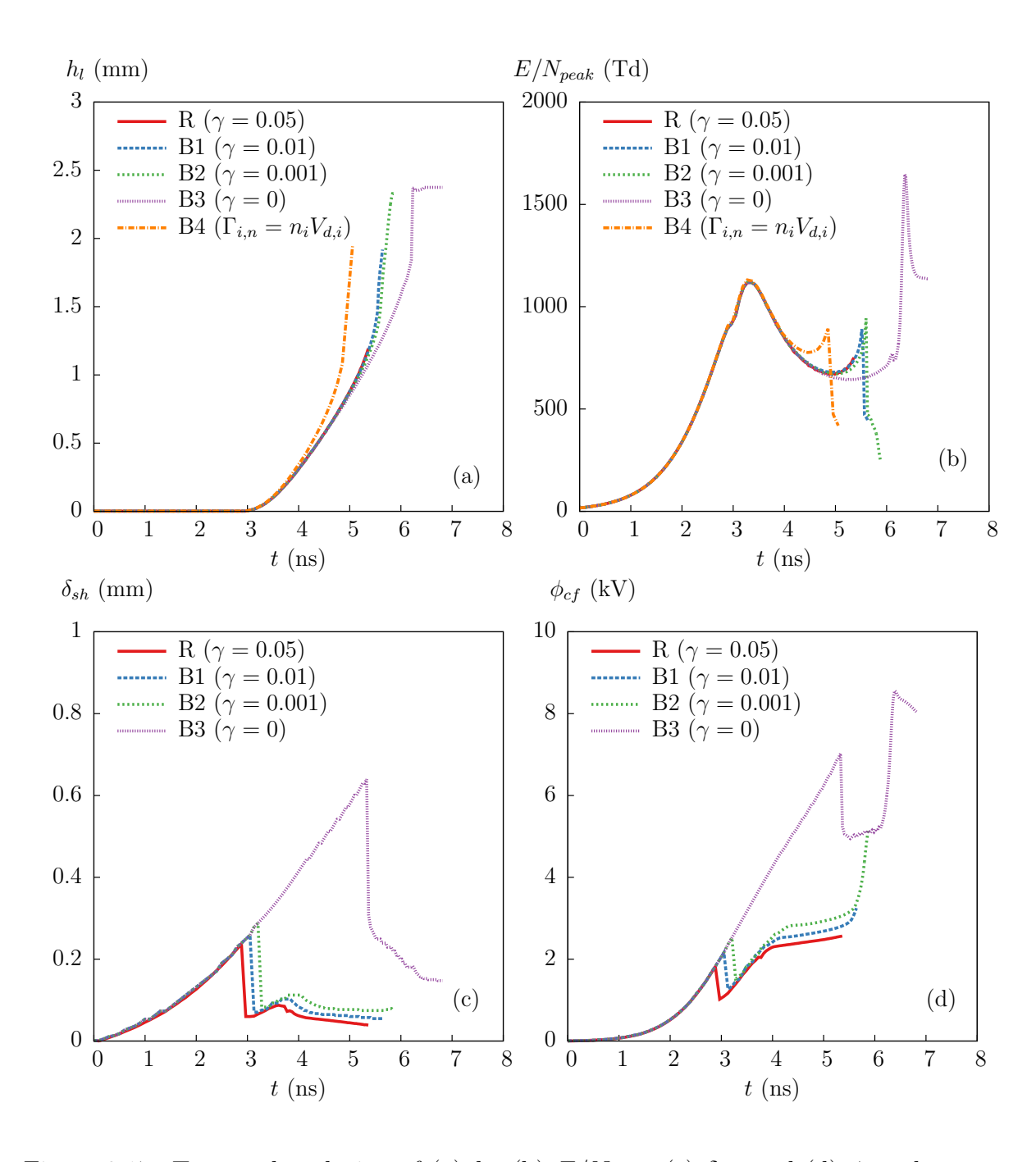


Figure 3.17: Temporal evolution of (a) h_l , (b) E/N_{peak} , (c) δ_{sh} , and (d) ϕ_{cf} , along the axis, for different values of γ and electrode surface models.

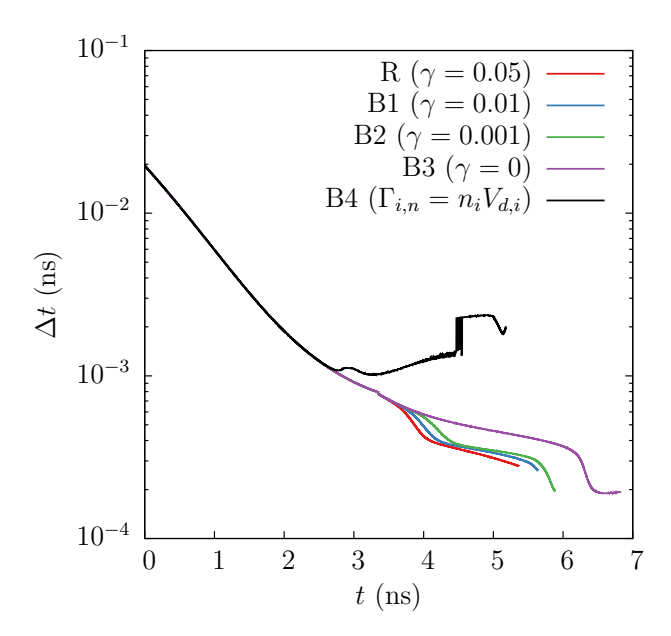


Figure 3.18: Evolution of the time step size constraint based on the electron drift velocity for streamers with γ ranging from 0.05 to 0 and including the "zero-gradient" boundary conditions (case B4).

density of charges, which in the previous sections was held constant at 10^{15} m⁻³. In the context of repeated voltage pulses and discharges, the amount and spatial distribution of electrons and positive ions varies significantly, depending on pulse repetition frequency and voltage, and thermodynamic conditions in the gap, taking values $O(10^3 - 10^{11} \text{ m}^{-3})$ [161]. While 10^9 m^{-3} is often taken as the seed charge value under typical initial conditions prior to any pulses, it was found in [38] that the initial quantity of electrons in the gap may be several orders of magnitude lower due to electron attachment to molecular oxygen in air. However, due to the large electric field values leading to ignition, electrons readily detach from O_2 . It is assumed then that an initial electron seed number density of 10^9 m^{-3} provides a reasonable approximation to gap conditions before pulses, and the effect of the initial concentration of electrons on streamer's dynamics is explored.

One of the primary roles of photoionization is to provide free electrons ahead of the positive streamer head to enable its propagation. As observed in [161], when a high level of preionization is used $(n_{e,0} = 10^{15} \text{ m}^{-3})$, inclusion of photoionization effects results only in a modest increase in the number of electrons ahead of the positive streamer, and thus a slightly faster ignition time and propagation speed. This is seen in figure 3.19(a), where it is also observed that photoionization effects drive a small decrease in the peak electric field during the streamer propagation phase as in figure 3.19(b), due to smaller gradients of charged particle number densities and electric potential around the streamer head. The increase in charges around areas of intense ionization also impacts the cathode sheath region, driving the edge of the sheath closer to the cathode, leading to a smaller cathode fall, as seen in figure

3.19(c) and (d).

When the seed charge number density is low, ignition of the positive streamer is delayed, but the streamer propagates faster. Consistent with previous observations, the lower preionization level ($n_{e,0} = 10^9 \text{ m}^{-3}$) creates much higher gradients in the charged particle number densities, resulting in a noticeably higher peak reduced electric field.

It is interesting to note here that while the initial seed level has a large impact on the behavior of the positive streamer, the effect on the negative streamer is much less pronounced. In all three cases considered, the negative streamer ignites at approximately the same time (corresponding to the sharp drop in the sheath length δ_{sh} and corresponding cathode voltage fall ϕ_{cf}). The evolution of δ_{sh} and ϕ_{cf} is quite similar for the the low and high seed charge cases when considering photoionization, and support a thinner sheath region with a lower cathode voltage fall, as compared with the high seed charge case without photoionization.

Results in figure 3.20(a) and (b) mirror results reported in [159], i.e. increasing the gap length holding pulse parameters constant results in a slower streamer, with a delayed ignition time, and lower peak E/N. Likewise, for a given pin geometry, larger peak applied voltages lead to faster ignition and propagation, as well as higher peak electric fields. Increases to r_c also impact streamer behavior, with larger radii leading to a later ignition, slower streamer propagation, and weaker reduced electric fields across all streamer phases.

Given the data in figure 3.20(c), we conclude that for a given r_c , the evolution

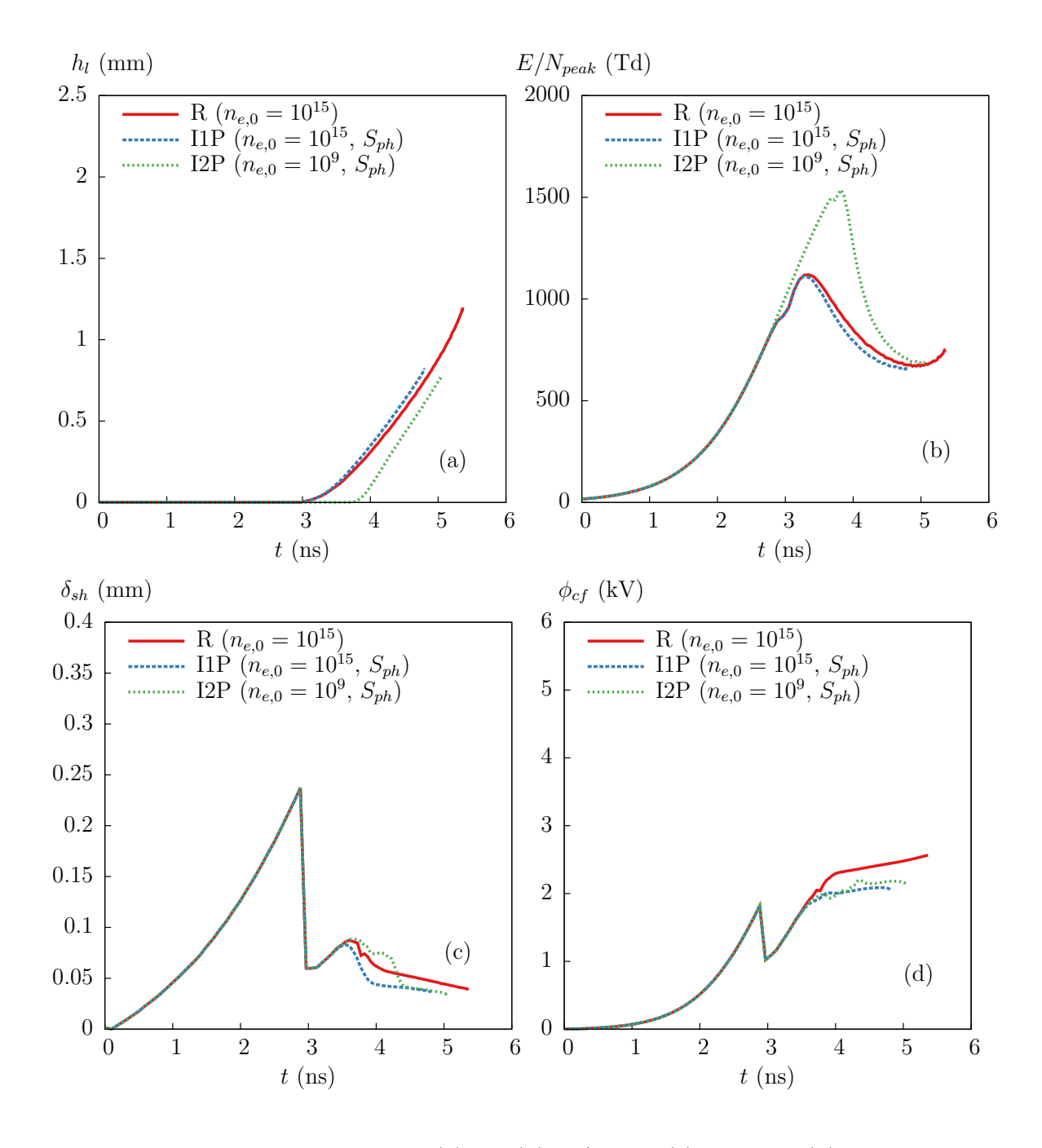


Figure 3.19: Temporal evolution of (a) h_l , (b) $E/N_{\rm peak}$, (c) δ_{sh} , and (d) ϕ_{cf} , taken along the axis of symmetry, for initial seed charge values of 10^{15} and 10^9 m⁻³, with and without photoionization.

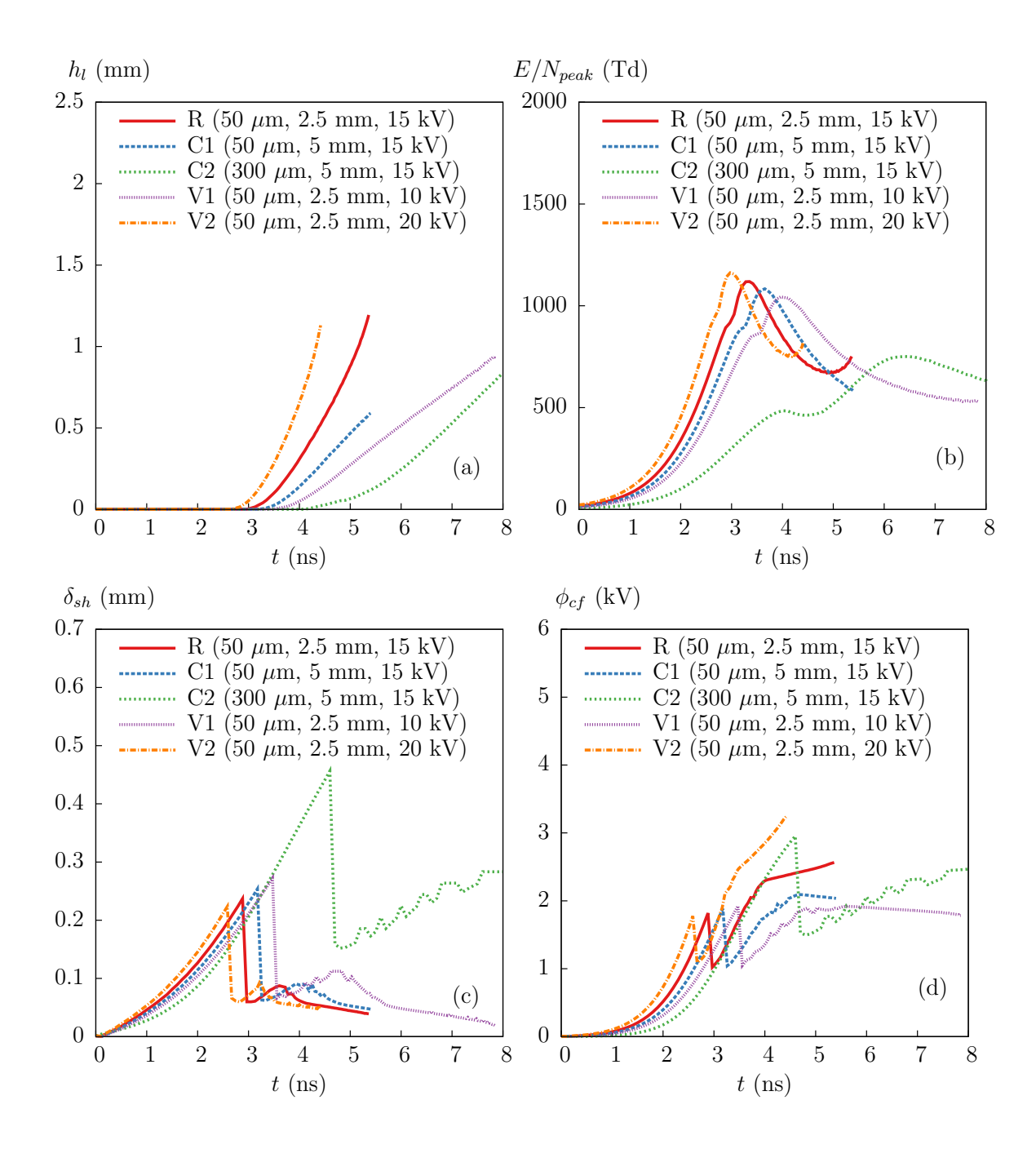


Figure 3.20: Temporal evolution of (a) h_l , (b) $E/N_{\rm peak}$, (c) δ_{sh} , and (d) ϕ_{cf} , taken along the axis of symmetry. Comparisons are made across cases using $r_c = 50$ and 300 μ m, $\ell = 2.5$ and 5 mm, and peak voltages ranging from 10 to 20 kV.

of δ_{sh} is quite similar across cases, with a modest difference in cathode streamer ignition timing seen with changes in ℓ and ϕ_{max} . In addition to a slower ignition and longer propagation phase, increases to r_c result in a thicker cathode sheath (by about a factor of 2 to 3 for the configurations considered). In addition to differences in ignition timing, ϕ_{cf} displays additional dependencies on ℓ and ϕ_{max} , with shorter gaps and larger applied voltages leading to greater cathode voltage falls, as seen in figure 3.20(d).

Chapter 4

Simulations of the plasma-assisted oxidation of ethylene/air mixtures

Conducting successful simulations of the oxidation and ignition of hydrocarbon/air mixtures via NSD requires a comprehensive understanding of multidimensional structures and complex physical process that arise during streamer ignition, propagation, and connection, as well as associated numerical challenges. The application of multiple discharges to ignite a hydrocarbon/air mixture introduces additional complexity, necessitating the development of a chemical kinetics mechanism that captures a wide range of kinetics process (including the excitation, dissociation, and ionization of air and fuel species via electron impact) but also tractable for use in large-scale multidimensional simulations, as well as understanding how important parameters such as pulse characteristics, problem geometry, and mixture conditions promote ignition. Many of these aspects were explored separately in chapter 2 (in a zero-dimensional reactor) and chapter 3, however a comprehensive investigation of the problem necessitates a more unified treatment.

In this chapter, a skeletal mechanism (reduced from the one used in chapter 2) is integrated into the multidimensional plasma discharge solver discussed in the previous chapter. The full evolution of streamer (from the ignition phase through

the spark phase) is simulated, and a complete summary of the discharge is presented. Analysis is then extended to the impact of multiple pulses applied at different frequencies, as well as to changes in the discharge at elevated temperature and pressure.

4.1 Model and numerical methods

4.1.1Governing equations

Simulations of the plasma-assisted ignition of ethylene/air mixtures in a pinto-pin gap are conducted using the reactive Navier-Stokes equations extended to include a drift-diffusion plasma fluid model using two-way coupling (meaning that the plasma fluid model and reactive Navier-Stokes equations are solved simultaneously, and information is communicated between the two models), and Joule heating effects. The temporal evolution of density, momentum, total energy density, and species mass fractions are modeled as

$$\frac{\partial \rho}{\partial t} = -\nabla \cdot (\rho \boldsymbol{u}) \tag{4.1}$$

$$\frac{\partial r}{\partial t} = -\nabla \cdot (\rho \boldsymbol{u} \boldsymbol{u} - p \boldsymbol{\Im} + \boldsymbol{\Pi})$$

$$(4.2)$$

$$\frac{\partial U}{\partial t} = -\nabla \cdot (\boldsymbol{u}U + p\boldsymbol{u}) + \nabla \cdot \boldsymbol{\Omega} + en_e \mu_e \boldsymbol{E} \cdot \boldsymbol{E}
\frac{\partial \rho Y_k}{\partial t} = -\nabla \cdot (\rho(\boldsymbol{u} + z_k \mu_k \boldsymbol{E}) Y_k) - \nabla \cdot \boldsymbol{\mathcal{F}}_k + \rho \dot{\omega}_k$$
(4.3)

$$\frac{\partial \rho Y_k}{\partial t} = -\nabla \cdot (\rho(\boldsymbol{u} + z_k \mu_k \boldsymbol{E}) Y_k) - \nabla \cdot \boldsymbol{\mathcal{F}}_k + \rho \dot{\omega}_k \tag{4.4}$$

$$\Delta \phi = -\frac{1}{\varepsilon_0} \rho_c. \tag{4.5}$$

The equations are identical to those discussed in section 3.1.1, with the addition of the Joule heating term in equation 4.3. The electric field is $\mathbf{E} = -\nabla \phi$, which is obtained through solution of equation 4.5, which relies on the charge density $\rho_c = e \sum_k z_k n_k$, and the vacuum permittivity ε_0 .

Important electron properties, such as the mobility μ_e , diffusivity \mathcal{D}_e , temperature T_e , and various rate coefficients are evaluated as functions of the reduced electric field E/N, assuming a local field approximation (LFA) [173]. These quantities have been parameterized as functions of the reduced electric field using data obtained from BOLSIG+ [50]. The BOLSIG+ calculation for electrons in air (modelled as 21% by volume oxygen and balance nitrogen) was performed using cross section data from the Morgan database obtained from LXCat [112]. Photoionization effects are modeled using the Zheleznyak approximation [185], and solved using a three-term Helmholtz approximation [90, 21]. It was found in [104] that the presence of hydrocarbons (such as methane) shortens the distance of photon propagation due to the large photon absorption cross sections for hydrocarbons, impacting photoionization effects and thus streamer behavior. The impact of such effects on properties such as the streamer ignition time and propagation speed are modest, and are ignored in this work.

The Joule heating term is calculated using the unit charge e, the electron number density and mobility n_e and μ_e , and electric field \mathbf{E} . It is thus assumed that Joule heating is primarily driven by the electric field-induced drift of electrons. This is a reasonable assumption, as the transport of ions is slower by several orders of magnitude, due to their much larger size relative to the electron. The diffusion of electrons is also neglected in evaluating the Joule heating, as the strong electric fields present during a streamer discharge ensure that drift processes dominate over

diffusion. Consistent with the LFA, the electron energy/temperature is a function of the local reduced electric field, and is not modeled separately from the gas energy, as in a local mean energy approximation (LMEA) [121]. It follows that energy gained by the electrons through Joule heating effects during the pulse increases the gas energy density instantaneously, which is an approximation. Our previous study [37] conducted using a LMEA demonstrated that for the conditions considered in this dissertation, pulse energy is first delivered primarily to the electrons. Electrons then transfer energy to the gas through collisions over time scales O(10 ns). As this study is concerned with time scales relevant to ignition and combustion, it is assumed that the error incurred by assuming instantaneous energy deposition is negligible.

A three dimensional domain with electrodes arranged in a pin-to-pin configuration is used for all simulations, conducted using the compressible flow solver PeleC, which uses the adaptive mesh refinement library AMReX [148]. The anode (driven) and cathode (grounded) are located at the top and bottom of the domain, respectively. The pins are modeled as paraboloids, defined by a pin height (fixed at 1.25 mm) and a radius of curvature at the pin tip $r_c = 50 \mu m$, and a gap length $\ell = 2.5 mm$ defined as the distance between the pin tips. Nanosecond pulsed discharges (NSPD) are applied with a frequency f in order to heat and pressurize the electrode gap region. Each nanosecond discharge is simulated using a time-varying sigmoid voltage signal

$$\phi(t) = \phi_{\text{max}} \left[\sigma(t - \delta, \lambda) + \sigma(t - \delta - T_p - T_r, -\lambda) - 1 \right], \tag{4.6}$$

$$\sigma(t,\lambda) = \frac{1}{1 + e^{-\lambda t}}. (4.7)$$

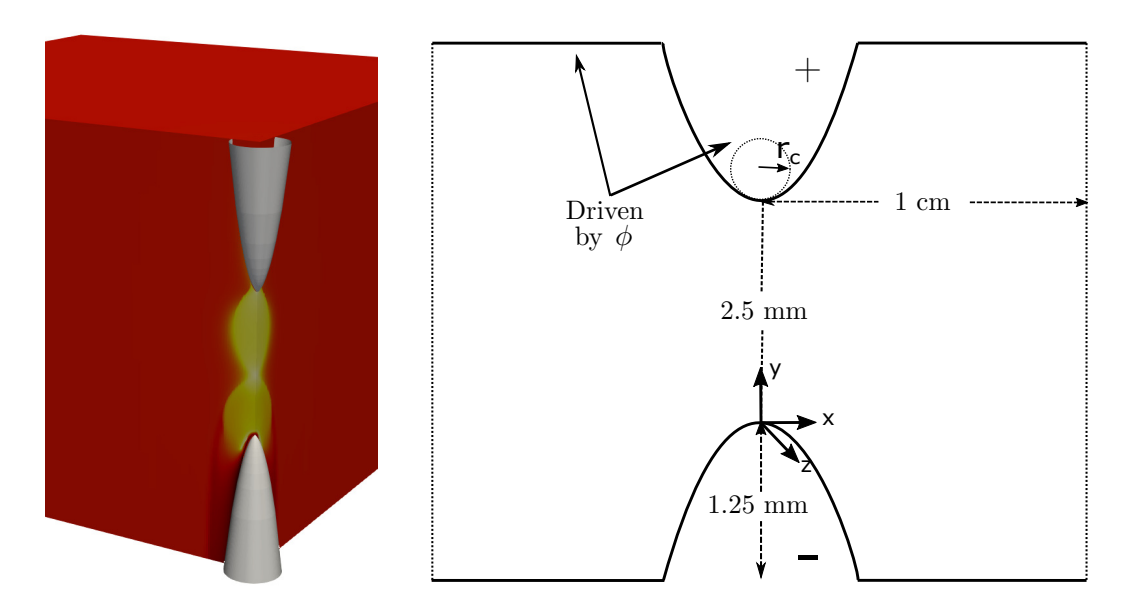


Figure 4.1: Electrode configuration; electrode surfaces are represented with solid lines, while far-field boundaries are shown with dotted lines.

Pulse parameters are held constant for all simulations considered, with pulse delay and pulse rise and fall time $\delta = T_r = 2$ ns, pulse plateau time $T_p = 1$ ns, and scaling factor $\lambda = 8/T_r$.

A schematic of the domain is provided in figure 4.1. In addition to the pins, the top and bottom domain boundaries are treated as electrode surfaces, while the domain boundaries in the span-wise directions are treated as far-field boundaries. Dirichlet conditions are applied for the electric potential at all electrode surfaces, while homogeneous Neumann conditions are applied for charged particles. The pin surfaces are assumed to be adiabatic which is an approximation that is reasonable over shorter periods of time $\mathcal{O}(1 - 100 \text{ ns})$. Gradients normal to the far-field domain boundaries vanish for all quantities of interest.

4.1.2 Reduced ethylene/air kinetics mechanism

The kinetics mechanism used in [37] and reduced in [17] is used, and describes the plasma-assisted oxidation of ethylene. The skeletal mechanism used in this study includes 57 species and 243 reactions. The mechanism includes 5 charged species and 11 excited state species (summarized in table 4.1), and reactions that describe elastic and inelastic collisions between electrons and air/fuel species, resulting in vibrationally and electronically excited species, dissociation, ionization, and electron-ion recombination. The mechanism from [17] has been extended to include negative ions $(O_2^-$ and $O_-^-)$, and reactions describing electron attachment and detachment, as well as ion-ion recombination. All reactions involving electrons and ions are summarized in table 4.2.

Plasma Species				
Vibrational:	$N_2(v1), N_2(v2), N_2(v3), N_2(v4), N_2(v5)$			
Electronic:	$N_2(A^3\Sigma), N_2(B^3\Pi), N_2(C^3\Pi), O_2(a^1\Delta), O_2(b^1\Sigma), O(1D)$			
Charged:	$E, N_2^+, O_2^-, O_2^-, O^-$			

Table 4.1: Plasma species included in the kinetics mechanism.

Rxn. No.	Reaction	Fit type	A (cm, s, K, Td)	β	$\delta \varepsilon \; (\mathrm{eV})$	Ref.				
Vibrational excitation										
R1	$E + N_2 \rightarrow N_2(v_1) + E$	Janev	4.4×10^{-9}	_	0.29	[41]				
R2	$E + N_2 \rightarrow N_2(v_2) + E$	Janev	2.6×10^{-9}	_	0.59	[41]				
R3	$E + N_2 \rightarrow N_2(v_3) + E$	Janev	1.8×10^{-9}	_	0.88	[41]				
R4	$E + N_2 \rightarrow N_2(v_4) + E$	Janev	1.1×10^{-9}	_	1.17	[41]				
R5	$E + N_2 \rightarrow N_2(v_5) + E$	Janev	8.9×10^{-10}	_	1.47	[41]				
	Electronic excitation									
R6	$E + N_2 \rightarrow N_2(A^3\Sigma) + E$	Janev	1.8×10^{-10}	_	6.17	[41]				
R7	$\mathrm{E} + \mathrm{N}_2 \rightarrow \mathrm{N}_2(\mathrm{B}^3\Pi) + \mathrm{E}$	Janev	2.1×10^{-9}	_	7.35	[41]				
R8	$\mathrm{E} + \mathrm{N}_2 \rightarrow \mathrm{N}_2(\mathrm{C}^3\Pi) + \mathrm{E}$	Janev	5.5×10^{-9}	_	11.03	[41]				
R9	$E + O_2 \rightarrow O_2(a^1 \Delta) + E$	Janev	9.6×10^{-10}	_	0.98	[41]				
R10	$\mathrm{E} + \mathrm{O}_2 \to \mathrm{O}_2(\mathrm{b}^1\Sigma) + \mathrm{E}$	Janev	2.3×10^{-10}	_	1.63	[41]				
R11	$E + O \rightarrow O(1D) + E$	Janev	3.4×10^{-9}	_	1.97	[41]				
	Impact	dissociatio	on							
R12	$E + N_2 \rightarrow 2N + E$	Janev	3.4×10^{-8}	_	13.00	[41]				
R13	$E + O_2 \rightarrow 2O + E$	Janev	5.9×10^{-10}	_	4.50	[41]				
R14	$E + O_2 \rightarrow O + O(1D) + E$	Janev	1.8×10^{-9}	_	6.00	[41]				
R15	$E + O_2 \rightarrow 2O(1D) + E$	Janev	3.1×10^{-8}	_	8.40	[41]				
R16	$E + C_2H_4 \rightarrow C_2H_3 + H + E$	Janev	3.7×10^{-9}	_	3.80	[41]				
R17	$E + C_2H_2 \rightarrow C_2H + H + E$	Janev	7.6×10^{-9}	_	1.91	[41]				
R18	$E + H_2 \rightarrow 2H + E$	Janev	3.9×10^{-9}	_	8.90	[41]				
	Io	nization								
R19	$E + N_2 \rightarrow N_2^+ + 2E$	f(E/N)	3.3×10^{-8}	_	15.60	[87]				
R20	$E + O_2 \rightarrow O_2^+ + 2E$	f(E/N)	3.9×10^{-8}	_	12.06	[87]				
		n attachme	nt							
R21	$E + O_2 + M \rightarrow O_2^- + M$	$f(T_e)$	_	_	_	[70]				
R22	$E + O_2 \rightarrow O + O^-$	FIT1	8.1×10^{-12}	_	_	[57]				
R23	$E + O_2(a^1\Delta) \rightarrow O + O^-$	FIT1	8.7×10^{-11}	_	_	[57]				
R24	$E + O_2(b^1\Sigma) \rightarrow O + O^-$	FIT1	2.3×10^{-11}	_	_	[57]				
	Charge transfer and electron detachment									
R25	$\mathrm{O^-} + \mathrm{O_2} \rightarrow \mathrm{O} + \mathrm{O_2}^-$	Janev	1.6×10^{-11}	_	_	[127]				
R26	$\mathrm{O_2}^- + \mathrm{O_2} \rightarrow \mathrm{E} + 2\mathrm{O_2}$	FIT1	4.2×10^{-10}	_	_	[127]				
R27	$\mathrm{O^-} + \mathrm{O_2} \rightarrow \mathrm{E} + \mathrm{O_2} + \mathrm{O}$	FIT1	1.2×10^{-9}	_	_	[127]				
R28	$\mathrm{O^-} + \mathrm{N_2} \rightarrow \mathrm{E} + \mathrm{N_2} + \mathrm{O}$	FIT1	2.2×10^{-12}	_	_	[127]				
Electron-ion and ion-ion recombination										
R29	$E + N_2^+ \rightarrow 2N$	Arr.	4.9×10^{-5}	-0.5	_	[41]				
R30	$E + O_2^{-+} \rightarrow 2O$	Arr.	6.0×10^{-4}	-1.0	_	[41]				
R31	${\rm O_2}^- + {\rm O_2}^+ + {\rm M} \to 2{\rm O_2} + {\rm M}$	Arr.	3.1×10^{-19}	-2.5	_	[70]				
R32	$O^- + O_2^+ + M \to O + O_2 + M$	Arr.	3.1×10^{-19}	-2.5	_	[70]				
R33	$O_2^- + N_2^+ + M \to O_2 + N_2 + M$	Arr.	3.1×10^{-19}	-2.5	_	[70]				
R34	$O^- + N_2^+ + M \to O + N_2 + M$	Arr.	3.1×10^{-19}	-2.5	_	[70]				

Table 4.2: Summary of reactions involving electrons and ions.

The mechanism also describes quenching of vibrationally and electronically excited species, which are associated with fast [144] and slow [74] heating processes, respectively. These plasma processes are coupled with the combustion mechanism from [69], which describes the oxidation of various hydrocarbon fuels, and has been validated for both lean and rich stoichiometries, and pressures up to 40 atm.

4.1.3 Numerical methods

The original advancement algorithm used by PeleC is first summarized, with further details available in [1]. Next, extensions to the algorithm to accommodate the LFA fluid model are discussed. The reactive Navier-Stokes equations are integrated in PeleC using a finite-volume second-order method-of-lines (MOL) approach. Advection of the conserved variables (\boldsymbol{U}) is discretized using a Godunov scheme with characteristic extrapolation to the cell faces, and a Riemann solver [97]. Diffusive sources are discretized using a second-order centered approach, and transport coefficients based on Ern and Giovangigli approximations [42].

A predictor-corrector approach is employed, whereby the advective and diffusive sources S_{AD} are calculated multiple times in order to construct an approximation to the state variable U^{**}

$$S_{AD}^{n} = A(U^{n}) + D(U^{n})$$

$$(4.8)$$

$$U^* = U^n + \Delta t (S_{AD}^n + \omega_r) \tag{4.9}$$

$$S_{AD}^{n+1} = A(U^*) + D(U^*)$$
(4.10)

$$U^{**} = \frac{1}{2}(U^n + U^*) + \frac{\Delta t}{2}(S_{AD}^{n+1} + \omega_r), \tag{4.11}$$

where A and D represent the advective and diffusive operators, while ω_r is a timelagged reactive source. From here, an advective/diffusive forcing term is calculated

$$\mathbf{F}_{AD} = \frac{1}{\Delta t} (\mathbf{U}^{**} - \mathbf{u}^n) - \boldsymbol{\omega}_r, \tag{4.12}$$

after which the solution at the next time step is obtained by integrating U^n with \mathbf{F}_{AD} and the reactive sources until time n+1 using CVODE [53]. The time-lagged reactive source term is then updated for the next time step

$$\boldsymbol{\omega}_r = \frac{\boldsymbol{U}^{n+1} - \boldsymbol{U}^n}{\Delta t} - \boldsymbol{F}_{AD}. \tag{4.13}$$

4.1.3.1 Plasma fluid model

In this section, the time advancement outlined in section 4.1.3 is extended and modified to incorporate the plasma fluid models. Each time step begins with the calculation of the electric field. In this study, we adopt a semi-implicit approach [169], whereby a first-order explicit prediction of the space-charge is used to approximate the potential at time n + 1

$$\Delta \phi^{n+1} = -\frac{e}{\varepsilon_0} \sum_{k} z_k \left(n_k^n + \Delta t \nabla \cdot \left(-n_k^n \mu_k^n \nabla \phi^{n+1} - \mathcal{D}_k^n \nabla n_k^n \right) \right). \tag{4.14}$$

Such approaches have been found to reduce the restrictiveness of the dielectric relaxation timescale by one to two orders of magnitude. Next, the Helmholtz equations used to approximate photoionization effects [21] are solved to calculate the photoionization source term S_{ph}^n . The electric field is then used to evaluate the advective source term for charged species and the mean electron energy, and is also used to evaluate electron transport coefficients. Each time S_{AD} is evaluated, the Joule heating source term S_{jh} is calculated and applied to the gas energy.

It was observed in preliminary simulations that that during each nanosecond pulse, the electron advective CFL condition (driven by a large electron drift velocity) was responsible for the most severe time step size restriction. In between pulses, however, the electron diffusion CFL condition was found to restrict the time step, and resulted in prohibitively small time steps and overall computational costs. In order to address this problem, an implicit approach for evaluating the diffusive source term for electrons $D()_{Y_E}$ was adopted

$$D_{Y_E}(Y_E^{\text{old}}) = \nabla \cdot (\mathcal{D}_e \nabla) Y_E^{\text{new}} = \frac{Y_E^{\text{new}} - Y_E^{\text{old}}}{\Delta t}, \tag{4.15}$$

where $Y_E^{\text{old}} = Y_E^n$ and $Y_E^{\text{new}} = Y_E^*$ when equation 4.8 is evaluated, and $Y_E^{\text{old}} = Y_E^*$ and $Y_E^{\text{new}} = Y_E^{**}$ when equation 4.10 is evaluated. As before, a second-ordered centered discretization is used, and implicit sources are evaluated whenever \mathbf{S}_{AD} is needed. The updated time advancement approach is summarized in algorithm 2.

4.1.3.2 Grid resolution and time step size

To resolve sharp gradients in the solution (for instance in the streamer head, and near the electrode tips), grid spacing $\mathcal{O}(1 \ \mu\text{m})$ is required. As these regions are typically limited to a very small percentage of the overall domain, the adaptive mesh refinement (AMR) library AMReX [148] is used to increase the grid resolution in these regions only. A base coarse mesh consisting of cells with a grid spacing

Algorithm 2 PeleC advancement framework

```
1: procedure ADVANCE(U(\rho, \rho u, U, n_k))
           while t < t_{\text{out}} \text{ do}
 2:
                \mathbf{E}^{n+1} = -\nabla \phi^{n+1} > Applied voltage \phi_{app} at anode, semi-implicit approx.
 3:
                S_{ph} = S_{ph}(\mathbf{U}^n)
                                                          ▷ Calculated using 3-term Helmholtz approx.
 4:
                S^* = AD(U^n, E^{n+1}) > Advective/diffusive sources and boundary fluxes
 5:
                                                        \triangleright Implicit evaluation of the Y_E diffusive source
                   D_{Y_E} = D(Y_E^n)
 6:
                   S_U^* + = S_{ih}(\boldsymbol{U}^n, \boldsymbol{E}^{n+1})
 7:
                                                                         oldsymbol{U}^* = oldsymbol{U}^n + \Delta t (oldsymbol{S}^* + oldsymbol{\omega}_r)
 8:
                S^{n+1} = AD(U^*, E^{n+1})
 9:
                   D_{Y_E} = D(Y_E^*)
10:
                   S_U^{n+1} + = S_{jh}(\boldsymbol{U}^*, \boldsymbol{E}^{n+1})
11:
                oldsymbol{U}^{**}=rac{1}{2}(oldsymbol{U}^n+oldsymbol{U}^*)+rac{\Delta t}{2}(oldsymbol{S}^{n+1}+oldsymbol{\omega}_r)
12:
                F_{AD} = \frac{1}{\Delta t} (U^{**} - U^n) - \omega_r

    Advective/diffusive forcing term

13:
                \boldsymbol{\omega}_r = \boldsymbol{\omega}_r(\boldsymbol{U}^n, \boldsymbol{F}_{AD}, S_{ph})
                                                                                      ▶ Integrated using CVODE
14:
                U^{n+1} = U^n + \Delta t (F_{AD} + \omega_r)
15:
          end while
16:
17: end procedure
```

 $\Delta=156~\mu\mathrm{m}$ in each direction is defined on the entire domain. A hierarchy of successively finer grids are used to resolve steep gradients in the solution, with up to 7 additional levels of refinement (with a refinement factor 2) utilized (resulting in $\Delta_{\min}=1.25~\mu\mathrm{m}$).

Refinement criteria are defined based on the gradients in the reduced electric field E/N, temperature T, and pressure p. As described in equation 3.14, cells are tagged for refinement at a given level when the absolute value of the finite difference between adjacent cells exceeds a user-specified threshold. For the atmospheric cases discussed in the remainder of this chapter, the thresholds are $\Delta E/N = 50 \text{ Td}$, $\Delta T = 100 \text{ K}$, and $\Delta p = 0.05 \text{ atm}$. These parameters ensure sufficient resolution of the propagating streamer head and resulting plasma channel, as well as the heated and

pressured hot spots that form near the electrode tips, and the subsequent shock waves. The pin surfaces are represented using an embedded boundary (EB) approach [58], with a state redistribution scheme [18] used to resolve the small cut cell problem. In order to ensure the EB geometry is resolved adequately, cells that intersect with the surfaces of the electrodes are also tagged for refinement, up to the highest level.

Due to their small mass, time step size constraints are largely driven by the electron dynamics. Specifically, the electron drift Courant-Friedrichs-Lewy (CFL) condition and dielectric relaxation time scale (which is associated with the coupling between changes in the space charge density and electric field) control the stable time step size δt . Following [170], δt is calculated as

$$\delta t = \min(0.3 \,\delta t_A, 5.0 \,\delta t_E),\tag{4.16}$$

$$\delta t_A = \min\left(\frac{\Delta}{|\boldsymbol{v}|_{\text{eff},e}}\right),\tag{4.17}$$

$$\delta t_E = \min\left(\frac{\varepsilon_0}{e\mu_e n_e}\right),\tag{4.18}$$

where δt_A and δt_E represent the electron drift and dielectric relaxation time scale constraints, and minimization occurs across the entire domain and all AMR levels. The coefficient of 0.3 differs from the original study, driven by requirements of the MOL strategy. The factor of 5.0 is larger by an order of magnitude as well, due to the semi-implicit handling of the Poisson equation for the potential discussed in section 4.1.3.1.

4.2 Ethylene/air results

4.2.1 Voltage sensitivity

A zero-dimensional study is performed first to characterize the sensitivity of the solution to the applied voltage. An isochoric and adiabatic reactor with a time-varying applied electric field strength using the sigmoid profile in equation 4.6 is used to ignite the plasma, and the impact on the evolution of plasma properties is examined. A stoichiometric ethylene/air mixture at atmospheric conditions and an initial temperature of 300 K is considered first, and simulations are conducted over an interval of 100 ns. The evolution of the electron number density for various applied electric field strengths is depicted in Fig. 4.2a, where it is observed that modest changes in the applied electric field strength (\sim 10%) result in important changes in the peak electron number density, which varies by approximately 4 orders of magnitude across cases. This sensitivity extends to the temperature rise ΔT shown in Fig. 4.2b, which varies from negligible heating for the 70 kV/cm case (not shown) to O(1000 K) for the 80 kV/cm case. The gas heating and electron number densities observed across cases range from values typical of corona discharges to spark discharges.

To understand how this sensitivity changes under conditions that reflect combustion applications, additional cases are run with increasing initial temperature and pressure according to isentropic compression laws

$$\left(\frac{p_1}{p_2}\right) = \left(\frac{T_1}{T_2}\right)^{\frac{\gamma}{\gamma-1}},\tag{4.19}$$

with $\gamma = 1.4$. Initial temperatures of $T_0 = 400$, 500, and 600 K are considered. The resulting initial pressures, mass and number densities are provided in table 4.3.

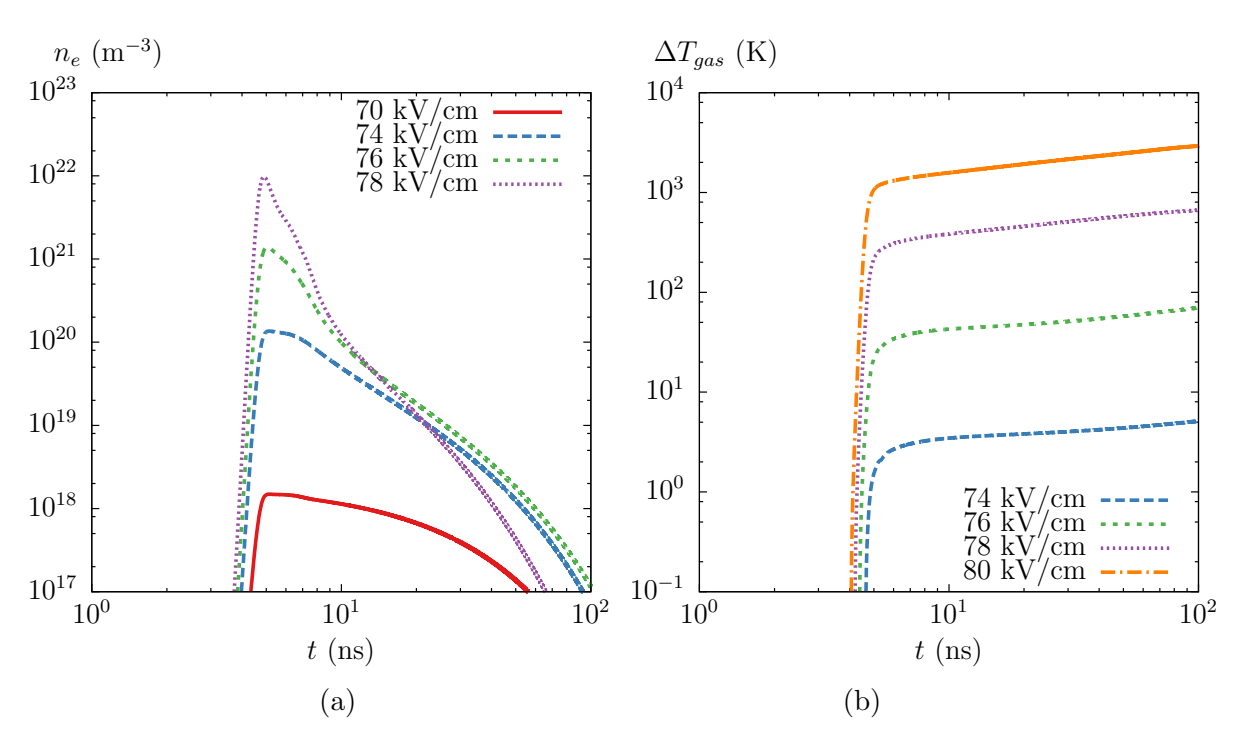


Figure 4.2: Temporal evolution of (a) electron number density and (b) gas temperature for various pulse strengths at atmospheric conditions.

T_0 (K)	$p_0 \text{ (atm)}$	$N~(\mathrm{m}^{-3})$	$\rho~(\rm kg/m^3)$
300	1.0	$\begin{array}{c} 2.446 \times 10^{25} \\ 5.022 \times 10^{25} \\ 8.773 \times 10^{25} \\ 1.384 \times 10^{26} \end{array}$	1.169
400	2.737		2.401
500	5.977		4.194
600	11.314		6.615

Table 4.3: Initial conditions used for increasing temperature and pressure PAC streamer cases assuming isentropic compression and stoichiometric ethylene/air.

Stronger pulses are required to ignite higher pressure mixtures given the increase in the gas number density. Temporal evolution of the electron number density and gas heating for the 600 K case are provided in Fig. 4.3. It is again found that small increases in the pulse strength result in substantial changes in the extent of gas heating, with similar sensitivity in the electron number density observed as well.

The sensitivity of the pulse strength on T_0 and p_0 is illustrated in Fig. 4.4, which shows the change in the gas internal energy density ΔU (at the final time t=100 ns) normalized by the gas number density N, as a function of the reduced electric field. One apparent trend is that as T_0 and p_0 increase, the mixture becomes more sensitive to the pulse strength, as evidenced by the steeper slope for the 11.3 atm case as compared with the atmospheric case. It is also seen that the applied electric field strength corresponding to a given amount of (normalized) deposited energy does not scale linearly with the gas number density, but rather increases at a slower rate. In other words, to obtain the same normalized energy deposition for a case with higher T_0 and p_0 , a lower E/N is required, as compared with a lower pressure/temperature case.

While the reactor simulation results cannot be used to directly select param-

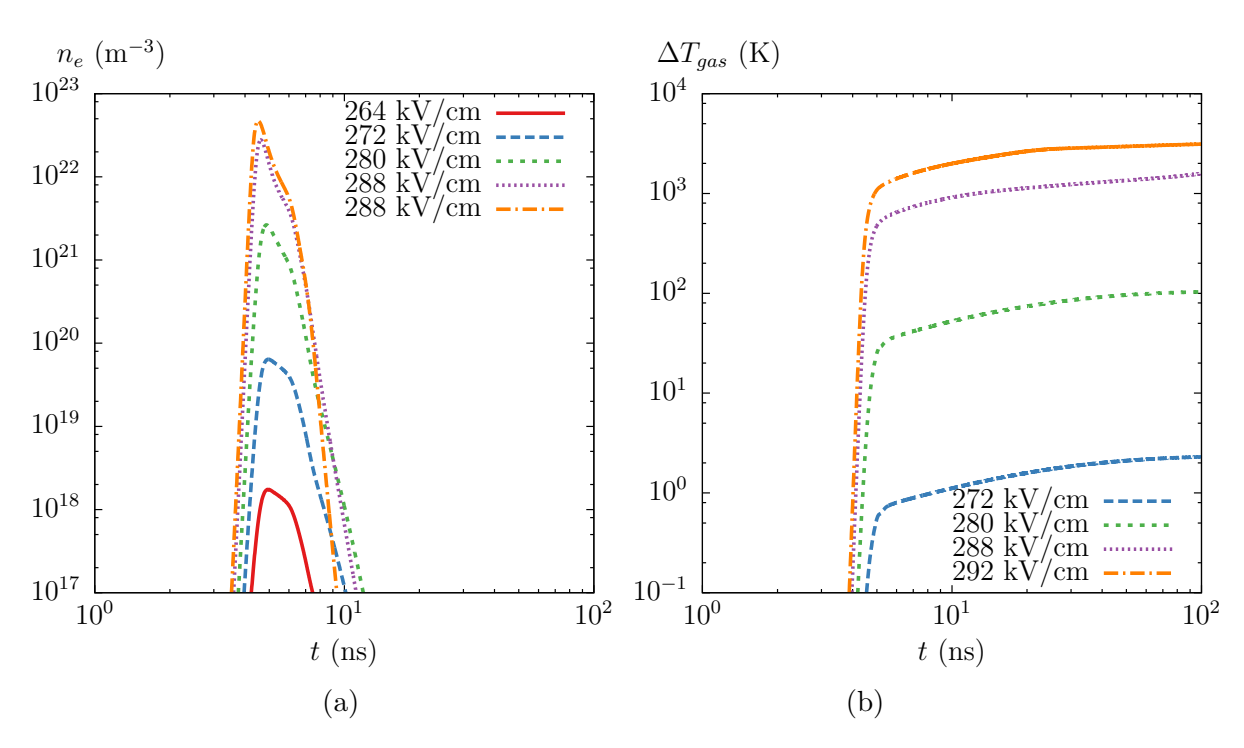


Figure 4.3: Temporal evolution of (a) electron number density and (b) gas temperature for various pulse strengths at $T_0=600~{\rm K}$ and $p_0=11.3~{\rm atm}$.

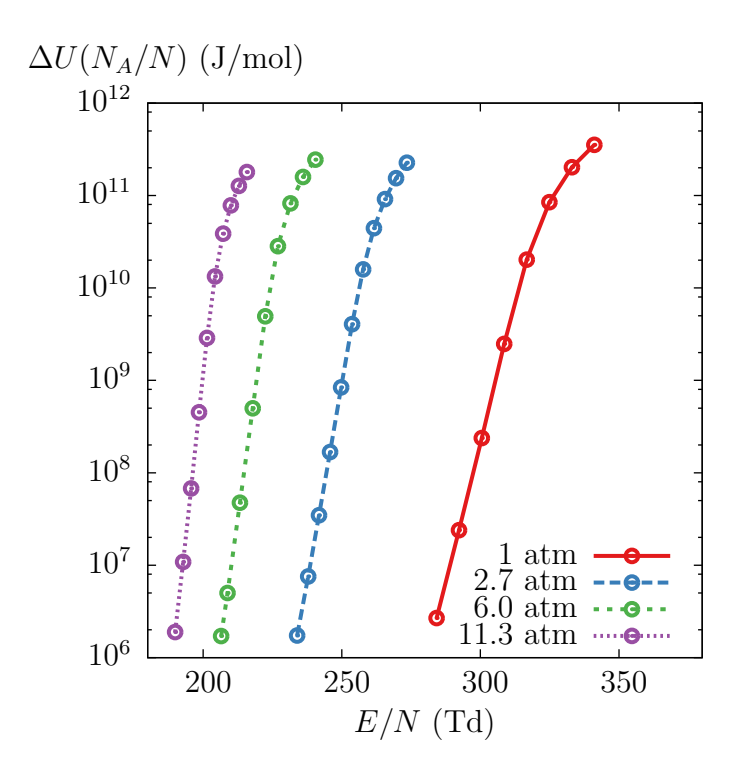


Figure 4.4: Deposited energy per particle as a function of the peak reduced electric field strength for the cases outlined in table 4.3.

eters for multidimensional discharge simulations, the conclusions drawn suggest that in spatially-resolved simulations of plasma discharges, the discharge regime has a sharp dependence on the pulse strength. The results also provide an indication of how the pulse strength might be adjusted as T_0 and p_0 increase.

4.2.2 Single pulse solution

We begin with an overview of the solution during and after a single NSD in section 4.2.2.1. Next, a detailed analysis of the reactions that contribute most to the production and consumption of combustion radicals is presented in section 4.2.2.2. Finally, heating and subsequent acoustic expansion in the plasma channel is

examined, and ignition theory (involving minimum flame kernel radius and ignition energy) is used to assess and quantify the conditions necessary for a successful ignition in section 4.2.2.3.

4.2.2.1 Solution overview

A single pulse is applied to a stoichiometric ethylene/air mixture at atmospheric conditions. The applied voltage was selected to produce a streamer in the glow-to-spark transitional regime, with peak heating of $\mathcal{O}(1000 \text{ K})$. The voltage profile is given in equation 4.6, with $\phi_{\text{max}} = 13 \text{ kV}$. As the applied voltage approaches its peak value, a negative (anode-directed) streamer ignites at the cathode, and a positive (cathode-directed) streamer ignites near the anode at time τ_{ig} (defined as the time at which the peak value of E/N along the axis is observed). The streamers propagate towards the center of the gap and eventually meet at τ_{conn} (defined as the time at which the positive streamer propagates at its peak speed), forming a plasma channel that spans the entire gap. The applied voltage is sustained for a few nanoseconds before dropping during the 2 ns voltage fall phase, which ends by approximately 6 ns.

As the streamer propagates, strong electric fields in front of the head result in the formation of electrons n_e , cations n_+ (O₂⁺ and N₂⁺), anions n_- (O₂⁻, O⁻), vibrationally excited nitrogen $n_{\rm N_2(v)}$ (N₂(v1), N₂(v2), N₂(v3), N₂(v4), N₂(v5)), electronically excited nitrogen $n_{\rm N_2^*}$ (N₂(A³ Σ), N₂(B³ Π), N₂(A³ Σ)), metastable oxygen $n_{\rm O_2^*}$ (O₂(a¹ Δ), O₂(b¹ Σ)), combustion radicals $n_{\rm rad}$ (O, OH, and H), and combustion products $n_{\rm prod}$ (CO, CO₂, and H₂O). The solution immediately after the applied

voltage (t = 6 ns) is presented in figure 4.5. The streamer channel is non-uniform radially, with a narrower structure near the anode (top), and a broader more diffuse structure near the cathode (bottom).

As observed in figure 4.6, the positive and negative streamers propagate with an average speed of approximately 10⁶ m/s, in good agreement with values reported in similar studies [159]. Following streamer connection, space charge shielding in the plasma channel results in a nearly uniform electric field across the gap.

It is observed that the most active regions (identified as areas with local maxima in the population of various plasma species) are located near the anode and cathode tips, as well as near the center of the channel (where the positive and negative streamer heads meet and connect to form the plasma channel). The regions near the pin tips are especially active, and undergo rapid heating and pressurization when the applied voltage is sustained after streamer connection. This is driven by local maxima in the reduced electric field strength during the propagation phase, near both the pin tips (due to the pin curvature) as well as in the center of the gap where the streamers connect.

The increase in temperature near the pin tips is driven by Joule heating, as demonstrated in figure 4.7(a), which shows the temporal evolution of the electron number density and reduced electric field strength at a point near the anode located approximately 1.8 μ m from the anode tip axially, and 0.63 μ m off the axis of symmetry (referred to as point 1). During the first 2.5 ns of the simulation (prior to streamer ignition), the electric field strength follows the sigmoid profile used to define the applied voltage. Once the positive streamer ignites (at time $\tau_{ig} = 2.6$ ns),

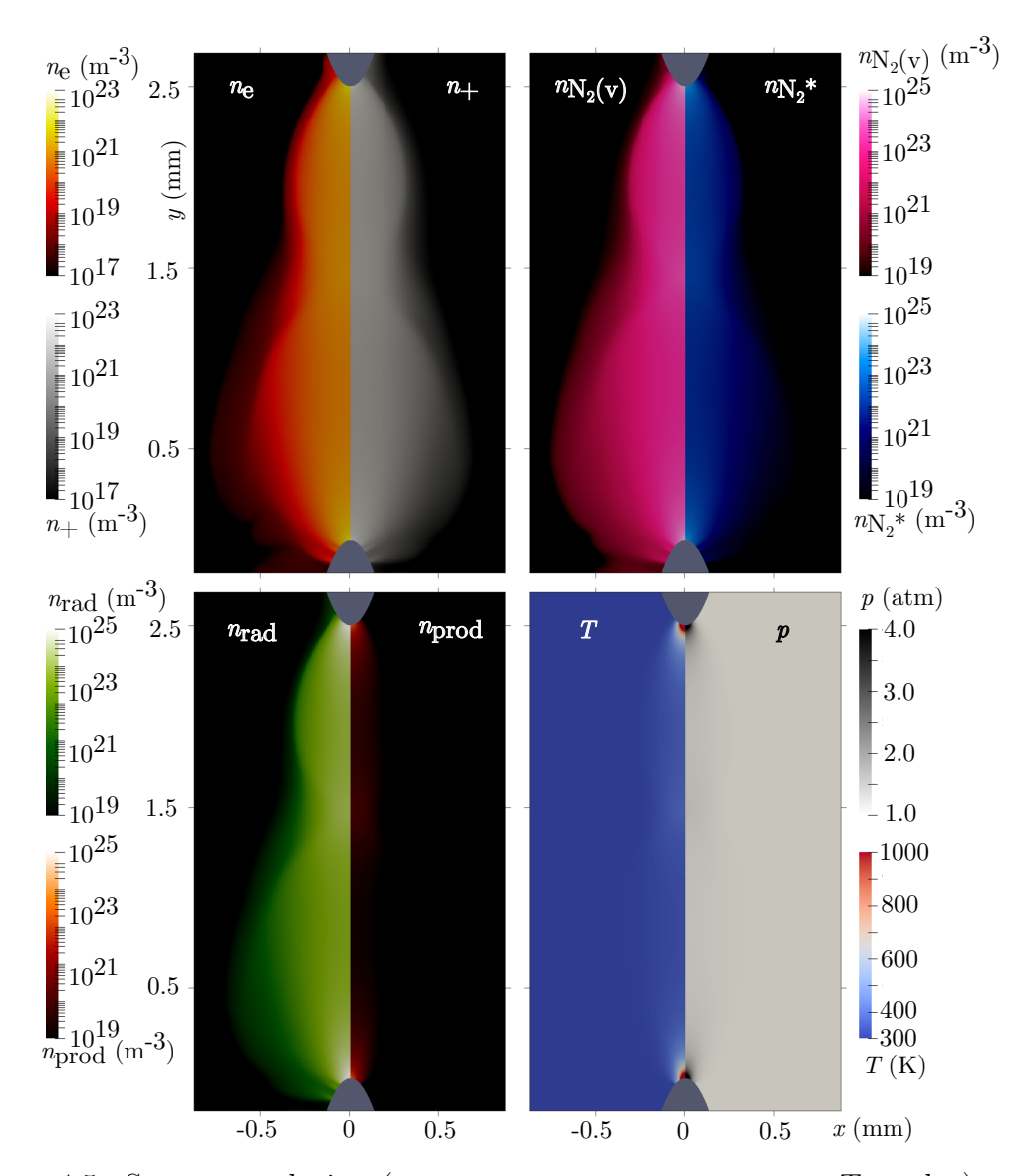


Figure 4.5: Streamer solution $(n_e, n_+, n_{N_2(v)}, n_{N_2^*}, n_{rad}, n_{prod}, T, and p)$ at 6 ns. The plasma channel is comprised of a narrow region formed by the propagation of the positive streamer, and a broader region from by propagation of the negative streamer.

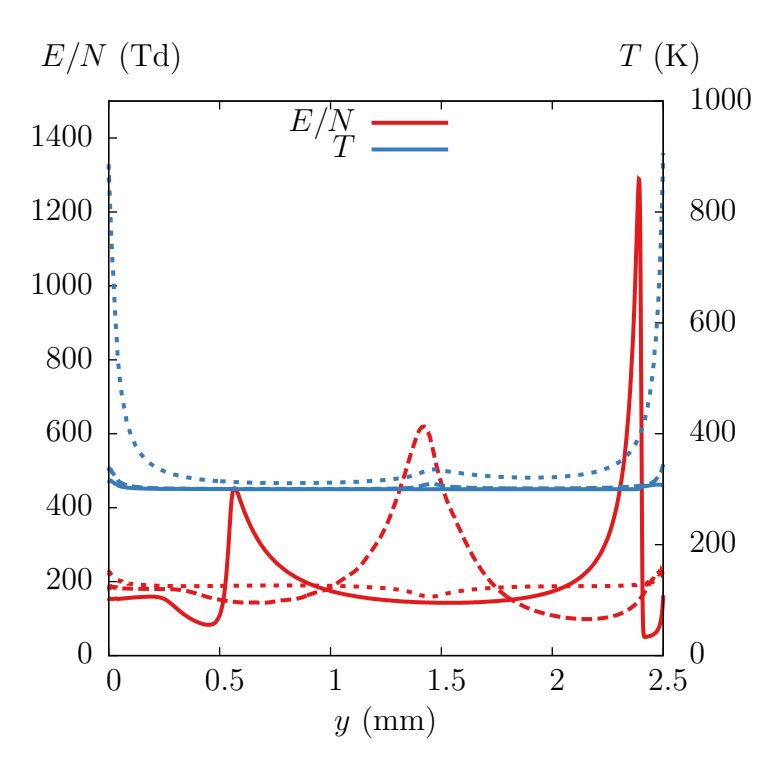


Figure 4.6: Reduced electric field and gas temperature along the axis of symmetry at 2.8 ns (solid lines), 3.7 ns (dashed lines), and 4.5 ns (dotted lines). Ignition of the positive streamer occurs at 2.6 ns, while streamer connection occurs at 3.7 ns.

the electron number density increases rapidly resulting in space charge shielding and an almost instantaneous reduction in the electric field strength.

There is a transitory phase as the streamers propagate and connect (at time $\tau_{conn} = 3.7 \text{ ns}$), after which the electron number density further increases by approximately an order of magnitude, eventually reaching a maximum between 4 and 5 ns. It is during this time that a vast majority of the energy is deposited by the pulse, as shown in figure 4.7(b). The heating of the gas coincides with the energy deposition, and peak temperatures in excess of 2000 K are observed near both the anode and the cathode. The temperature continues to rise even after the energy deposition phase, due primarily to the quenching of electronically nitrogen species, which are responsible for fast heating [144].

Detailed insight is provided in figure 4.8, which shows the streamer solution taken along the axis of symmetry immediately after the pulse. As noted previously, local maxima are observed near the cathode (y = 0 mm), anode (y = 2.5 mm), and the location where the streamers connect ($y \approx 1.5$ mm). The populations of excited plasma species are provided in figure 4.8(a). There is a strong correlation between the population of an excited species and its excitation energy $\delta \varepsilon$, whereby species with lower excitation energies are present in greater amount in the plasma channel. This is seen most clearly in the separation between the amount of $n_{N_2(v)}$ (which has excitation energies ranging from 0.29 to 1.47 eV), and the amount of electronically excited species (N_2^* , O_2^* , and O(1D) with excitation energies ranging from 0.98 to 11.03 eV). The population of $N_2(v)$ is one to two orders of magnitude greater than the population of electronically excited species. Likewise, the population of $N_2(v_1)$

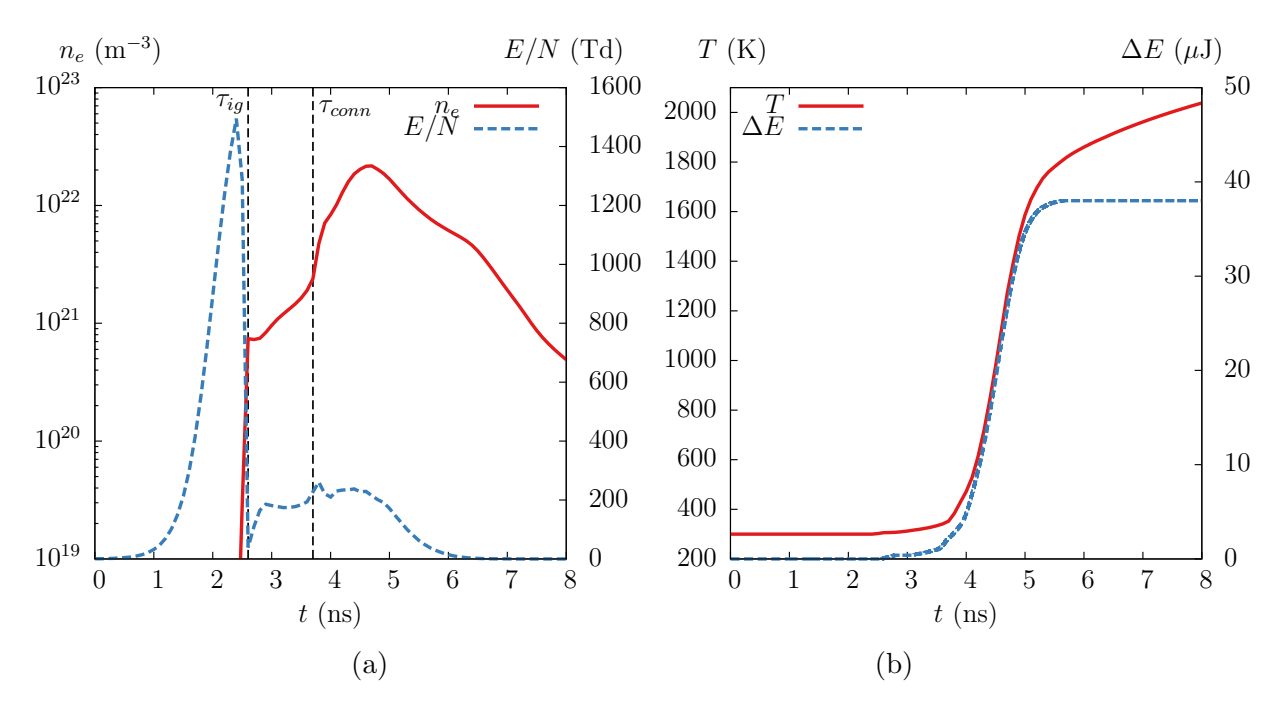


Figure 4.7: (a) Temporal evolution of the electron number density and reduced electric field strength at point 1, (b) temporal evolution of the temperature at point 1 and total energy deposited.

(which has the lowest excitation energy) is approximately an order of magnitude higher than the population of $N_2(v_5)$ (which has the highest excitation energy of the vibrationally excited species included in the model).

It is important to distinguish between vibrationally and electronically excited species due to the fact that they play vastly different roles in the context of ignition applications. As previously mentioned, the generation and subsequent quenching of N_2^* is largely responsible for fast heating. This process occurs over $\mathcal{O}(10 \text{ ns})$, and is responsible for a gas temperature rise of $\mathcal{O}(10\text{-}100 \text{ K})$. As discussed later in section 4.2.2.2, quenching of N_2^* also plays an important role in combustion radical generation. In contrast, $N_2(v)$ (and long-lived electronically excited species like metastable $O_2(a^1\Delta)$ and $O_2(b^1\Sigma)$) persist for much longer periods of time ($\geq 10 \ \mu s$). The quenching of $N_2(v)$ results in a much slower temperature rise known as slow heating [74]. Over shorter periods of time this heating is negligible, and the generation of vibrationally excited species acts as a energy sink, effectively trapping a portion of the pulse energy without any appreciable increase in the gas temperature or generation of combustion radicals.

The population of combustion radicals in the plasma channel is shown in figure 4.8(b). It is apparent that O is created in the greatest amount, followed by OH and H. This is consistent with previous investigations of LTP chemistry [37], which found that electron impact reactions and electronically excited species quenching primarily results in the formation of O, which in turn promotes the formation of H and OH radicals. Combustion products are also formed immediately following the pulse, albeit in much smaller amounts. The population of CO_2 is lower than the

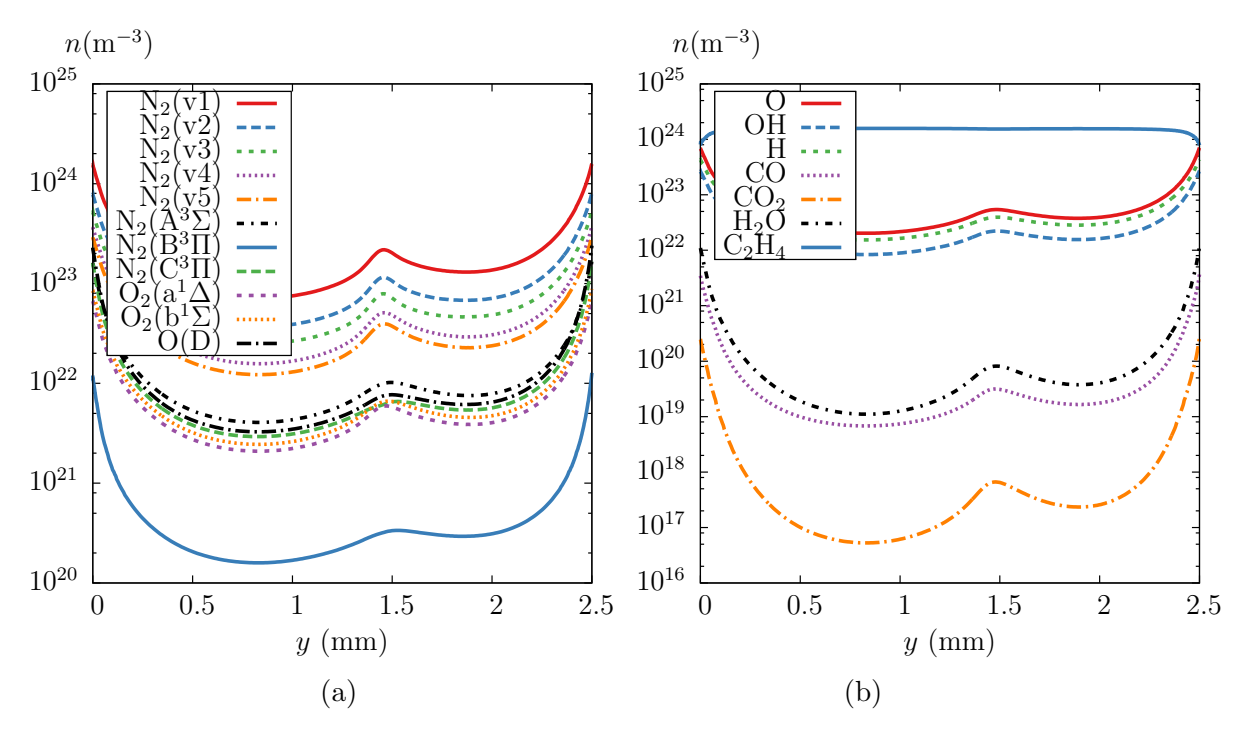


Figure 4.8: (a) Number densities of excited state species, (b) number densities of radical and product species along the axis of symmetry at 6 ns.

population of CO and H_2O by one to two orders of magnitude. Since conversion of CO to CO_2 is responsible for much of the heat release in conventional hydrocarbon combustion, this indicates that an *ignition event* is not imminent.

The temporal evolution of the solution (anion, cation, $N_2(v)$, N_2^* combustion radical, and combustion product mass densities integrated across the entire domain) over longer periods of time following the pulse is presented in figure 4.9. The species masses have been normalized using a reference mass $m_{\rm ref} = 2.29619 \times 10^{-6}$ g, which is the mass of the initial gas mixture in a cylindrical region with a height of 2.5 mm, and a radius of 0.5 mm (approximating the volume occupied by the plasma channel). Following the pulse, there is a transient period during which electrons

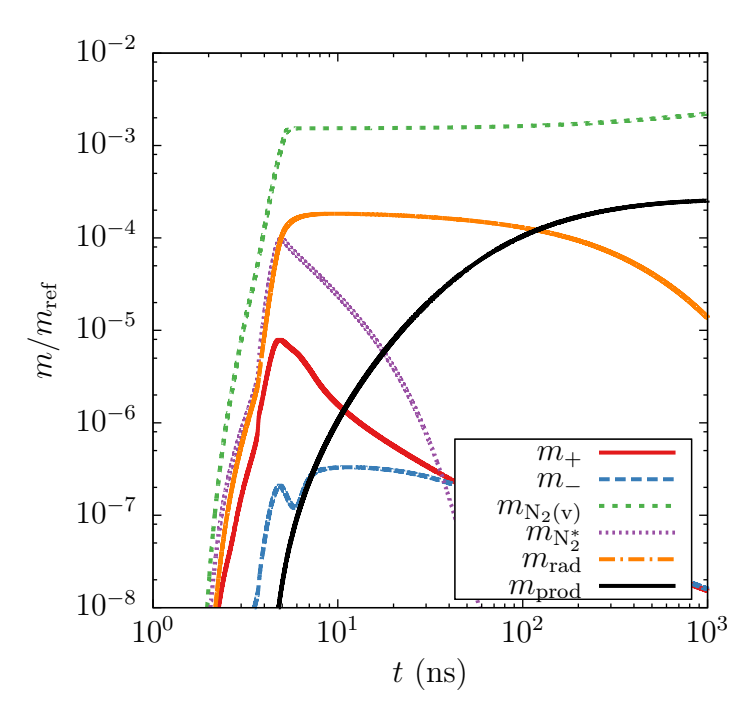


Figure 4.9: Temporal evolution of the total amount of cations, anions, vibrationally and electronically excited N₂, radicals, and products integrated across the entire domain, normalized using a reference gas mass $m_{\rm ref} = 2.29619 \times 10^{-6}$ g.

attach to O_2 and O_3 , after which the concentrations of cations and anions decay primarily due to ion-ion recombination reactions (R31-34). $N_2(v)$ remains present in large amounts long after the pulse, in contrast with N_2^* , which is rapidly quenched after $\mathcal{O}(10 \text{ ns})$. Combustion radicals are consumed over an interval $\mathcal{O}(0.1\text{-}1 \mu\text{s})$. Combustion products (primarily CO and H_2O) are produced both during the pulse and long after, as combustion radicals generated by the discharge are consumed in fuel oxidation reactions.

A more complete picture of the solution is provided by radial profiles at various instances in time and locations across the gap. Two radial profiles are taken across

the plane of symmetry: one profile across the top portion of the plasma channel near the anode (y = 0.5 mm) from the anode tip), and one across the bottom portion of the channel near the cathode (y = 0.75 mm) from the cathode tip). The solutions, provided in figure 4.10, are taken at three instants in time (t = 10, 100, 1000 ns). Solution profiles taken near the anode are denoted with an "a" subscript, while solutions near the cathode are denoted with a "c" subscript.

As apparent in figure 4.5, the radial extent of the plasma channel near the cathode is greater for all variables of interest. It is also observed that within the portion of the channel formed by the positive streamer (closer to the anode), the population of active species is greater than in the portion formed by the negative streamer (near the cathode). This is due to the fact that the reduced electric field strength in front of the positive streamer is larger than that in front of the negative streamer. This is apparent from the solution at 2.8 ns in figure 4.6, where the negative and positive streamer heads correspond with the maxima in E/N at $y \approx 0.5$ and $y \approx 2.4$ mm, respectively.

It is especially informative to consider the temporal evolution of these quantities. The population of electrons changes considerably due to electron attachment, decreasing by several orders of magnitude from 10 to 100 ns, and reaching negligible levels by 1 μ s. The populations of cations and anions decrease by a few orders of magnitude as well, as ion-ion recombination results in fewer ions over longer periods of time, and transport processes result in a more diffuse structure. Among excited species, significant variation is only observed for N_2^* which decreases considerably from 10 to 100 ns, consistent with the $\mathcal{O}(10 \text{ ns})$ time scales associated with N_2^*

quenching. Given the longer time scales associated with the relaxation of $N_2(v)$ and metastable O_2 , almost no variation is observed in the radial profiles for these species.

Combustion radicals are produced during the pulse, after which they are consumed during the inter-pulse period (decreasing in number density by one to two orders of magnitude in the plasma channel), as shown in figure 4.10(c). Finally, as seen in figure 4.10(d), the number density of combustion products and gas temperature increase due to fuel oxidation as well as fast and slow heating effects. The increase in the population of combustion products at such low temperatures is possible due to the presence of combustion radicals, which are present largely due to electron impact reactions, and N_2^* quenching. This highlights one of the primary benefits of using LTP in the ignition process. Combustion radicals are not present in such large amounts at low temperatures during traditional thermal ignition. Instead, conventional ignition requires that the gas temperature increase until chain branching leads to the production of combustion radicals, and fuel oxidation.

4.2.2.2 Generation and consumption of combustion radicals

Further insight into the role that combustion radicals play in the fuel oxidation process is gained by examining the reactions that contribute the most to their generation and consumption. As mentioned previously, energetic electrons have an important role in generating O radicals as well as H radicals, although to a lesser extent, through electron impact reactions that result in the dissociation of air and fuel species (R13-16). The quenching of electronically excited N₂ provides another

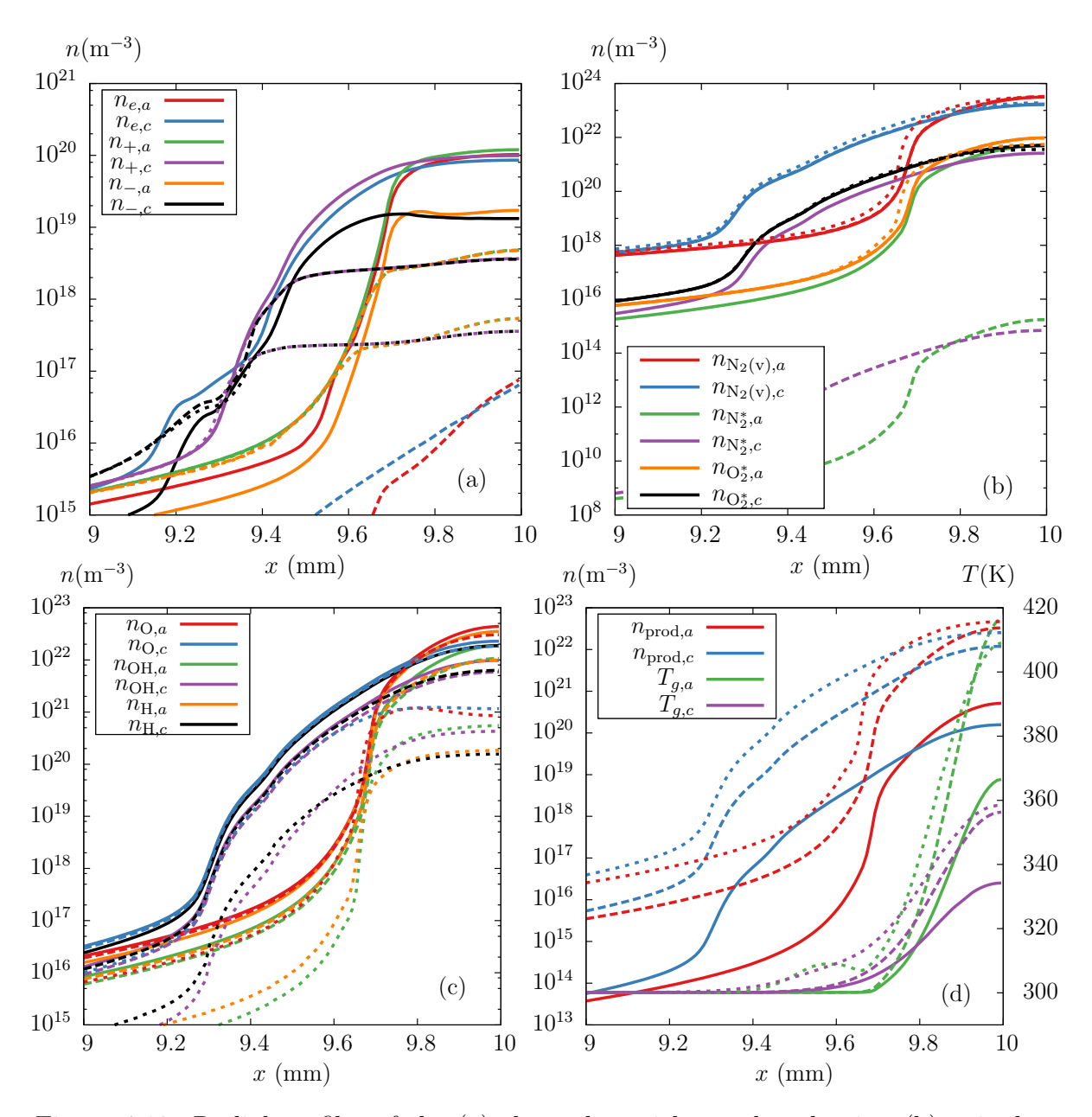


Figure 4.10: Radial profiles of the (a) charged particle number density, (b) excited species number density, (c) combustion radical number density, and (d) product number density and gas temperature, taken across the upper and lower portions of the plasma channel at 10 ns (solid), 100 ns (dashed), and 1 μ s (dotted).

important source of O and H radicals

$$N_2(A^3\Sigma) + O_2 \to N_2 + 2O$$
 (R35)

$$N_2(B^3\Pi) + O_2 \to N_2 + 2O$$
 (R36)

$$N_2(A^3\Sigma) + C_2H_4 \to N_2 + C_2H_3 + H$$
 (R37)

$$N_2(B^3\Pi) + C_2H_4 \to N_2 + C_2H_3 + H$$
 (R38)

$$N_2(C^3\Pi) + C_2H_4 \to N_2 + C_2H_3 + H.$$
 (R39)

O radicals go on to promote the formation of H and OH during fuel oxidation

$$C_2H_4 + O \leftrightarrow CH_2CHO + H$$
 (R40)

$$C_2H_4 + O(1D) \to C_2H_3 + OH$$
 (R41)

$$CH_3 + O \leftrightarrow CH_2O + H$$
 (R42)

$$CH_2O + O \leftrightarrow HCO + OH$$
 (R43)

$$HO_2 + O \leftrightarrow O_2 + OH,$$
 (R44)

while H radicals generate OH radicals also according to the well known reaction

$$HO_2 + H \leftrightarrow 2OH.$$
 (R45)

Reactions R40-43 also represent important steps in the fuel oxidation process, promoting the H-abstraction from ethylene (R40, R41), as well as the conversion of other intermediate species including methyl radicals (R42) and formaldehyde (R43).

Combustion radicals play important roles at all steps of the fuel oxidation process

$$C_2H_4 + O \leftrightarrow CH_3 + HCO$$
 (R46)

$$C_2H_4 + H \leftrightarrow C_2H_3 + H_2 \tag{R47}$$

$$C_2H_4 + OH \leftrightarrow C_2H_3 + H_2O$$
 (R48)

$$C_2H_4 + OH \leftrightarrow C_2H_3OH + H$$
 (R49)

$$C_2H_4 + OH \leftrightarrow PC_2H_4OH$$
 (R50)

$$C_2H_3 + H \leftrightarrow C_2H_2 + H_2 \tag{R51}$$

$$C_2H_3 + H \leftrightarrow H_2CC + H_2 \tag{R52}$$

$$C_2H_3 + OH \leftrightarrow C_2H_2 + H_2O$$
 (R53)

$$CH_2O + OH \leftrightarrow HCO + H_2O$$
 (R54)

$$CH_2O + H \leftrightarrow HCO + H_2$$
 (R55)

$$HCO + H \leftrightarrow CO + H_2$$
 (R56)

$$HCO + O \leftrightarrow CO + OH$$
 (R57)

$$HCO + O \leftrightarrow CO_2 + H$$
 (R58)

$$HCO + OH \leftrightarrow CO + H_2O.$$
 (R59)

The relative importance of these reactions during and after the pulse is illustrated in figures 4.11-4.13, which show the evolution of the forward production and consumption rates for reactions R35-R59 at a point near the cathode located approximately 2.5 μ m from the tip axially, and 2.5 μ m off the axis of symmetry (referred to as point 2). From figures 4.11(a) and (b), it is apparent that quenching of excited species dominates the evolution O early on, resulting in a peak in the population of

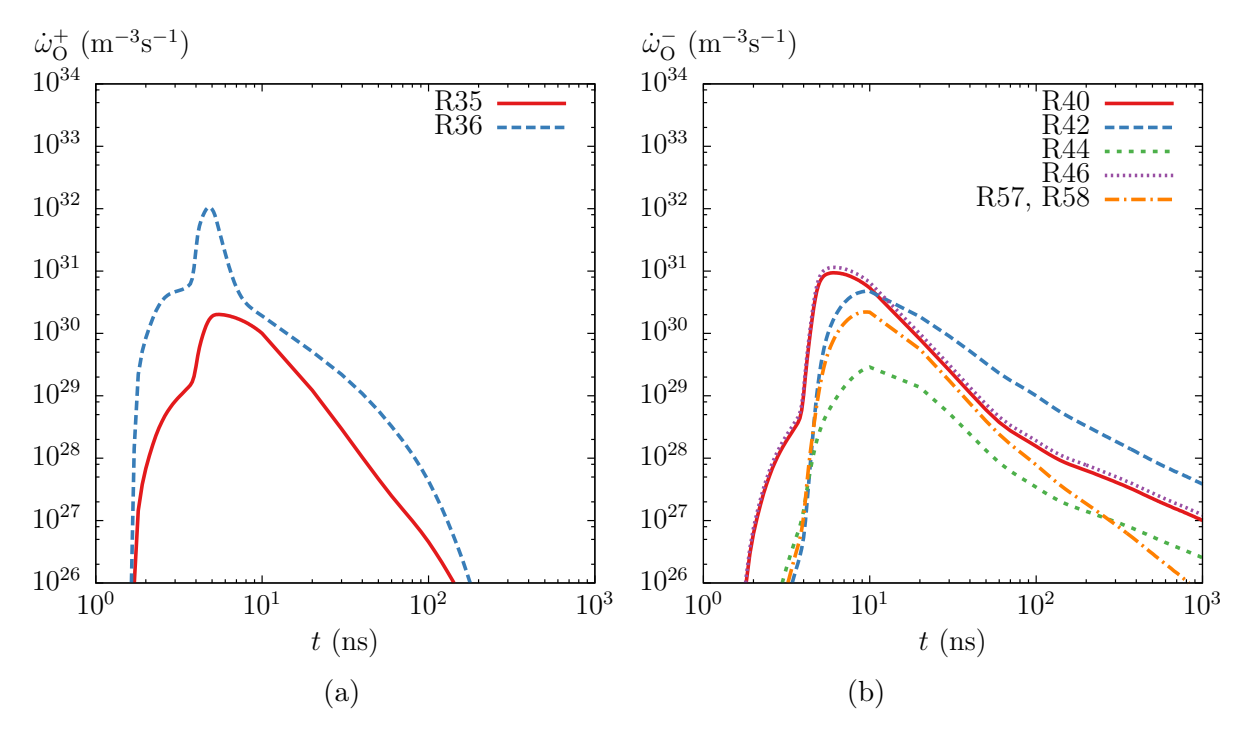


Figure 4.11: Temporal evolution of (a) production and (b) consumption of O at point 2 driven by key reactions.

O shortly after the pulse. The production of O quickly decreases by O (10 ns), at which point consumption pathways lead to a decrease in the overall amount of O. Specifically, H-abstraction of ethylene dominates towards the end of the pulse, after which conversion of methyl to formaldehyde primarily governs the evolution of O for the remainder of the inter-pulse period.

As with O, H radical production dominates during the early stages of the simulation. Quenching of N_2^* via reaction with ethylene governs the evolution of the H radicals through the first 100 ns, as shown in figure 4.12. Over longer periods of time, consumption of O through R40 and R42 produces H radicals, resulting in a lesser decrease in the rate of H production compared to O. During the early stages of

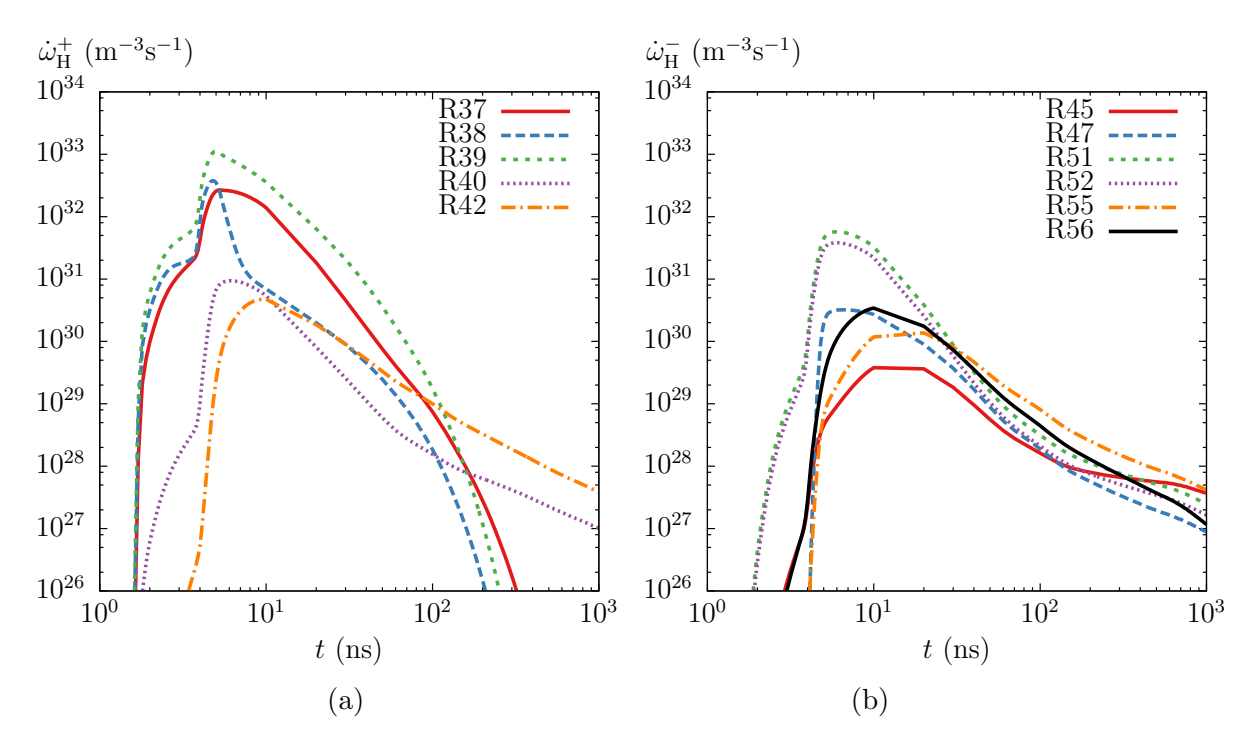


Figure 4.12: Temporal evolution of (a) production and (b) consumption of H at point 2 driven by key reactions.

the pulse, H is primarily consumed through reaction with ethylenyl (C_2H_3) to form acetylene (C_2H_2) and H_2CC . Further into the inter-pulse period, other fuel and fuel radical reactions acquire more dominant roles in the evolution of H as well, as H is consumed to convert ethylene (R47), formaldehyde (R55), and formyl (R56).

Excited oxygen radicals O(1 D) play a major role in generating OH radicals during and shortly after the pulse, as seen in figure 4.13(a). Following this, O and H promote the continued formation of OH, through reactions with formaldehyde and especially hydroperoxyl (HO₂). As with H, OH plays a role throughout the fuel oxidation process, as it is consumed to convert fuel and fuel radicals.

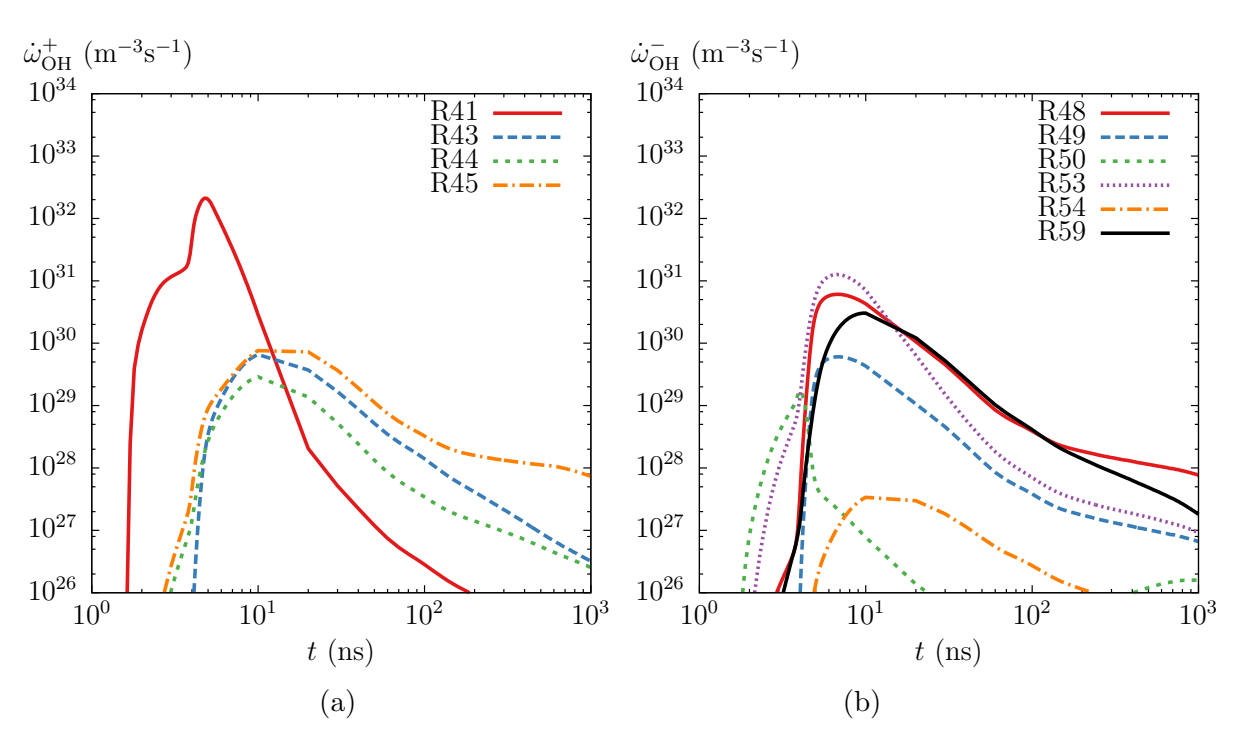


Figure 4.13: Temporal evolution of (a) production and (b) consumption of OH at point 2 driven by key reactions.

4.2.2.3 Barriers to successful ignition

During the pulse, kernels of heated and pressurized gas form near the electrode tips, as energy deposition in the gap is highly nonuniform. Since the energy deposition occurs on nanosecond timescales, it is effectively isochoric, and the gas density is unchanged immediately following the pulse. On timescales $O(0.1 - 1 \mu s)$, spherical shock waves develop and emanate from the electrode hot spots. These shock waves support sharp changes in pressure, density, and velocity as shown in figure 4.14. It is apparent that during the early stages of the shock wave formation, large gas velocities of approximately 250 m/s are observed along with pressures of several atmospheres, as shown in figure 4.15, which presents radial profiles located 0.05 mm from the anode tip at various instants in time. A much weaker cylindrical expansion wave is also observed, due to the fact that heating in the interior of the channel is significantly smaller than near the tips. Following the hydrodynamic expansion of the gas, a region of low gas density is observed in the channel, with especially large drops in density seen near the electrode tips.

It is important to understand the requisite conditions for a successful ignition in order to make predictions about whether a single pulse is sufficient to ignite the mixture. Following theory presented in [35], we adopt the concept of critical radius R_c which defines the minimum radius needed for a flame kernel to support sustained outward propagation. Additionally, each ignitable mixture has a minimum ignition energy (MIE) required for a successful ignition. There is a strong positive correlation between the critical flame radius and the mixture Lewis number Le, which is taken to be 1.2 for the purposes of this discussion [67]. From [35], this implies $R_c \approx 2\delta_t$,

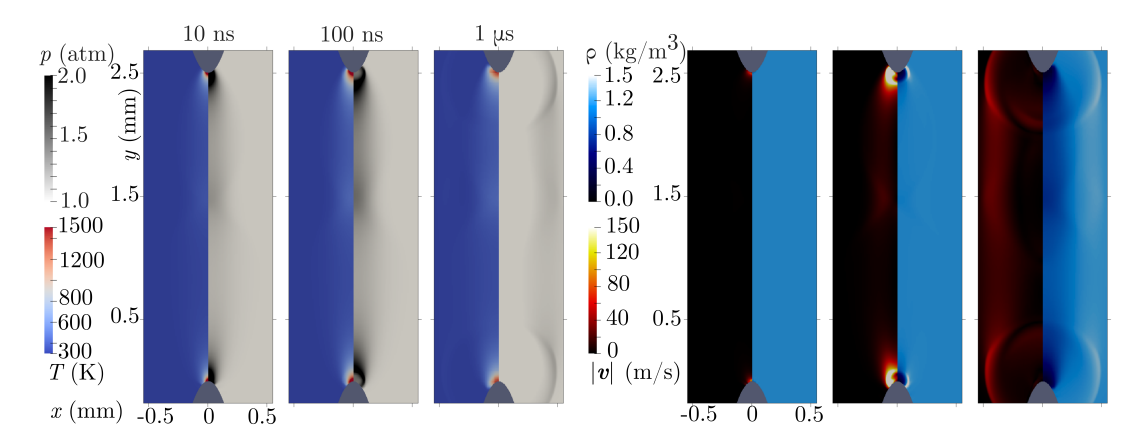


Figure 4.14: Heating and hydrodynamic expansion $(T, p, \rho, \text{ and } |v|)$ at 10 ns, 100 ns, and 1 μ m following the first pulse.

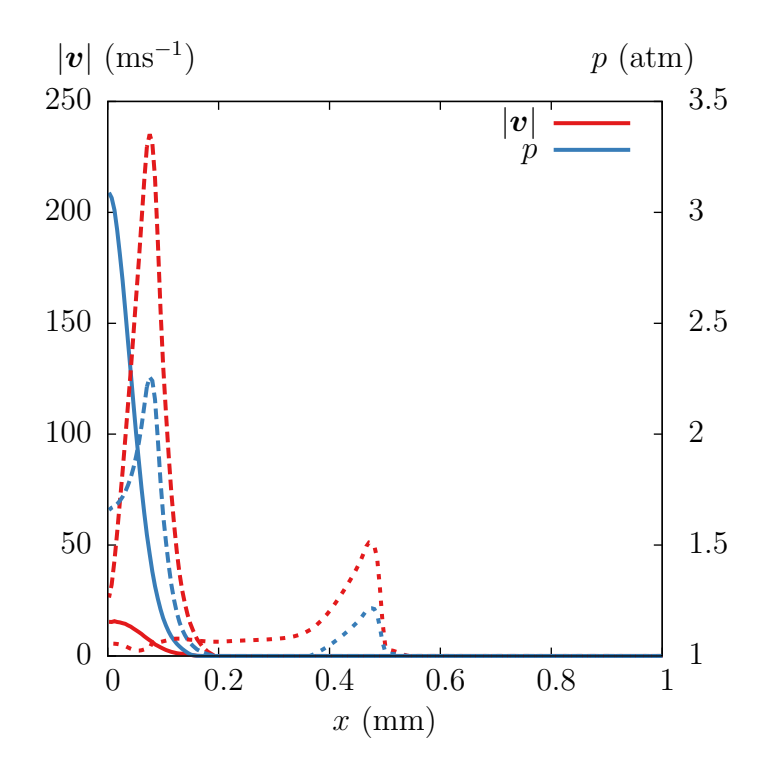


Figure 4.15: Radial profiles of the gas pressure and velocity magnitude, taken across the plasma channel 0.05 mm from the anode tip at 10 ns (solid), 100 ns (dashed), and 1 μ s (dotted).

where δ_t is the flame thickness. The flame thickness for a stoichiometric ethylene/air at atmospheric conditions was found to be $\delta_t \approx 300 \ \mu \text{m}$ in [85], yielding $R_c = 0.6 \ \text{mm}$.

It is readily apparent from the results presented in figure 4.14 that the radius of the heated kernel is of the same order of the radius of curvature of the electrode at the tip $r_c = 50 \mu m$, and thus much less than the critical radius required for ignition. Additionally, if one assumes that the entirety of the pulse energy is deposited within the electrode hot spots, approximately 20 μ J of energy are deposited within each kernel. This is less than the MIE reported for ethylene/air flames by approximately one order of magnitude [130, 171, 164]. Together, these results indicate that although the pulse produced significant temperature rise in small regions near the electrode tips, the pulse strength was not nearly sufficient to meet the criteria for ignition, as defined by R_c and the MIE. Broadly, such an occurrence highlights the difficulty in achieving PAI within a single pulse using thin pins (defined as having a small r_c) - the small radius of curvature drives large gradients in the solution, and excessive heating $(\Delta T > 2,000 \text{ K})$. However, since energy deposition occurs in a small region, criteria for the minimum flame radius and energy deposition are not met easily. Ignition without excessive gas heating can be achieved more easily by using thicker pins, which lead to a more spatially uniform energy deposition.

4.2.3 Multiple pulse dynamics

One of the most critical outstanding questions is that of the ideal pulsing strategy for PAI. Successful PAC ignition typically requires several pulses, with each pulse generating active particles. These particles are consumed during the inter-pulse period, resulting in incremental increases in the gas temperature, and population of combustion products. Once enough energy has been deposited into the gas mixture and the temperature/combustion radical populations are sufficiently elevated, chain branching reactions dominate and the mixture ignites rapidly. Under ideal conditions, each pulse forms of a channel of active particles, without leading to excessive heating ($\Delta T > 2,000 \text{ K}$) in the domain (in order to avoid electrode degradation and significant NO_x production).

The application of multiple pulses is explored first by simulating two pulses of the same strength ($\phi_{\text{max}} = 12 \text{ kV}$) separated by 2 μ s. All other conditions and pulse parameters are otherwise identical to those discussed in section 4.2.2. The evolution of key plasma metrics during the two pulses is shown in figure 4.16 at a point near the anode located approximately 7.3 μ from the anode tip axially and 2.5 μ m off the axis of symmetry (referred to as point 3). Data is shifted by the pulse start time $t_s = 0 \mu$ s for the first pulse, and $t_s = 2 \mu$ s for the second pulse. It is apparent that the streamer ignites sooner by about 0.5-1 ns compared to the first pulse, as evidenced by the difference in the time at which n_e increases suddenly in figure 4.16(a). The reduced electric field strength is also higher during the second pulse, due to the fact that the expansion of the gas near the pin tips after the first pulse results in a region of reduced number density.

The difference in the timing of streamer ignition also implies that streamer connection and transition to the spark regime occurs earlier. This is a particularly important point, as it was observed in section 4.2.2.1 that most of the pulse energy is

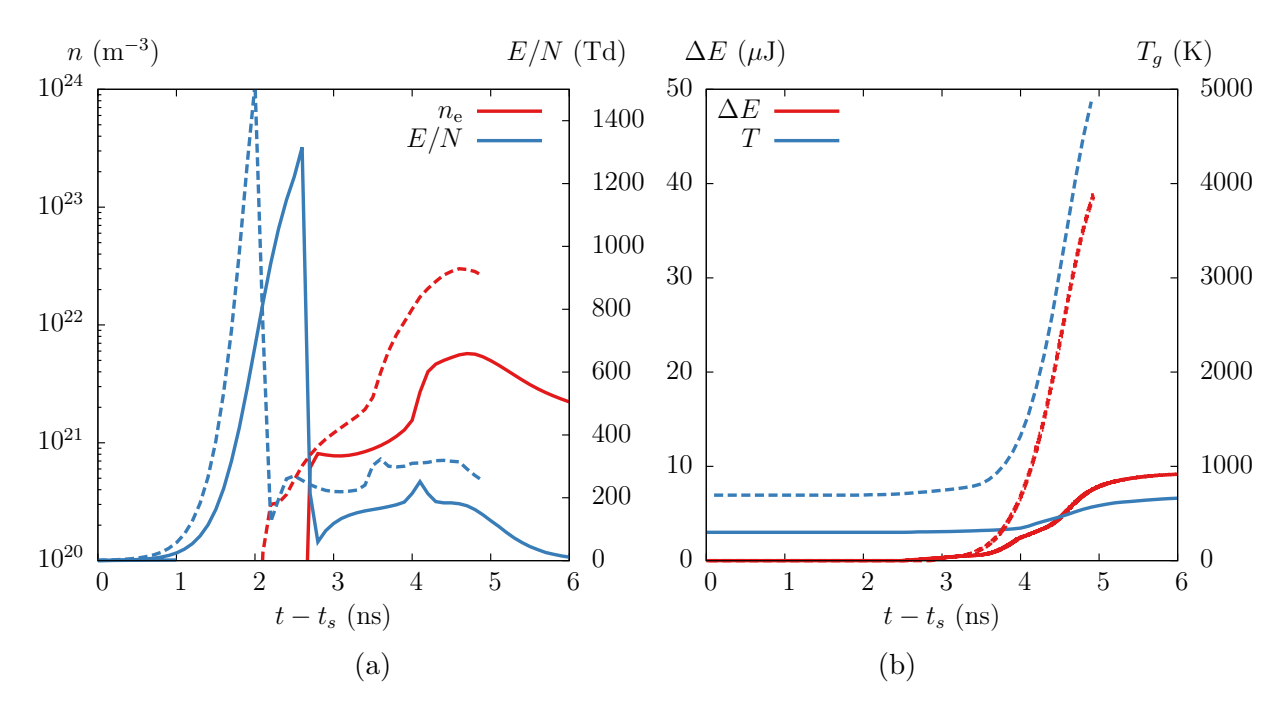


Figure 4.16: Temporal evolution during the first pulse (solid lines) and second pulse (dashed lines) of (a) electron number density and reduced electric field strength at point 3 and (b) temporal evolution of the temperature at point 3 and total energy deposited.

deposited following streamer connection. From figure 4.16(b), it is clear that heating and energy deposition are affected significantly. The energy deposited during the second pulse is higher by over a factor of 4, and the amount of heating near the electrode tip increases from $\mathcal{O}(100 \text{ K})$ to $\mathcal{O}(1000 \text{ K})$. This is due both to the earlier streamer connection time, as well as the higher E/N near the pin tips during the second pulse. Simulations are not conducted after the peak temperature in the domain reaches 5,000 K as the expressions for thermodynamic quantities used in this study (i.e. the specific heat capacity c_p) are not valid at higher temperatures.

It has been established that pulse strength and streamer timing both have

a significant impact on heating and energy deposition. It was found that for the case under consideration, the second pulse must be weaker than the first to avoid excessive heating ($\Delta T > 2,000 \text{ K}$).

Discussion of how behavior changes over multiple NSD concludes with an examination on how pulse frequency impacts the pulse timing and thus heating and energy deposition characteristics. Simulations of two NSD are performed using pulse separations of 2 μ s (f = 500 kHz) and 5 μ s (f = 200 kHz), and a peak voltage of $\phi_{\rm max} = 10$ kV for the second pulse. Temporal evolution of the solutions at point 3 during the second pulse are shown in figure 4.17, where the pulse start time $t_s = 2$ μ s for the first pulse and 5 μ s for the second pulse. As the period for higher frequency is shorter, the degree of preionization in the channel for the 500 kHz case is greater as there is less time for charge recombination, leading to a slightly faster ignition. The populations of charged particles and active species increase sooner, reaching higher values through the pulse period. The higher electron number density and electric field strength for the 500 kHz case result in greater energy deposition through Joule heating.

It is interesting to note that quantities that differ significantly between the two cases at the beginning of the second pulse reach similar values by the end of the pulse. Species that relax over time scales comparable to the pulse period (for instance combustion radicals) are seen to differ by an order of magnitude or more at the onset of the pulse, but reach nearly identical values after. There is a more noticeable increase in the gas temperature for the 500 kHz case, which sees approximately 20% more thermal heating in the region. This is an important finding which highlights

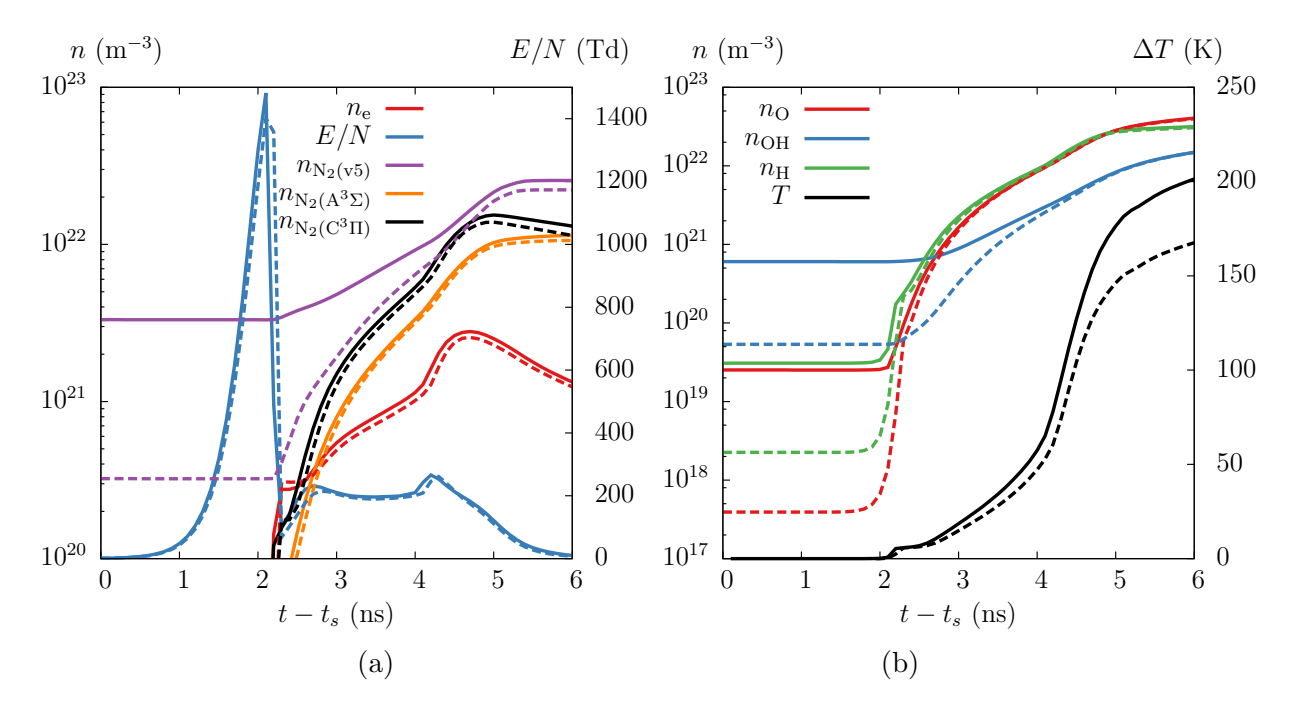


Figure 4.17: Temporal evolution during the second pulse at 500 kHz (solid lines) and 200 kHz (dashed lines) of (a) electron and excited species number number densities and reduced electric field strength and (b) number densities of select combustion radicals and temperature at point 3.

that even minor changes in the pulse timing, and the evolution of the charged and active species can produce sizeable changes in the evolution of important combustion quantities, such as the gas temperature.

The above discussion can be summarized by concluding that the pulse strength and conditions in the gap prior to the pulse, and their impact on streamer timing primarily govern heating and energy deposition in the gap. Holding all else constant, there is a secondary dependence on pulse frequency, with more frequent pulses leading to greater heating and energy deposition due to greater preionization prior to onset of the NSD.

4.2.4 Streamers at elevated temperatures and pressures

In order to characterize ignition at conditions more relevant to combustion devices where gas compression can lead to high pressures and temperatures, simulations at elevated initial pressures and temperatures are conducted. Gas mixtures at elevated initial temperatures and pressures chosen from table 4.3 are used to initialize each simulation. It was found in [37] that in order to obtain comparable heating and energy deposition at different p_0 and T_0 , the applied voltage peak ϕ_{max} needs to be adjusted to account for the changing gas number density. However our preliminary study presented in figure 4.4 suggests that pulse strength does not scale linearly with increases in N_0 at constant energy deposition, rather higher p_0 and T_0 require weaker pulses.

The atmospheric case with $\phi_{\text{max}} = 13 \text{ kV}$ presented in section 4.2.2 is compared against a case at 400 K using a peak applied voltage $\phi_{\text{max}} = 21.2 \text{ kV}$. Note that scaling the applied voltage directly with N_0 results in $\phi_{\text{max}} = 26.7 \text{ kV}$, which was found to drive elevated heating near the electrodes $\mathcal{O}(10,000 \text{ K})$. All other pulse parameters are held constant. The energy deposited during the pulse (scaled using N_0 and a common reference number density N_{ref}) is presented in figure 4.18, in order to confirm that the (normalized) amount of energy deposited differs by only a small percentage between the two cases.

Qualitative comparisons can be made by examining species mole fractions shortly after the pulse (t = 10 ns), as shown in figure 4.19. It is apparent that charged species are produced efficiently (as defined by higher mole fractions X) at lower pressures ($T_0 = 300$ K, $p_0 = 1$ atm). This is due to the fact that a lower

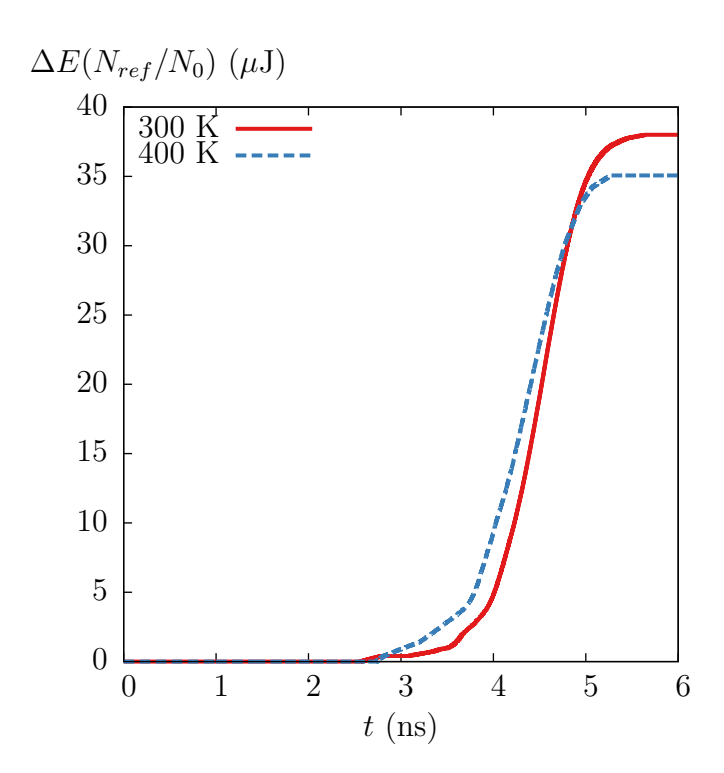


Figure 4.18: Temporal evolution of the total deposited energy scaled using the initial gas number density N_0 and a reference gas number density $(N_{ref} = 2.446 \times 10^{25} \text{ m}^{-3})$ for the 300 K and 400 K cases.

reduced electric field strength (E/N) is applied at higher pressure and temperature $(T_0 = 400 \text{ K}, p_0 = 2.7 \text{ atm})$, as the ϕ_{max} was not scaled directly with N_0 . This is seen clearly in figure 4.20(a), which shows the evolution of the reduced electric field strength at point 3. It is well known that when using the local field approximation (LFA), E/N plays a key role in determining quantities such as the electron impact rate coefficients, with higher values of E/N resulting in greater rates of ionization and electronically excited species production. This also explains why the mole fraction of electronically excited species following the pulse is greater at lower pressures and temperatures.

In order to compare the two cases quantitatively, the temporal evolution of the reduced electric field, mole fractions, and gas temperature during the first 100 ns at point 3 are provided in figure 4.20. Several conclusions can be drawn. As previously observed, it is apparent from figure 4.20(a) that stronger reduced electric fields are present in the vicinity of the electrodes throughout the entire pulse, resulting in larger charged particle mole fractions, given the high electron energies needed for ionization. It is also apparent that the streamers at elevated pressure and temperature ignite and connect sooner.

From figure 4.20(b), it is also apparent that the peak rate of production (normalized by N_0) of N_2^* is higher at lower pressure, while that of $N_2(v)$ and O_2^* is higher at higher pressures. These findings are consistent with the fact that energies for electronic excitation of N_2 are higher compared with energies for vibrational excitation of N_2 and and electronic excitation of O_2 , and stronger electric fields are required.

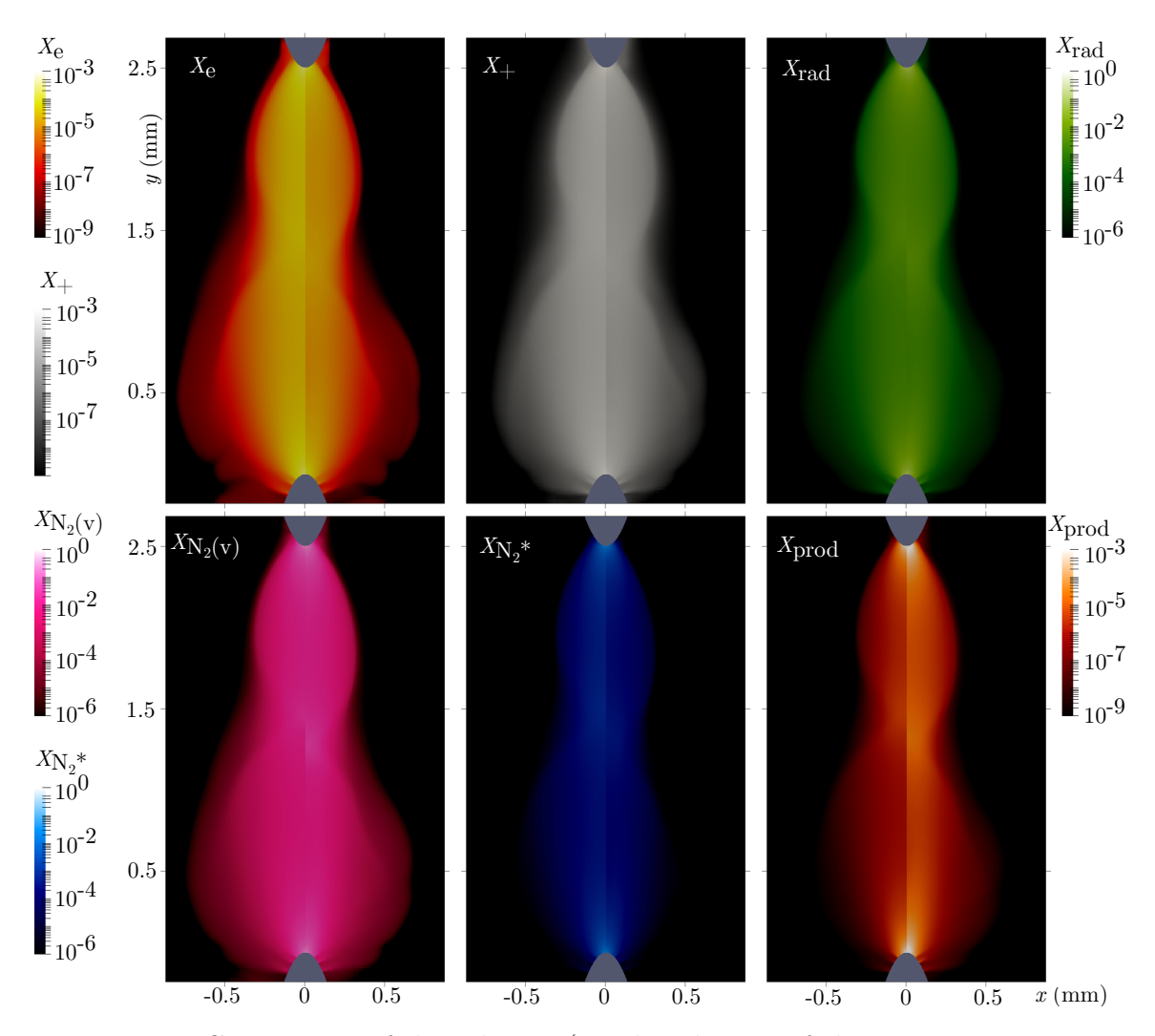


Figure 4.19: Comparison of the solution (number density of electrons, cations, combustion radicals, vibrationally and electronically excited N_2 , and combustion products, normalized by N_0) for the 300 K (left panels) and 400 K (right panels) cases at 6 ns.

Despite the larger mole fractions of N_2^* (which generate combustion radicals efficiently when quenched) at lower pressures, higher combustion product mole fractions are observed in the high pressure case, as shown in figure 4.20(c). This is due primarily by the difference in streamer timing, as faster streamer evolution at higher pressure results in more time for generation of active particles and energy deposition. It is also apparent that although the peak mole fraction of N_2^* is greater at lower pressure, $X_{N_2^*}$ remains higher at high pressure until between 4 and 5 ns, which is when radical production starts declining.

More differences are observed in gas heating and combustion products, as shown in figure 4.20(d). While the evolution of temperature is similar early during the pulse, more gas heating at higher pressure is observed. This is due to more efficient quenching of excited species at higher pressure (from figure 4.20(c), it is apparent that the relative consumption of N_2^* is greater at higher pressure until approximately 45 ns). As noted earlier, combustion products are created more efficiently at higher pressure. Several factors contribute to this, including faster streamer ignition, larger radical mole fractions, and higher temperatures. Increased generation of combustion products at higher pressures contradicts earlier findings from [37]. In this earlier study, simulations were conducted in a zero dimensional reactor, which considerably simplified the plasma assisted ignition process. The findings presented here underscore the complexity of plasma-assisted ignition, and highlight the need for continued improvements to predictive multidimensional simulations with high-fidelity models for plasma discharges and combustion chemistry.

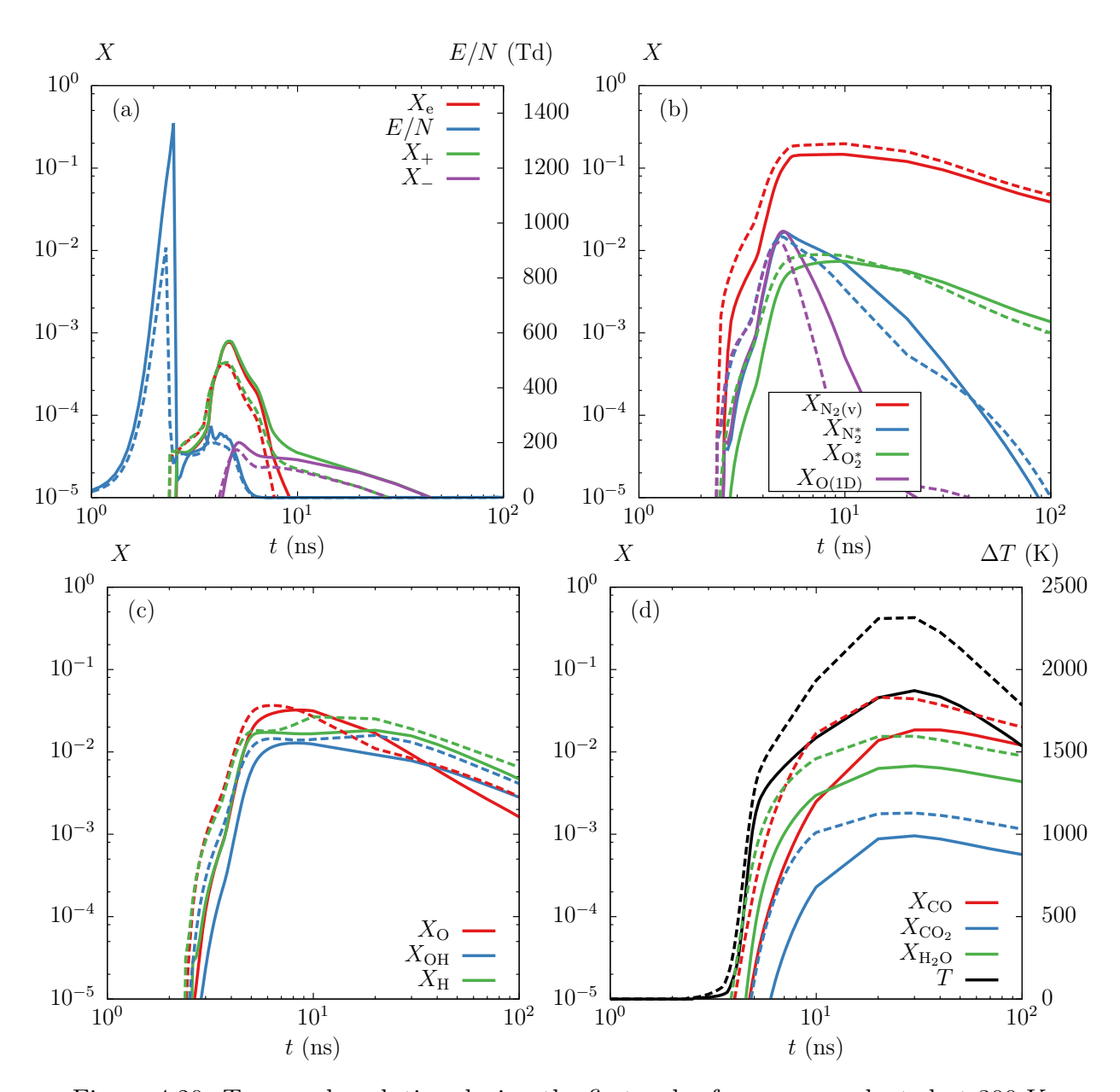


Figure 4.20: Temporal evolution during the first pulse for cases conducted at 300 K and 1 atm (solid lines) and 400 K and 2.7 atm (dashed lines) of (a) the charged species number number densities and reduced electric field strength, (b) excited species number densities, (c) combustion radicals number densities, and (d) combustion product number densities and temperature at point 3.

Chapter 5

Summary and conclusions

The work presented in this dissertation focused on developing and applying a robust framework for simulating hydrocarbon/air ignition via NSPD in multiple dimensions. First, the ignition of methane and ethylene/air mixtures was investigated in an isochoric adiabatic reactor in order to understand how fuel type, pressure, and pulse parameters impact ignition efficiency. Next, a reactive Navier-Stokes solver was extended to include a plasma-fluid model with two-way coupling between plasma and fluid. Axisymmetric simulations of plasma streamers in air were then conducted, and the evolution of the plasma sheath and its dependence on modeling choices at the boundary were examined. Finally, these simulations were extended to employ a skeletal plasma ethylene/air combustion mechanism and important ignition aspects, including heating and energy deposition during the pulse as well as combustion radical production and consumption, were analyzed and discussed.

The primary contribution of this work is the development, implementation, and application of a plasma discharge solver with two-way coupling between the plasma-fluid model and reactive Navier-Stokes equations capable of conducting multidimensional simulations using an adaptive mesh refinement framework. This solver was used to gain a comprehensive understanding of how important problem parame-

ters, such as pressure, fuel type, pulse characteristics, and problem geometry impact ignition.

A summary of important findings from each of the chapters is presented next, followed by recommendations for future areas of work.

5.1 Kinetic enhancement of plasma-assisted ignition

While experimental investigations of plasma-assisted ignition have been carried out extensively under low and atmospheric pressure conditions, relatively few studies have examined how the kinetic enhancement brought by plasma discharges changes at higher pressure for common hydrocarbon fuels. To bridge this gap, ignition of methane/air and ethylene/air mixtures was simulated in a zero-dimensional reactor, with a kinetic model that couples low-temperature plasma and combustion kinetics. A wide range of initial pressures were explored (spanning 0.5 to 30 atm), along with changing pulse frequencies (5 to 500 kHz), pulse FWHM (15 to 60 ns), and energy density depositions (15 to 15,000 mJ cm⁻³).

One key finding was that the time to ignition τ depends strongly on fuel type, initial pressure p, and energy deposition rate W. For the fuels considered in this study, τ was fit to a power law of the form

$$\tau = C(W/W^*)^a (p_0/p)^b, \tag{5.1}$$

and excellent agreement was observed across a wide range of pulse conditions.

The ignition time displayed several secondary dependencies as well, most notably on the pulse FWHM and frequency. It was observed that holding the energy deposition rate, pressure, and fuel type constant, the application of shorter pulses at lower frequencies lead to more efficient ignition. This was largely driven by the fact that for a given energy deposition rate, the application of shorter and less frequent pulses implies a stronger pulse with greater energy deposition per pulse. These factors contribute to generate active species and combustion radicals more efficiently during each pulse, which in turn promotes shorter ignition times.

The time to ignition τ was then compared with the thermal ignition time τ_T , and it was observed that PAI is more efficient at low pressures for both fuels, i.e. it leads to a time to ignition that is shorter than the thermal ignition time. PAI becomes relatively less efficient with increasing pressure, with this trend being more apparent for methane/air mixtures. The decrease in performance with increases in pressure is in part tied to the peak mean electron energy during the pulse, which decreases with increasing pressure, leading to fewer excited species, and thus fewer combustion radicals (on a normalized basis).

The poor performance of PAI for methane/air mixtures at high pressure (30 atm) is due to an inability to generate HCO from formaldehyde efficiently, caused by a lack of available H, which is converted to HO_2 by O_2 at high pressures. On the other hand, ethylene/air mixtures are more resilient to increasing pressure due to several bypass reaction pathways, which allow for the generation of HCO and CO from ethylene, ethylenyl, and vinoxy, thus circumventing the $CH_2O \rightarrow HCO$ bottleneck.

5.2 Implementation of a multidimensional NSD solver

In order to perform multidimensional simulations of nanosecond discharges and the subsequent plasma-assisted oxidation of hydrocarbon/air mixtures, a robust and efficient reactive Navier-Stokes solver was extended to include a plasma-fluid model. A local field approximation was used to parameterize electron transport coefficients and rate coefficients for electron reactions as functions of the reduced electric field. A two-way coupling strategy was used to ensure that plasma and reactive transport processes interacted with each other throughout the discharge and inter-pulse period.

Given the separation between the time scales that define plasma and combustion physics, special consideration was given to the efficiency of the solver. An AMR strategy was used to ensure that large gradients in the reduced electric field strength, pressure, and temperature (which correspond with important physical structures in the discharge solution) were resolved while maintaining a manageable problem size. A semi-implicit approach for solving Poisson's equation for the electric potential was implemented along with an implicit strategy for integrating electron diffusive sources in order to overcome stringent time step size restrictions both during and after the discharge.

5.3 Streamers in air and the cathode sheath

The simulation of plasma discharges presents an imposing challenge and is characterized by severely restricted time step sizes O(0.1-1 ps), complex physical structures that require $O(1 \mu\text{m})$ grid resolution, and tight coupling between phys-

ical processes (for instance between the evolving space charge and electric field). One physical structure that arises during the discharge's evolution is the cathode sheath, which is characterized by large gradients and elevated electric fields $\mathcal{O}(1000\,\mathrm{Td})$. In most numerical studies of PAI, the sheath is either eliminated entirely (through application of homogeneous Neumann boundary at the electrode surface), or left undiscussed. Its presence however has important implications for the solution, significantly modifying currents and heating near the cathode surface, as well as impacting the voltage and electric field across the gap.

In order to address these limitations, simulations of axisymmetric pin-to-pin streamer nanosecond discharges in atmospheric air were performed using the NSD solver. Parameters were varied to explore the effects of geometry, applied voltage, and electron emission at the electrode surface. Special consideration was given to the cathode sheath, which forms as electron drift and secondary emission processes create a region with significant space charge separation, and strong electric fields.

It was found that for a typical case, positive (cathode-directed) and negative (anode-directed) streamers ignite within a few nanoseconds, and propagate towards the center of the gap, forming a channel of charge-neutral plasma. Formation of the plasma sheath coincided with ignition of the negative streamer when electron loss and secondary emission processes were considered at the cathode surface, and supported reduced electric field strengths $\mathcal{O}(1000 \text{ Td})$. Such conditions lead to a reduction of the requisite time step size below 1 ps due to a CFL condition based on the electron drift velocity. It was also observed that when a charged particle flux consistent with a homogeneous Neumann boundary condition for the charged particle

number densities was imposed, the flux of electrons from the cathode surface was sufficiently large to eliminate the cathode sheath entirely, impacting the behavior of the negative streamer, and significantly reducing the computational cost of the simulation.

Next, the impact of photoionization, preionization, gap configuration, and applied voltage strength on streamer ignition and propagation behavior was investigated. It was observed that while lower preionization levels lead to delayed ignition but faster propagation of the positive streamer, ignition of the negative streamer and formation of the cathode sheath were less affected, with similar cathode fall values observed for both high and low preionization values. Alternatively, inclusion of photoionization processes had a minimal effect on the positive streamer, but resulted in a thinner cathode sheath with a smaller cathode voltage fall. Changes in gap length and applied voltage strength generally only impacted the timing of the formation of the cathode sheath, with more significant changes in the sheath thickness observed with changes in the radius of curvature of the pin. A more complex set of dependencies were found for the cathode voltage fall, with shorter gap lengths and stronger applied voltages leading to greater falls.

5.4 Ignition of ethylene/air mixtures using nanosecond pulsed discharges

To complete the investigation of plasma-assisted ignition discussed in this dissertation, a skeletal ethylene/air mechanism derived from the detailed mechanism discussed in chapter 2 was incorporated into the NSD solver. Axisymmetric pin-to-

pin plasma discharges in stoichiometric ethylene/air mixtures were simulated through the entire evolution of the streamer (including streamer ignition, propagation, and connection phases, as well as the subsequent spark phase) and through the inter-pulse phase. Single-pulse and two-pulse simulations were conducted using varying pulse frequencies and initial conditions to gain a broad understanding of how important parameters impact PAI.

First, a single-pulse simulation at atmospheric conditions was conducted using a voltage pulse with a peak of $\phi_{\text{max}} = 13 \text{ kV}$, which was sufficient to induce a temperature rise of approximately 2000 K near the electrode tips during the spark phase. The solution was then examined through the first 2 μ s of the simulation. The composition of the plasma channel was discussed in detail and it was shown that following the pulse, vibrationally excited N₂ dominated the population of excited state species, while the production of O dominated radical production. These observations are consistent with findings from the zero-dimensional study in chapter 2.

A peak temperature rise of approximately 2000 K near the pin tips, and a total energy deposition of 38 μ J were observed for the single-pulse case. The size of the heated and pressurized kernels near the electrode tips and deposited energy were compared against the minimum flame radius and minimum ignition energy (MIE) for the mixture, and it was found that these criteria were not met, indicating that a single pulse was insufficient to achieve mixture ignition. This was primarily due to the small radius of curvature of thin pins, which resulted in large gradients in the electric field in small regions near the electrode tips, limiting the energy deposition mostly to these regions. Deposition of energy sufficient to meet MIE requirements

would have resulted in excessive heating ($\Delta T > 5{,}000$ K), and it was concluded that successful ignition from a single pulse requires thicker pins, which would result in shallower electric field gradients in the gap and thus more uniform heating and energy deposition.

Next, a simulation was conducted using two identical voltage pulses with $\phi_{\rm max}=12~{\rm kV}$ and an inter-pulse duration of 2 $\mu{\rm s}$. While the peak heating and energy deposition during the first pulse were modest ($\Delta T=200~{\rm K}$ and $\Delta E=10~\mu{\rm J}$), heating of several thousand K and energy deposition over 40 $\mu{\rm J}$ of energy deposition were observed during the second pulse prior to its completion. This was due to two factors. Following the hydrodynamic expansion in the gap after the first pulse, a lower number density was present prior to application of the second pulse, resulting in stronger reduced electric fields. Additionally, higher preionization in the channel prior to the second pulse resulted in faster streamer ignition and connection, leaving more time for energy deposition during the spark phase (for a second pulse duration equal to that of the first pulse).

Finally, the impact of elevated temperature and pressure on the solution was briefly considered. A simulation of stoichiometric ethylene/air at $T_0 = 400$ K and $p_0 = 2.7$ atm was conducted using $\phi_{\text{max}} = 21.2$ kV, and compared against the single pulse case. It was observed that the mole fraction of electronically excited species after a single pulse was largest at lower pressure due to higher reduced electric field strengths during the pulse, while the mole fraction of vibrationally excited species was higher in the elevated pressure case for the same reason. It was also found that the mole fraction of combustion products at higher pressure was higher, due to

slightly faster pulse ignition. This finding contradicts observations from the study conducted in chapter 2, indicating that a zero-dimensional treatment of the problem is not sufficient to capture the complexity of PAI, and highlighting the need for development of robust predictive multidimensional tools to approach the problem.

5.5 Recommendations for future work

The work presented in the studies discussed in this dissertation can be extended and improved, with the goal of developing better predictive tools for simulating PAI.

1. Incorporation of a local mean energy approximation:

While the use of a local field approximation (LFA) is suitable when gradients in the electric field are sufficiently small, it is known that when gradients are larger, the local mean energy approximation (LMEA) is more appropriate and accurate. The extension of the computational model discussed in this study to use a LMEA is an important step for conducting predictive PAI simulation that include the presence of the cathode sheath (which supports particularly large gradients in the electric field).

2. Development of a circuit model:

While the simulations conducted in this study modeled the applied voltage at the anode as having a sigmoid profile directly controlled by user-defined parameters, this is a simplistic approximation. It is known that the applied voltage at the anode is strongly impacted by the circuitry used to generate the pulse, the electrical characteristics of the combustion chamber that contains the pins, and the displacement and conduction currents associated with the conducting plasma channel that forms during each discharge. Future modeling efforts need to account for this important aspect of the problem in order to produce results that can be directly compared with experimental data.

3. Simulation of PAI with the electrode sheaths:

The simulations of ethylene/air oxidation conducted in chapter 4 used homogeneous Neumann, conditions which prevented the formation of the electrode sheaths, primarily due to the computational cost associated with simulating these structures. Future work should focus on conducting PAI with the sheaths included (together with a plasma fluid model based on the LMEA), as their presence has a known effect on the currents, temperature, and energy deposition near the electrodes.

4. Simulations of PAI in turbulent environments:

Nearly all numerical studies of NSD and PAI in both air and air/fuel mixtures have been conducted in quiescent environments, despite the fact applications of practical interest operate in turbulent environments. Spatial imhomogeneity in the gas temperature and density can impact the propagation of the streamer during the discharge phase, while turbulent transport can modify the channel of active particles formed during the discharge during the inter-pulse period. With a solver capable of conducting three-dimensional simulations, novel research into how turbulence impacts the PAI process can be conducted.

Appendices

Appendix A

Rate coefficient fitting for electron reactions

${\bf Appendix~B}$ Detailed PAC mechanism

${\bf Appendix~C}$ Reduced ethylene/air mechanism

Bibliography

- [1] Pelec documentation. https://pelec.readthedocs.io/en/latest/index.html. Accessed: 2022-03-08.
- [2] I Adamovich, Scott D Baalrud, A Bogaerts, PJ Bruggeman, M Cappelli, V Colombo, Uwe Czarnetzki, U Ebert, James Gary Eden, P Favia, et al. The 2017 plasma roadmap: Low temperature plasma science and technology. J. Phys. D: Appl. Phys., 50(32):323001, 2017.
- [3] Igor V Adamovich, Ting Li, and Walter R Lempert. Kinetic mechanism of molecular energy transfer and chemical reactions in low-temperature air-fuel plasmas. *Philos. Trans. R. Soc. A*, 373(2048):20140336, 2015.
- [4] NL Aleksandrov and EM Anokhin. Low-energy electron attachment and detachment in vibrationally excited oxygen. J. Phys. D: Appl. Phys., 42(22):225210, 2009.
- [5] NL Aleksandrov and EM Anokhin. Electron detachment from o- 2 ions in oxygen: the effect of vibrational excitation and the effect of electric field. J. Phys. B, 44(11):115202, 2011.
- [6] NL Aleksandrov, SV Kindysheva, EN Kukaev, SM Starikovskaya, and A Yu Starikovskii. Simulation of the ignition of a methane-air mixture by a high-voltage nanosecond discharge. *Plasma Phys. Rep.*, 35(10):867–882, 2009.

- [7] Ann S Almgren, John B Bell, Phillip Colella, Louis H Howell, and Michael L Welcome. A conservative adaptive projection method for the variable density incompressible navier–stokes equations. J. Comput. Phys., 142(1):1–46, 1998.
- [8] Nikolay Anikin, Evgeny Kukaev, Svetlana Starikovskaia, and Andrei Starikovskii. Ignition of hydrogen-air and methane-air mixtures at low temperatures by nanosecond high voltage discharge. In 42nd AIAA Aerospace Sciences Meeting and Exhibit, page 833, 2004.
- [9] Robert R Arslanbekov and Vladimir I Kolobov. Two-dimensional simulations of the transition from townsend to glow discharge and subnormal oscillations. J. Phys. D: Appl. Phys., 36(23):2986, 2003.
- [10] Natalia Yu Babaeva and Mark J Kushner. Effect of inhomogeneities on streamer propagation: Ii. streamer dynamics in high pressure humid air with bubbles. *Plasma Sources Sci. Technol.*, 18(3):035010, 2009.
- [11] Behnaz Bagheri and Jannis Teunissen. The effect of the stochasticity of photoionization on 3d streamer simulations. *Plasma Sources Sci. Technol.*, 28(4):045013, 2019.
- [12] Behnaz Bagheri, Jannis Teunissen, and Ute Ebert. Simulation of positive streamers in co2 and in air: the role of photoionization or other electron sources. Plasma Sources Sci. Technol., 29(12):125021, 2020.
- [13] Séverine Barbosa, Guillaume Pilla, Deanna Lacoste, Philippe Scouflaire, Sébastien Ducruix, C Laux, and Denis Veynante. Influence of a repetitively pulsed

- plasma on the flame stability domain of a lab-scale gas turbine combustor. In Fourth European combustion meeting, pages 1–6, 2009.
- [14] N Barleon, L Cheng, B Cuenot, O Vermorel, and A Bourdon. Investigation of the impact of nrp discharge frequency on the ignition of a lean methane-air mixture using fully coupled plasma-combustion numerical simulations. *Proc.* Combust. Inst., 2022.
- [15] Yacine Bechane and Benoit Fiorina. Numerical investigations of turbulent premixed flame ignition by a series of nanosecond repetitively pulsed discharges. Proc. Combust. Inst., 38(4):6575–6582, 2021.
- [16] A Belasri, JP Boeuf, and LC Pitchford. Cathode sheath formation in a discharge-sustained xecl laser. J. Appl. Phys., 74(3):1553–1567, 1993.
- [17] Aurélie Bellemans, Nicholas Kincaid, Nicholas Deak, Perrine Pepiot, and Fabrizio Bisetti. P-drgep: a novel methodology for the reduction of kinetics mechanisms for plasma-assisted combustion applications. *Proc. Combust. Inst.*, 38(4):6631–6639, 2021.
- [18] Marsha Berger and Andrew Giuliani. A state redistribution algorithm for finite volume schemes on cut cell meshes. J. Comput. Phys., 428:109820, 2021.
- [19] Fabrizio Bisetti and Mbark El Morsli. Kinetic parameters, collision rates, energy exchanges and transport coefficients of non-thermal electrons in premixed

- flames at sub-breakdown electric field strengths. Combust. Theory Model., 18(1):148–184, 2014.
- [20] Anne Bourdon, Zdenek Bonaventura, and Sébastien Celestin. Influence of the pre-ionization background and simulation of the optical emission of a streamer discharge in preheated air at atmospheric pressure between two point electrodes. *Plasma Sources Sci. Technol.*, 19(3):034012, 2010.
- [21] Anne Bourdon, VP Pasko, NY Liu, Sébastien Célestin, Pierre Ségur, and Emmanuel Marode. Efficient models for photoionization produced by non-thermal gas discharges in air based on radiative transfer and the helmholtz equations. Plasma Sources Sci. Technol., 16(3):656, 2007.
- [22] Anne Bourdon, François Péchereau, Fabien Tholin, and Zdenek Bonaventura. Study of the electric field in a diffuse nanosecond positive ionization wave generated in a pin-to-plane geometry in atmospheric pressure air. *J. Phys. D: Appl. Phys.*, 54(7):075204, 2020.
- [23] Dennis Bouwman, Jannis Teunissen, and Ute Ebert. 3d particle simulations of positive air–methane streamers for combustion. *Plasma Sources Sci. Technol.*, 31(4):045023, 2022.
- [24] FH Branin. Transient analysis of lossless transmission lines. *Proceedings of the IEEE*, 55(11):2012–2013, 1967.
- [25] Doug Breden and Laxminarayan Raja. Simulations of nanosecond pulsed

- plasmas in supersonic flows for combustion applications. $AIAA\ J.,\ 50(3):647-658,\ 2012.$
- [26] Douglas Breden, Laxminarayan L Raja, Cherian A Idicheria, Paul M Najt, and Shankar Mahadevan. A numerical study of high-pressure non-equilibrium streamers for combustion ignition application. J. Appl. Phys., 114(8):083302, 2013.
- [27] PJ Bruggeman, Mark J Kushner, Bruce R Locke, Johannes GE Gardeniers, WG Graham, David B Graves, RCHM Hofman-Caris, Dragana Maric, Jonathan P Reid, Elisa Ceriani, et al. Plasma-liquid interactions: a review and roadmap. Plasma Sources Sci. Technol., 25(5):053002, 2016.
- [28] Mario Capitelli and J Norman Bardsley. *Nonequilibrium processes in partially ionized gases*, volume 220. Springer Science & Business Media, 2012.
- [29] Maria Castela, Benoît Fiorina, Axel Coussement, Olivier Gicquel, Nasser Darabiha, and Christophe O Laux. Modelling the impact of non-equilibrium discharges on reactive mixtures for simulations of plasma-assisted ignition in turbulent flows. Combust. Flame, 166:133–147, 2016.
- [30] Maria Castela, Sergey Stepanyan, Benoit Fiorina, Axel Coussement, Olivier Gicquel, Nasser Darabiha, and Christophe O Laux. A 3-d dns and experimental study of the effect of the recirculating flow pattern inside a reactive kernel produced by nanosecond plasma discharges in a methane-air mixture. Proc. Combust. Inst., 36(3):4095–4103, 2017.

- [31] Mirko Černák, D Bessieres, and J Paillol. Positive streamer formation in cathode region of pulsed high-pressure discharges for transversely excited atmosphere laser applications. J. Appl. Phys., 110(5):053303, 2011.
- [32] Mirko Černák, Tomáš Hoder, and Zdeněk Bonaventura. Streamer breakdown: cathode spot formation, trichel pulses and cathode-sheath instabilities. *Plasma Sources Sci. Technol.*, 29(1):013001, 2019.
- [33] Olivier Chanrion and Torsten Neubert. A pic-mcc code for simulation of streamer propagation in air. *J. Comput. Phys.*, 227(15):7222–7245, 2008.
- [34] PJ Chantry, AV Phelps, and GJ Schulz. Theory of electron collision experiments at intermediate and high gas densities. *Phys. Rev.*, 152(1):81, 1966.
- [35] Zheng Chen, Michael P Burke, and Yiguang Ju. On the critical flame radius and minimum ignition energy for spherical flame initiation. *Proc. Combust.* Inst., 33(1):1219–1226, 2011.
- [36] Valentino Cruccolini, Riccardo Scarcelli, Michele Battistoni, Carlo Nazareno Grimaldi, Massimo Augusto Dal Re, Douglas Breden, and Laxminarayan L Raja. Multidimensional modeling of non-equilibrium plasma generated by a radio-frequency corona discharge. *Plasma Sources Sci. Technol.*, 29(11):115013, 2020.
- [37] Nicholas Deak, Aurélie Bellemans, and Fabrizio Bisetti. Plasma-assisted ignition of methane/air and ethylene/air mixtures: Efficiency at low and high pressures. *Proc. Combust. Inst.*, 38(4):6551–6558, 2021.

- [38] Nicholas E Deak, Alfredo Duarte, and Fabrizio Bisetti. Steady-state streamer simulations using a spectral deferred correction strategy. In AIAA Scitech 2021 Forum, page 0685, 2021.
- [39] Anthony C DeFilippo and Jyh-Yuan Chen. Modeling plasma-assisted methane—air ignition using pre-calculated electron impact reaction rates. *Combust.*Flame, 172:38–48, 2016.
- [40] John V DiCarlo and Mark J Kushner. Solving the spatially dependent boltz-mann's equation for the electron-velocity distribution using flux corrected transport. J. Appl. Phys., 66(12):5763–5774, 1989.
- [41] Zakari Sebastian Eckert. Energy Transfer in Non-Equilibrium Reacting Gas Flows: Applications in Plasma Assisted Combustion and Chemical Gas Lasers. PhD thesis, The Ohio State University, 2018.
- [42] Alexandre Ern and Vincent Giovangigli. *Multicomponent transport algorithms*, volume 24. Springer Science & Business Media, 1994.
- [43] Lucas Esclapez, Valentina Ricchiuti, John B Bell, and Marcus S Day. A spectral deferred correction strategy for low mach number reacting flows subject to electric fields. Combust. Theory Model., 24(2):194–220, 2020.
- [44] John E Foster, Selman Mujovic, Joseph Groele, and Isaiah M Blankson. Towards high throughput plasma based water purifiers: design considerations and the pathway towards practical application. J. Phys. D: Appl. Phys., 51(29):293001, 2018.

- [45] RN Franklin. The plasma–sheath boundary region. J. Phys. D: Appl. Phys., 36(22):R309, 2003.
- [46] S. Goldman. Transformation calculus and electrical transients. *The Mathematical Gazette*, 34(309):239–239, 1950.
- [47] VV Gorin, AA Kudryavtsev, Jingfeng Yao, Chengxun Yuan, and Zhongxiang Zhou. Boundary conditions for drift-diffusion equations in gas-discharge plasmas. *Phys. Plasmas*, 27(1):013505, 2020.
- [48] GK Grubert, MM Becker, and D Loffhagen. Why the local-mean-energy approximation should be used in hydrodynamic plasma descriptions instead of the local-field approximation. *Phys. Rev. E*, 80(3):036405, 2009.
- [49] Vyaas Gururajan, Riccardo Scarcelli, Anand Karpatne, Douglas Breden, Laxminarayan Raja, Sayan Biswas, and Isaac Ekoto. A computational study of the thermodynamic conditions leading to autoignition in nanosecond pulsed discharges. J. Eng. Gas Turbine Power, 143(11), 2021.
- [50] GJM Hagelaar and LC Pitchford. Solving the boltzmann equation to obtain electron transport coefficients and rate coefficients for fluid models. *Plasma Sources Sci. Technol.*, 14(4):722, 2005.
- [51] Jie Han, Memdouh Belhi, Fabrizio Bisetti, and S Mani Sarathy. Numerical modelling of ion transport in flames. Combust. Theory Model., 19(6):744–772, 2015.

- [52] SC Haydon and OM Williams. Combined spatial and temporal studies of ionization growth in nitrogen. J. Phys. D: Appl. Phys., 9(3):523, 1976.
- [53] Alan C Hindmarsh, Peter N Brown, Keith E Grant, Steven L Lee, Radu Serban, Dan E Shumaker, and Carol S Woodward. Sundials: Suite of nonlinear and differential/algebraic equation solvers. ACM Trans. Math. Software, 31(3):363–396, 2005.
- [54] Erjiang Hu, Xiaotian Li, Xin Meng, Yizhen Chen, Yu Cheng, Yongliang Xie, and Zuohua Huang. Laminar flame speeds and ignition delay times of methane—air mixtures at elevated temperatures and pressures. *Fuel*, 158:1–10, 2015.
- [55] Bang-Dou Huang, Emile Carbone, Keisuke Takashima, Xi-Ming Zhu, Uwe Czarnetzki, and Yi-Kang Pu. The effect of the pulse repetition rate on the fast ionization wave discharge. J. Phys. D: Appl. Phys., 51(22):225202, 2018.
- [56] Bangdou Huang, Cheng Zhang, Jintao Qiu, Xuan Zhang, Yujian Ding, and Tao Shao. The dynamics of discharge propagation and x-ray generation in nanosecond pulsed fast ionisation wave in 5 mbar nitrogen. *Plasma Sources* Sci. Technol., 28(9):095001, 2019.
- [57] AA Ionin, IV Kochetov, AP Napartovich, and NN Yuryshev. Physics and engineering of singlet delta oxygen production in low-temperature plasma. J. Phys. D: Appl. Phys., 40(2):R25, 2007.
- [58] Hans Johansen and Phillip Colella. A cartesian grid embedded boundary method for poisson's equation on irregular domains. *J. Comput. Phys.*,

- 147(1):60-85, 1998.
- [59] Eric Johnsen, Johan Larsson, Ankit V Bhagatwala, William H Cabot, Parviz Moin, Britton J Olson, Pradeep S Rawat, Santhosh K Shankar, Björn Sjögreen, Helen C Yee, et al. Assessment of high-resolution methods for numerical simulations of compressible turbulence with shock waves. J. Comput. Phys., 229(4):1213–1237, 2010.
- [60] Yiguang Ju, Joseph K Lefkowitz, Christopher B Reuter, Sang Hee Won, Xueliang Yang, Suo Yang, Wenting Sun, Zonglin Jiang, and Qi Chen. Plasma assisted low temperature combustion. 36(1):85–105, 2016.
- [61] Yiguang Ju and Wenting Sun. Plasma assisted combustion: Dynamics and chemistry. *Prog. Energy Combust. Sci.*, 48:21–83, 2015.
- [62] DENG Jun, HE Liming, LIU Xingjian, and CHEN Yi. Numerical simulation of plasma-assisted combustion of methane-air mixtures in combustion chamber. Plasma Sources Sci. Technol., 20(12):125502, 2018.
- [63] Robert J Kee, Fran M Rupley, and James A Miller. Chemkin-ii: A fortran chemical kinetics package for the analysis of gas-phase chemical kinetics. Technical report, Sandia National Labs., Livermore, CA (USA), 1989.
- [64] Ahmed Khacef, Jean Marie Cormier, and Jean Michel Pouvesle. Nox remediation in oxygen-rich exhaust gas using atmospheric pressure non-thermal plasma generated by a pulsed nanosecond dielectric barrier discharge. J. Phys. D: Appl. Phys., 35(13):1491, 2002.

- [65] Joohan Kim, Vyaas Gururajan, Riccardo Scarcelli, Sayan Biswas, and Isaac Ekoto. Modeling nanosecond-pulsed spark discharge and flame kernel evolution. J. Energy Resour. Technol., 144(2), 2022.
- [66] Wookyung Kim, M Godfrey Mungal, and Mark A Cappelli. The role of in situ reforming in plasma enhanced ultra lean premixed methane/air flames. Combust. Flame, 157(2):374–383, 2010.
- [67] Hideaki Kobayashi, Yasuharu Kawabata, and Kaoru Maruta. Experimental study on general correlation of turbulent burning velocity at high pressure. In Proc. Combust. Inst., volume 27, pages 941–948. Elsevier, 1998.
- [68] Sumire Kobayashi, Zdeněk Bonaventura, Fabien Tholin, Nikolay A Popov, and Anne Bourdon. Study of nanosecond discharges in h2-air mixtures at atmospheric pressure for plasma assisted combustion applications. *Plasma Sources Sci. Technol.*, 26(7):075004, 2017.
- [69] A Alexander Konnov. Implementation of the ncn pathway of prompt-no formation in the detailed reaction mechanism. Combust. Flame, 156(11):2093–2105, 2009.
- [70] IA Kossyi, A Yu Kostinsky, AA Matveyev, and VP Silakov. Kinetic scheme of the non-equilibrium discharge in nitrogen-oxygen mixtures. *Plasma Sources* Sci. Technol., 1(3):207, 1992.
- [71] Juliusz Kruszelnicki, Amanda M Lietz, and Mark J Kushner. Atmospheric pressure plasma activation of water droplets. J. Phys. D: Appl. Phys.,

- 52(35):355207, 2019.
- [72] AA Kulikovsky. Positive streamer in a weak field in air: A moving avalancheto-streamer transition. *Phys. Rev. E*, 57(6):7066, 1998.
- [73] DA Lacoste, JP Moeck, D Durox, CO Laux, and Thierry Schuller. Effect of nanosecond repetitively pulsed discharges on the dynamics of a swirl-stabilized lean premixed flame. J. Eng. Gas Turbine Power, 135(10), 2013.
- [74] Suzanne Lanier, Ivan Shkurenkov, Igor V Adamovich, and Walter R Lempert. Two-stage energy thermalization mechanism in nanosecond pulse discharges in air and hydrogen-air mixtures. *Plasma Sources Science and Technology*, 24(2):025005, 2015.
- [75] Michael F L'Annunziata. *Handbook of radioactivity analysis*. Academic press, 2012.
- [76] Joseph K Lefkowitz, Peng Guo, Timothy Ombrello, Sang Hee Won, Christopher A Stevens, John L Hoke, Frederick Schauer, and Yiguang Ju. Schlieren imaging and pulsed detonation engine testing of ignition by a nanosecond repetitively pulsed discharge. Combust. Flame, 162(6):2496–2507, 2015.
- [77] Joseph K Lefkowitz, Peng Guo, Aric Rousso, and Yiguang Ju. Species and temperature measurements of methane oxidation in a nanosecond repetitively pulsed discharge. *Philos. Trans. R. Soc. A*, 373(2048):20140333, 2015.

- [78] Joseph K Lefkowitz and Timothy Ombrello. Reduction of flame development time in nanosecond pulsed high frequency discharge ignition of flowing mixtures. Combust. Flame, 193:471–480, 2018.
- [79] Joseph K Lefkowitz, Mruthunjaya Uddi, Bret C Windom, Guofeng Lou, and Yiguang Ju. In situ species diagnostics and kinetic study of plasma activated ethylene dissociation and oxidation in a low temperature flow reactor. *Proc.* Combust. Inst., 35(3):3505–3512, 2015.
- [80] Sergey B Leonov and Dmitry A Yarantsev. Plasma-induced ignition and plasma-assisted combustion in high-speed flow. *Plasma Sources Sci. Technol.*, 16(1):132, 2006.
- [81] Dmitry Levko, Ashish Sharma, and Laxminarayan L Raja. Plasmas generated in bubbles immersed in liquids: direct current streamers versus microwave plasma. J. Phys. D: Appl. Phys., 49(28):285205, 2016.
- [82] Youwen Liang, Stephen B Pope, and Perrine Pepiot. A pre-partitioned adaptive chemistry methodology for the efficient implementation of combustion chemistry in particle pdf methods. *Combust. Flame*, 162(9):3236–3253, 2015.
- [83] Jin-Yuan Liu, Zheng-Xiong Wang, and Xiaogang Wang. Sheath criterion for a collisional sheath. *Phys. Plasmas*, 10(7):3032–3034, 2003.
- [84] Ningyu Liu and Victor P Pasko. Effects of photoionization on propagation and branching of positive and negative streamers in sprites. J. Geophys. Res. Space Phys., 109(A4), 2004.

- [85] Xunchen Liu, Sibo Huang, Guoqing Wang, Hongyu Xiong, and Fei Qi. Applying an in-situ calibration method of spectral line shape to determine flame temperature of methane and ethylene spherically expanding flames. Combust. Flame, 237:111743, 2022.
- [86] Guofeng Lou, Ainan Bao, Munetake Nishihara, Saurabh Keshav, Yurii G Utkin, J William Rich, Walter R Lempert, and Igor V Adamovich. Ignition of premixed hydrocarbon–air flows by repetitively pulsed, nanosecond pulse duration plasma. *Proc. Combust. Inst.*, 31(2):3327–3334, 2007.
- [87] John J Lowke and Richard Morrow. Theoretical analysis of removal of oxides of sulphur and nitrogen in pulsed operation of electrostatic precipitators. *IEEE Trans. Plasma Sci.*, 23(4):661–671, 1995.
- [88] Tianfeng Lu and Chung K Law. A directed relation graph method for mechanism reduction. *Proc. Combust. Inst.*, 30(1):1333–1341, 2005.
- [89] X Lu, GV Naidis, M Laroussi, S Reuter, DB Graves, and K Ostrikov. Reactive species in non-equilibrium atmospheric-pressure plasmas: Generation, transport, and biological effects. *Phys. Rev.*, 630:1–84, 2016.
- [90] Alejandro Luque, Ute Ebert, Carolynne Montijn, and Willem Hundsdorfer. Photoionization in negative streamers: Fast computations and two propagation modes. Appl. Phys., 90(8):081501, 2007.
- [91] Sergey O Macheret, Mikhail N Shneider, and Richard B Miles. Modeling of air

- plasma generation by repetitive high-voltage nanosecond pulses. 30(3):1301–1314, 2002.
- [92] M Makarov. Effect of electrode processes on the spatial uniformity of the xecl laser discharge. J. Phys. D: Appl. Phys., 28(6):1083, 1995.
- [93] Xingqian Mao, Hongtao Zhong, Tianhan Zhang, Andrey Starikovskiy, and Yiguang Ju. Modeling of the effects of non-equilibrium excitation and electrode geometry on h2/air ignition in a nanosecond plasma discharge. *Combust. Flame*, 240:112046, 2022.
- [94] Robert Marskar. An adaptive cartesian embedded boundary approach for fluid simulations of two-and three-dimensional low temperature plasma filaments in complex geometries. J. Comput. Phys., 388:624–654, 2019.
- [95] Robert Marskar. 3d fluid modeling of positive streamer discharges in air with stochastic photoionization. *Plasma Sources Sci. Technol.*, 29(5):055007, 2020.
- [96] Luca L Massa and Jonathan B Freund. An integrated predictive simulation model for the plasma-assisted ignition of a fuel jet in a turbulent crossflow. In 54th AIAA Aerospace Sciences Meeting, page 2154, 2016.
- [97] Ralph Menikoff and Bradley J Plohr. The riemann problem for fluid flow of real materials. *Rev. Mod. Phys*, 61(1):75, 1989.
- [98] James B Michael, Tat Loon Chng, and Richard B Miles. Sustained propagation of ultra-lean methane/air flames with pulsed microwave energy deposition. Combust. Flame, 160(4):796–807, 2013.

- [99] Roger C Millikan and Donald R White. Systematics of vibrational relaxation.
 J. Chem. Phys., 39(12):3209–3213, 1963.
- [100] Jonas Moeck, Deanna Lacoste, Christophe Laux, and Christian Paschereit. Control of combustion dynamics in a swirl-stabilized combustor with nanosecond repetitively pulsed discharges. In 51st AIAA Aerospace Sciences Meeting including the New Horizons Forum and Aerospace Exposition, page 565, 2013.
- [101] R Morrow and N Sato. The discharge current induced by the motion of charged particles in time-dependent electric fields; sato's equation extended. *Journal* of Physics D: Applied Physics, 32(5):L20, 1999.
- [102] Sharath Nagaraja, Vigor Yang, and Igor Adamovich. Multi-scale modelling of pulsed nanosecond dielectric barrier plasma discharges in plane-to-plane geometry. J. Phys. D: Appl. Phys., 46(15):155205, 2013.
- [103] Sharath Nagaraja, Vigor Yang, Zhiyao Yin, and Igor Adamovich. Ignition of hydrogen-air mixtures using pulsed nanosecond dielectric barrier plasma discharges in plane-to-plane geometry. Combust. Flame, 161(4):1026-1037, 2014.
- [104] GV Naidis. Modelling of transient plasma discharges in atmospheric-pressure methane–air mixtures. J. Phys. D: Appl. Phys., 40(15):4525, 2007.
- [105] S Nijdam, G Wormeester, EM Van Veldhuizen, and U Ebert. Probing background ionization: positive streamers with varying pulse repetition rate and with a radioactive admixture. J. Phys. D: Appl. Phys., 44(45):455201, 2011.

- [106] Sander Nijdam, Jannis Teunissen, and Ute Ebert. The physics of streamer discharge phenomena. Plasma Sources Science and Technology, 29(10):103001, 2020.
- [107] Atsushi Nishiyama and Yuji Ikeda. Improvement of lean limit and fuel consumption using microwave plasma ignition technology. Technical report, SAE Technical Paper, 2012.
- [108] A Nonaka, JB Bell, MS Day, C Gilet, AS Almgren, and ML Minion. A deferred correction coupling strategy for low mach number flow with complex chemistry. *Combust. Theory Model.*, 16(6):1053–1088, 2012.
- [109] David Z Pai, Deanna A Lacoste, and Christophe O Laux. Nanosecond repetitively pulsed discharges in air at atmospheric pressure—the spark regime. Plasma Sources Sci. Technol., 19(6):065015, 2010.
- [110] David Z Pai, Deanna A Lacoste, and Christophe O Laux. Transitions between corona, glow, and spark regimes of nanosecond repetitively pulsed discharges in air at atmospheric pressure. J. Appl. Phys., 107(9):093303, 2010.
- [111] David Z Pai, Gabi D Stancu, Deanna A Lacoste, and Christophe O Laux. Nanosecond repetitively pulsed discharges in air at atmospheric pressure—the glow regime. *Plasma Sources Sci. Technol.*, 18(4):045030, 2009.
- [112] S Pancheshnyi, S Biagi, MC Bordage, GJM Hagelaar, WL Morgan, AV Phelps, and LC Pitchford. The lxcat project: Electron scattering cross sections and

- swarm parameters for low temperature plasma modeling. *Chem. Phys.*, 398:148–153, 2012.
- [113] Sergey Pancheshnyi. Role of electronegative gas admixtures in streamer start, propagation and branching phenomena. *Plasma Sources Sci. Technol.*, 14(4):645, 2005.
- [114] Sergey Pancheshnyi. Photoionization produced by low-current discharges in o2, air, n2 and co2. *Plasma Sources Sci. Technol.*, 24(1):015023, 2014.
- [115] Sergey Pancheshnyi, M Nudnova, and A Starikovskii. Development of a cathode-directed streamer discharge in air at different pressures: experiment and comparison with direct numerical simulation. *Phys. Rev. E*, 71(1):016407, 2005.
- [116] Sergey Pancheshnyi, Pierre Ségur, Julien Capeillère, and Anne Bourdon. Numerical simulation of filamentary discharges with parallel adaptive mesh refinement. J. Comput. Phys., 227(13):6574–6590, 2008.
- [117] SV Pancheshnyi, SM Starikovskaia, and A Yu Starikovskii. Role of photoionization processes in propagation of cathode-directed streamer. J. Phys. D: Appl. Phys., 34(1):105, 2001.
- [118] SV Pancheshnyi and A Yu Starikovskii. Two-dimensional numerical modelling of the cathode-directed streamer development in a long gap at high voltage. J. Phys. D: Appl. Phys., 36(21):2683, 2003.

- [119] L Papageorgiou, AC Metaxas, and George E Georghiou. Three-dimensional numerical modelling of gas discharges at atmospheric pressure incorporating photoionization phenomena. J. Phys. D: Appl. Phys., 44(4):045203, 2011.
- [120] Bernard Parent, Mikhail N Shneider, and Sergey O Macheret. Sheath governing equations in computational weakly-ionized plasmadynamics. J. Comput. Phys., 232(1):234–251, 2013.
- [121] Sang-Kyu Park and Demetre J Economou. Analysis of low pressure rf glow discharges using a continuum model. *J. Appl. Phys.*, 68(8):3904–3915, 1990.
- [122] SE Parker, RJ Procassini, CK Birdsall, and BI Cohen. A suitable boundary condition for bounded plasma simulation without sheath resolution. J. Comput. Phys., 104(1):41–49, 1993.
- [123] AV Phelps. The diffusion of charged particles in collisional plasmas: free and ambipolar diffusion at low and moderate pressures. J. Res. Natl. Inst., 95(4):407, 1990.
- [124] JM Plewa, O Eichwald, O Ducasse, P Dessante, Carolyn Jacobs, N Renon, and Mohammed Yousfi. 3d streamers simulation in a pin to plane configuration using massively parallel computing. J. Phys. D: Appl. Phys., 51(9):095206, 2018.
- [125] Jonathan Poggie, Igor Adamovich, Nicholas Bisek, and Munetake Nishihara. Numerical simulation of nanosecond-pulse electrical discharges. *Plasma Sources Sci. Technol.*, 22(1):015001, 2012.

- [126] AA Ponomarev and NL Aleksandrov. Monte carlo simulation of electron detachment properties for ions in oxygen and oxygen: nitrogen mixtures. *Plasma Sources Sci. Technol.*, 24(3):035001, 2015.
- [127] AA Ponomarev and NL Aleksandrov. Monte carlo simulation of negative ion kinetics in air plasmas in a time-varying electric field. J. Phys. D: Appl. Phys., 53(5):055203, 2019.
- [128] NA Popov. Fast gas heating in a nitrogen-oxygen discharge plasma: I. kinetic mechanism. *Journal of Physics D: Applied Physics*, 44(28):285201, 2011.
- [129] NA Popov. Erratum: Kinetics of plasma-assisted combustion: effect of non-equilibrium excitation on the ignition and oxidation of combustible mixtures. Plasma Sources Sci. Technol., 25(4):049601, 2016.
- [130] D Razus, C Movileanu, and D Oancea. Additive influence on ignition of stoichiometric ethylene-air mixture by break sparks. 232:134–140, 2018.
- [131] RAAV Roussel-Dupré and AV Gurevich. On runaway breakdown and upward propagating discharges. J. Geophys. Res. Space Phys., 101(A2):2297–2311, 1996.
- [132] Aric Rousso, Xingqian Mao, Qi Chen, and Yiguang Ju. Kinetic studies and mechanism development of plasma assisted pentane combustion. Proc. Combust. Inst., 37(4):5595–5603, 2019.

- [133] Aric Rousso, Suo Yang, Joseph Lefkowitz, Wenting Sun, and Yiguang Ju. Low temperature oxidation and pyrolysis of n-heptane in nanosecond-pulsed plasma discharges. *Proc. Combust. Inst.*, 36(3):4105–4112, 2017.
- [134] Jeffrey Santner, Frederick L Dryer, and Yiguang Ju. The effects of water dilution on hydrogen, syngas, and ethylene flames at elevated pressure. *Proceedings of the Combustion Institute*, 34(1):719–726, 2013.
- [135] N Sato. Discharge current induced by the motion of charged particles. *J. Phys. D: Appl. Phys.*, 13(1):L3, 1980.
- [136] Riccardo Scarcelli, Thomas Wallner, Sibendu Som, Sayan Biswas, Isaac Ekoto, Douglas Breden, Anand Karpatne, and Laxminarayan L Raja. Modeling nonequilibrium discharge and validating transient plasma characteristics at aboveatmospheric pressure. *Plasma Sources Sci. Technol.*, 27(12):124006, 2018.
- [137] Pierre Ségur, Anne Bourdon, E Marode, Delphine Bessières, and JH Paillol. The use of an improved eddington approximation to facilitate the calculation of photoionization in streamer discharges. *Plasma Sources Sci. Technol.*, 15(4):648, 2006.
- [138] Serhiy Serbin, Anna Mostipanenko, Igor Matveev, and Albina Topina. Improvement of the gas turbine plasma assisted combustor characteristics. In 49th AIAA aerospace sciences meeting including the new horizons forum and aerospace exposition, page 61, 2011.

- [139] James Sevik, Thomas Wallner, Michael Pamminger, Riccardo Scarcelli, Dan Singleton, and Jason Sanders. Extending lean and exhaust gas recirculation-dilute operating limits of a modern gasoline direct-injection engine using a low-energy transient plasma ignition system. J. Eng. Gas Turbine Power, 138(11), 2016.
- [140] Ashish Sharma, Vivek Subramaniam, Evrim Solmaz, and Laxminarayan L Raja. Fully coupled modeling of nanosecond pulsed plasma assisted combustion ignition. J. Phys. D: Appl. Phys., 52(9):095204, 2018.
- [141] SA Shcherbanev, Ch Ding, SM Starikovskaia, and NA Popov. Filamentary nanosecond surface dielectric barrier discharge. plasma properties in the filaments. *Plasma Sources Sci. Technol.*, 28(6):065013, 2019.
- [142] Feng Shi, Ningyu Liu, and Joseph R Dwyer. Three-dimensional modeling of two interacting streamers. Journal of Geophysical Research: Atmospheres, 122(19):10–169, 2017.
- [143] Taisuke Shiraishi, Tomonori Urushihara, and Martin Gundersen. A trial of ignition innovation of gasoline engine by nanosecond pulsed low temperature plasma ignition. J. Phys. D: Appl. Phys., 42(13):135208, 2009.
- [144] Ivan Shkurenkov and Igor V Adamovich. Energy balance in nanosecond pulse discharges in nitrogen and air. *Plasma Sources Sci. Technol.*, 25(1):015021, 2016.

- [145] G Simon and W Bötticher. Two-dimensional model of the ignition phase of high-pressure glow discharges. J. Appl. Phys., 76(9):5036–5046, 1994.
- [146] Dan Singleton, SJ Pendleton, and Martin A Gundersen. The role of nonthermal transient plasma for enhanced flame ignition in c2h4–air. J. Phys. D: Appl. Phys., 44(2):022001, 2010.
- [147] Hariswaran Sitaraman and Ray Grout. Premixed combustion simulations with a self-consistent plasma model for initiation. In 54th AIAA Aerospace Sciences Meeting, page 2158, 2016.
- [148] Hariswaran Sitaraman, Shashank Yellapantula, Marc T Henry de Frahan, Bruce Perry, Jon Rood, Ray Grout, and Marc Day. Adaptive mesh based combustion simulations of direct fuel injection effects in a supersonic cavity flame-holder. Combust. Flame, 232:111531, 2021.
- [149] Magnus Sjöberg, Wei Zeng, Daniel Singleton, Jason M Sanders, and Martin A Gundersen. Combined effects of multi-pulse transient plasma ignition and intake heating on lean limits of well-mixed e85 disi engine operation. SAE Int. J. Engines, 7(4):1781–1801, 2014.
- [150] Alessandro Stagni, Alessio Frassoldati, Alberto Cuoci, Tiziano Faravelli, and E Ranzi. Skeletal mechanism reduction through species-targeted sensitivity analysis. *Combust. Flame*, 163:382–393, 2016.
- [151] SM Starikovskaia. Plasma-assisted ignition and combustion: nanosecond discharges and development of kinetic mechanisms. *J. Phys. D: Appl. Phys.*,

- 47(35):353001, 2014.
- [152] Svetlana M Starikovskaia. Plasma assisted ignition and combustion. J. Phys. D: Appl. Phys., 39(16):R265, 2006.
- [153] A Yu Starikovskii, AA Nikipelov, MM Nudnova, and DV Roupassov. Sdbd plasma actuator with nanosecond pulse-periodic discharge. *Plasma Sources* Sci. Technol., 18(3):034015, 2009.
- [154] Andrey Starikovskiy and Nickolay Aleksandrov. Plasma-assisted ignition and combustion. *Prog. Energy Combust. Sci.*, 39(1):61–110, 2013.
- [155] Wenting Sun, Zheng Chen, Xiaolong Gou, and Yiguang Ju. A path flux analysis method for the reduction of detailed chemical kinetic mechanisms. Combust. Flame, 157(7):1298–1307, 2010.
- [156] H Takana, Y Tanaka, and H Nishiyama. Computational simulation of reactive species production by methane-air dbd at high pressure and high temperature. EPL (Europhysics Letters), 97(2):25001, 2012.
- [157] Jannis Teunissen and Ute Ebert. Simulating streamer discharges in 3d with the parallel adaptive afivo framework. J. Phys. D: Appl. Phys., 50(47):474001, 2017.
- [158] Jannis Teunissen and Ute Ebert. Afivo: A framework for quadtree/octree amr with shared-memory parallelization and geometric multigrid methods. Comput. Phys. Commun., 233:156–166, 2018.

- [159] Fabien Tholin and Anne Bourdon. Influence of temperature on the glow regime of a discharge in air at atmospheric pressure between two point electrodes. J. Phys. D: Appl. Phys., 44(38):385203, 2011.
- [160] Fabien Tholin and Anne Bourdon. Simulation of the hydrodynamic expansion following a nanosecond pulsed spark discharge in air at atmospheric pressure. J. Phys. D: Appl. Phys., 46(36):365205, 2013.
- [161] Fabien Tholin and Anne Bourdon. Simulation of the stable 'quasi-periodic'glow regime of a nanosecond repetitively pulsed discharge in air at atmospheric pressure. *Plasma Sources Sci. Technol.*, 22(4):045014, 2013.
- [162] Fabien Tholin, Deanna A Lacoste, and Anne Bourdon. Influence of fast-heating processes and o atom production by a nanosecond spark discharge on the ignition of a lean h2–air premixed flame. *Combust. Flame*, 161(5):1235–1246, 2014.
- [163] Kuninori Togai, Nicholas Tsolas, and Richard A Yetter. Kinetic modeling and sensitivity analysis of plasma-assisted oxidation in a h2/o2/ar mixture. Combust. Flame, 164:239–249, 2016.
- [164] Albina A Tropina, Mruthunjaya Uddi, and Yiguang Ju. On the effect of nonequilibrium plasma on the minimum ignition energy—part 1: Discharge model. *IEEE Trans. Plasma Sci.*, 39(1):615–623, 2010.
- [165] L-K Tseng, MA Ismail, and Gerard M Faeth. Laminar burning velocities and

- markstein numbers of hydrocarbonair flames. *Combust. Flame*, 95(4):410–426, 1993.
- [166] Nicholas Tsolas, Richard A Yetter, and Igor V Adamovich. Kinetics of plasma assisted pyrolysis and oxidation of ethylene. part 2: Kinetic modeling studies. Combust. Flame, 176:462–478, 2017.
- [167] Mruthunjaya Uddi, Huijun Guo, Wenting Sun, and Yiguang Ju. Studies of c2h6 air and c3h8/ air plasma assisted combustion kinetics in a nanosecond discharge. In 49th AIAA Aerospace Sciences Meeting Including the New Horizons Forum and Aerospace Exposition, 12 2011.
- [168] Jan Van Dijk, Kim Peerenboom, Manuel Jimenez, Diana Mihailova, and Joost Van der Mullen. The plasma modelling toolkit plasimo. J. Phys. D: Appl. Phys., 42(19):194012, 2009.
- [169] Peter LG Ventzek, Timothy J Sommerer, Robert J Hoekstra, and Mark J Kushner. Two-dimensional hybrid model of inductively coupled plasma sources for etching. Appl. Phys., 63(5):605–607, 1993.
- [170] PA Vitello, BM Penetrante, and JN Bardsley. Simulation of negative-streamer dynamics in nitrogen. *Phys. Rev. E*, 49(6):5574, 1994.
- [171] Angelika Wähner, Gisbert Gramse, Tim Langer, and Michael Beyer. Determination of the minimum ignition energy on the basis of a statistical approach. J. Loss Prev. Process Ind., 26(6):1655–1660, 2013.

- [172] Qiang Wang, Demetre J Economou, and Vincent M Donnelly. Simulation of a direct current microplasma discharge in helium at atmospheric pressure. J. Appl. Phys., 100(2):023301, 2006.
- [173] AL Ward. Calculations of cathode-fall characteristics. *J. Appl. Phys.*, 33(9):2789–2794, 1962.
- [174] C Winters, Z Eckert, Z Yin, K Frederickson, and IV Adamovich. Measurements and kinetic modeling of atomic species in fuel-oxidizer mixtures excited by a repetitive nanosecond pulse discharge. J. Phys. D: Appl. Phys., 51(1):015202, 2017.
- [175] Caroline Winters, Yi-Chen Hung, Elijah Jans, Zak Eckert, Kraig Frederickson, Igor V Adamovich, and Nikolay Popov. Oh radical kinetics in hydrogen-air mixtures at the conditions of strong vibrational nonequilibrium. J. Phys. D: Appl. Phys., 50(50):505203, 2017.
- [176] Gideon Wormeester, Sergey Pancheshnyi, Alejandro Luque, Sander Nijdam, and Ute Ebert. Probing photo-ionization: simulations of positive streamers in varying n2: O2-mixtures. J. Phys. D: Appl. Phys., 43(50):505201, 2010.
- [177] DA Xu, MN Shneider, DA Lacoste, and CO Laux. Thermal and hydrodynamic effects of nanosecond discharges in atmospheric pressure air. J. Phys. D: Appl. Phys., 47(23):235202, 2014.
- [178] Suo Yang, Xiang Gao, Vigor Yang, Wenting Sun, Sharath Nagaraja, Joseph K Lefkowitz, and Yiguang Ju. Nanosecond pulsed plasma activated c2h4/o2/ar

- mixtures in a flow reactor. J. Propul. Power, pages 1240–1252, 2016.
- [179] Suo Yang, Sharath Nagaraja, Wenting Sun, and Vigor Yang. A detailed comparison of thermal and nanosecond plasma assisted ignition of hydrogenair mixtures. In 53rd AIAA Aerospace Sciences Meeting, page 1615, 2015.
- [180] Z Yin, Z Eckert, IV Adamovich, and WR Lempert. Time-resolved radical species and temperature distributions in an ar–o2–h2 mixture excited by a nanosecond pulse discharge. *Proc. Combust. Inst.*, 35(3):3455–3462, 2015.
- [181] Mustapha Zakari, H Caquineau, P Hotmar, and P Ségur. An axisymmetric unstructured finite volume method applied to the numerical modeling of an atmospheric pressure gas discharge. J. Comput. Phys., 281:473–492, 2015.
- [182] Anqi Zhang, Riccardo Scarcelli, Thomas Wallner, Douglas Breden, Anand Karpatne, Laxminarayan L Raja, Isaac Ekoto, and Benjamin Wolk. Numerical investigation of nanosecond pulsed discharge in air at above-atmospheric pressures. J. Phys. D: Appl. Phys., 51(34):345201, 2018.
- [183] Li Zhang, Stijn Heijkers, Weizong Wang, Luca Matteo Martini, Paolo Tosi, Dezheng Yang, Zhi Fang, and Annemie Bogaerts. Dry reforming of methane in a nanosecond repetitively pulsed discharge: chemical kinetics modeling. Plasma Sources Sci. Technol., 31(5):055014, 2022.
- [184] Weiqun Zhang, Ann Almgren, Vince Beckner, John Bell, Johannes Blaschke, Cy Chan, Marcus Day, Brian Friesen, Kevin Gott, Daniel Graves, et al. Am-

- rex: a framework for block-structured adaptive mesh refinement. *J. Open Source Softw.*, 4(37):1370–1370, 2019.
- [185] MB Zhelezniak, A Kh Mnatsakanian, and Sergei Vasil'evich Sizykh. Photoionization of nitrogen and oxygen mixtures by radiation from a gas discharge. *High Temp.*, 20(3):357–362, 1982.
- [186] Wen Zhou, Heng Guo, Wei Jiang, He-Ping Li, Zeng-Yao Li, and Giovanni Lapenta. Particle-in-cell and monte carlo collision simulations of the cathode sheath in an atmospheric direct-current arc discharge. *Plasma Sources Sci. Technol.*, 25(5):05LT01, 2016.
- [187] Yujie Zhu, Xuewei Zhang, and Jinliang He. Predicting streamer discharge front splitting by ionization seed profiling. *Phys. Plasmas*, 26(2):023513, 2019.